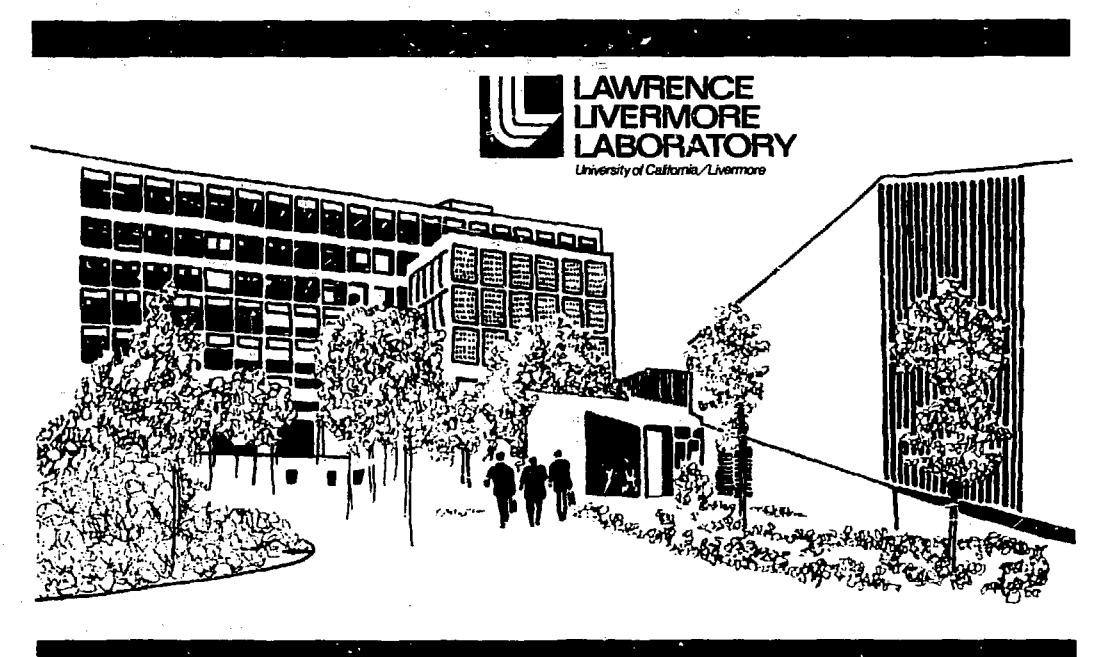# TANDEM MIRROR REACTOR WITH THERMAL BARRIERS

G. A. Carlson, B. Arfin, W. L. Barr, B. M. Boghosian,
J. L. Erickson, J. H. Fink, G. W. Hamilton, B. G.
Logan, J. O. Myall, and W. S. Neef, Jr.

MASTER

September 19, 1979

LAWRENCE
LIVERMORE
LABORATORY
University of California/Livermore

LAWRENCE LIVERMORE LABORATORY

University of California Livermore, California 94550

MASTER

UCRL-52836

TANDEM MIRROR REACTOR WITH THERMAL BARRIERS

G. A. Carlson, B. Arfin, W. L. Barr, B. M. Boghosian,
J. L. Erickson,* J. H. Fink,† G. W. Hamilton, B. G.
Logan, J. O. Myall, and W. S. Neef, Jr.

*Grumman Aerospace Corporation.
†Westinghouse Electric Corporation.

CONTENTS

ABSTRACT

The basic tandem mirror concept entails the improved axial confinement of a long cylindrical fusion plasma within a solenoid by means of strong electrostatic potentials at the ends. In the original tandem mirror concept, the confining electrostatic potential was produced by mirror-confined, end-plug plasmas of considerably higher density than the fusion plasma in the solenoidal center cell. As shown in a conceptual reactor design study completed in 1977, the requirement for a high plasma density plug led to advanced technological requirements for plug magnets and neutral-beam injectors.

A major new invention—the thermal barrier—can result in further improved axial confinement and, at the same time, a reduction in the end-plug technological requirements. Basically, the thermal barrier consists of a region of much reduced magnetic field strength, plasma density, and plasma potential between the solenoidal central cell and the end plug. The depressed positive plasma potential is an electrostatic barrier to electrons and permits the establishment of a hotter electron population in the plugs than in the central cell. The hotter electron population in turn increases the electrostatic confining potential. This report describes the concept of the improved tandem mirror reactor with thermal barriers and the progress we have made toward the conceptual design of such a reactor.

An analytic computer model for the tandem mirror plasma with thermal barriers has been constructed. Included is a detailed treatment of thermal ion trapping in the barrier region and barrier "pumping" by neutral beam charge exchange. Other new computer models were constructed to assess the MHD stability of plasmas contained in the new magnetic configuration.

1

Major end region elements of the new design are a magnet system comprised of a 12-T solenoidal barrier coil of niobium tin and niobium titanium plug coils (yin-yang shape) and transition coils, a low current 400 keV negative ion type neutral-beam injection system for the plugs, microwave heating of the plug electrons, a positive ion type neutral-beam system for charge-exchange "pumping" of the barrier region, and a plasma direct converter. The central cell is constructed of axial modules, each 2 m in length. Each module contains an annulus of helium-cooled blanket assemblies, a shield region, and two niobium titanium solenoidal coils.

Based on preliminary calculations, we set as the goal for the new reactor design a 500-MWe output from a high Q ($\geq$10) fusion plasma confined in a central cell about 60 m in length. Although our progress toward this goal has been significant, additional work must be done to achieve a self-consistent reactor design which satisifes all of the known physics constraints. The present magnet design has proved inadequate against the criterion for MHD ballooning stability at our assumed value for central cell β. Ongoing work emphasizes the redesign of the magnet system to increase the β limit for stability.

CHAPTER 1. OVERVIEW

G. A. Carlson

The concept of the tandem mirror magnetic fusion device was invented in 1976 by Logan and Fowler[1-1] at LLL and independently by Dimov[1-2] in the USSR. The basic concept entails the improved axial confinement of a long cylindrical fusion plasma within a solenoid by means of strong electrostatic potentials at the ends, produced by mirror-confined, end-plug plasmas. The first conceptual fusion reactor design based on the concept was published in July 1977[1-3]. The reactor had a central cell 100 m in length and produced 1000 MW of net electrical power from 2800 MW of fusion power. Drawbacks of the first design included a somewhat modest plasma performance (Q ≡ fusion power/total injected power trapped by the plasma ≈ 5) and a requirement for high technology components for the end plugs (17-T magnetic coils and 1.2-MeV neutral-beam injectors).

Work aimed at improving the tandem mirror reactor (TMR) was reported in April 1979.[1-4] In that report we investigated the use of auxiliary plasma cells (A-cells) at the ends of the reactor to improve plug confinement and to reduce the required neutral-beam injection energy, and the use of direct electron heating to further reduce the neutral-beam requirements. These new features also allowed the reduction of the plug magnetic field strengths. One reactor case reported in that study had a central cell 320 m in length and produced 3000 MW of fusion power. The maximum magnetic field strength (in the conductor of the axisymmetric plug coil set) was 15 T and the required neutral-beam injection energy was 350 keV. The reduced fusion power per metre of central cell length (compared to the 1977 design) was believed to be acceptable because of central cell design simplifications and cost reduction.

Also reported in April 1979 was a major new invention for tandem mirrors—the thermal barrier concept.[1-5] This invention followed from the

realization that the optimal use of electron heating in the tandem mirror involved the establishment of a hotter electron population in the plugs than in the central cell because the confining electrostatic potential is directly proportional to the electron temperature in the plugs, while cooler central cell electrons allow a higher fusion power density for a given magnetic field strength. However, in the normal tandem mirror, electron flow between the plugs and central cell is so high that only small temperature differences can be established, even with electron heating localized in the end plugs. The new concept introduces a barrier between the plug and central cell that effectively reduces the passing of central cell electrons into the plug. Because of the reduced electron interaction, a modest amount of electron heating in the plugs is sufficient to establish a large temperature difference.

Basically, the thermal barrier consists of a region of much reduced magnetic field strength, plasma density, and plasma potential. The depressed positive plasma potential is an electrostatic barrier to electrons. Although a region of reduced magnetic field strength could be produced in a tandem mirror by simply separating the plug coils from the central cell solenoid, it is more desirable to first increase the magnetic field at the end of the central cell, and then to produce the low field region by proper spacing of the plug coils. We call the new solenoidal coil at the end of the central cell the barrier coil. The primary physics complication introduced by the thermal barrier concept is the requirement for a method to prevent the filling of the barrier region by thermal ions leaking from the central cell. Such filling is unacceptable because it would negate the depression in plasma potential. In the April 1979 report,[1-4] two possible methods for "barrier pumping" were described: heating at the ion bounce frequency and a periodic elimination of the barrier magnetic well by means of an additional pulsed barrier coil. Since then, a third concept has emerged as the preferred method for barrier

pumping: the use of neutral beams to charge exchange with the thermal ions trapped in the barrier region. The charge exchange neutrals are lost radially from the plasma. By proper selection of the barrier pump neutral-beam energies and injection angles, the new ions are not trapped in the barrier region, but become fuel ions for the central cell.

In this report we describe the concept of this new TMR with thermal barriers and the progress we have made toward the conceptual design of such a reactor.

REACTOR DESCRIPTION AND SOME PRELIMINARY PARAMETERS

Figure 1-1 shows the proposed design for a 500-MWe tandem mirror reactor with thermal barriers. The DT fusion plasma is contained in the 56-m-long central cell. The central cell consists of 28 2-m-long modules, each containing an annular blanket region, a magnet shield region, and two niobium-titanium solenoidal magnets. The entire central cell resides in a vacuum trench, which allows the module-to-module seal to be made by an annular metal inflatable cushion. When the cushion is deflated, these seals allow the removal of individual modules by an overhead crane. Blanket coolant galleries are shown below the vacuum trench.

The end-plug components of the reactor are housed in large cylindrical vacuum vessels. Beginning at the central cell end, we see the high field barrier coil (a solenoid), a transition coil to transform the magnetic flux bundle from circular to elliptical, the minimum-B plug coils (a yin-yang pair), and a circularizing coil. The latter coil is used to recircularize the elliptical flux bundle emerging from the yin-yang and permits the use of a circular cross-section direct converter. The end-plug magnets are housed in a
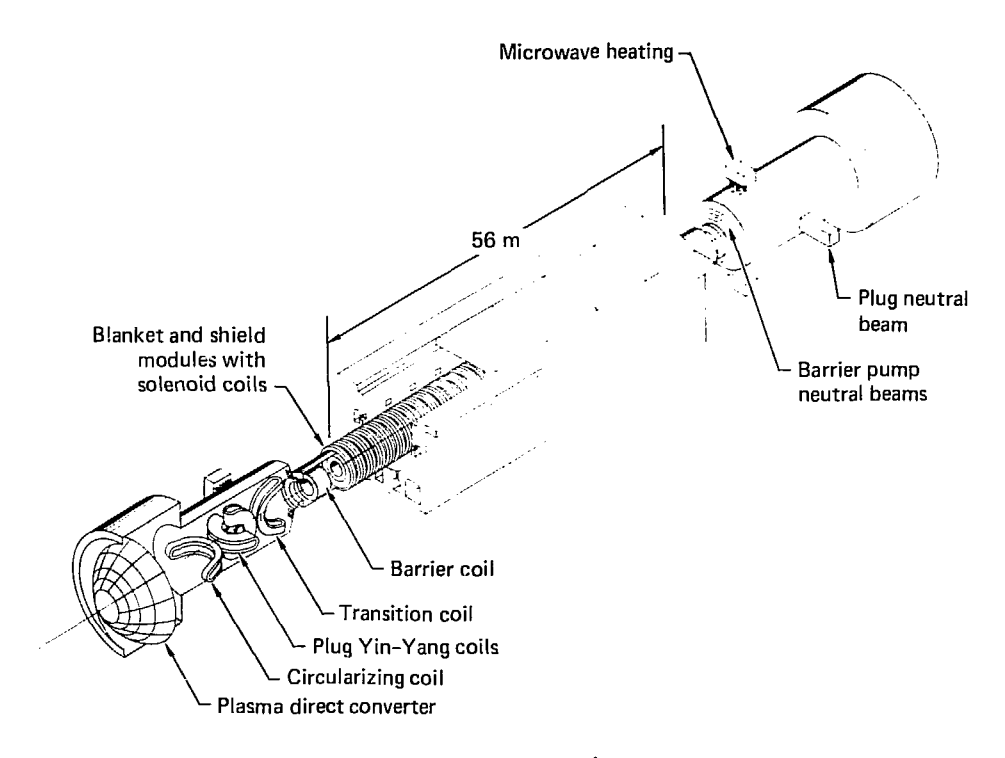
Fig. 1-1.   500-MWe tandem mirror reactor.

12-m-diam vacuum vessel; the plasma direct converter vacuum vessel is 20 m in diameter.

The plug plasmas, contained in the plug yin-yang coils, are each sustained by a low-current, 400-keV neutral beam (shown only on the far end in Fig. 1-1). Also shown is the gyrotron tube system for microwave heating of the electrons on the plug side of the thermal barrier. The small neutral beams indicated on the end wall of the plug vacuum vessel are the barrier region beams for charge-exchange pumping of the barrier and fueling of the central cell.

The preliminary design shown in Fig. 1-1 was based on a particular magnetic geometry. The various magnetic field strengths along the axis of the

machine are 2.8 T in the central cell, 12 T at the barrier maximum, 1.2 T at the barrier minimum, 6 T at the plug mirrors, and 4 T at the plug center.

For a central cell plasma β of 0.75, the fusion power is 31-MW power per metre of central cell length, or 1770 MW for the 56-m-long central cell. A preliminary analysis of the injection requirements for this reactor led to the simplified power flow diagram shown in Fig. 1-2. The total injection requirements for both plug regions are 1 MW of plug neutral beams, 54 MW of barrier-pump neutral beams, and 108 MW of electron cyclotron resonant heating (ECRH). Dividing the fusion power by the sum of these injection requirements yields a plasma $Q = 10.9$. Leaving the central cell are 1420 MW of neutron power and 516 MW of charged particle power. (Here we show the charged particle power as the total injected power plus 20% of the fusion power, which is an over-estimate due to the significant amount of charge-exchange neutral power that will deposit on the wall in the barrier region due to barrier pumping. We roughly compensate for this overestimate by choosing a modest direct conversion efficiency.) We have taken the blanket energy multiplication to be 1.2 and have chosen nominal efficiencies of 0.35 for the thermal converter and 0.5 for all of the neutral beams, the ECRH, and the plasma direct converter. As shown in Fig. 1-2, the resulting net electrical power is 527 MWe. Note that the plasma direct converter can provide most of the input power for the neutral beams and FCRH. This is advantageous in that the near instantaneous rise to power possible in the plasma direct converter (as opposed to the rise time of the thermal plant) will allow start-up of the reactor without a large power drain from the utility grid.

Because the central cell plasma is near or at ignition, the power output of the reactor can be increased by increasing the central cell length and re-taining the same end plug systems. Figure 1-3 shows the resulting power flow diagram for a reactor with a central cell length of 100 m. The fusion power
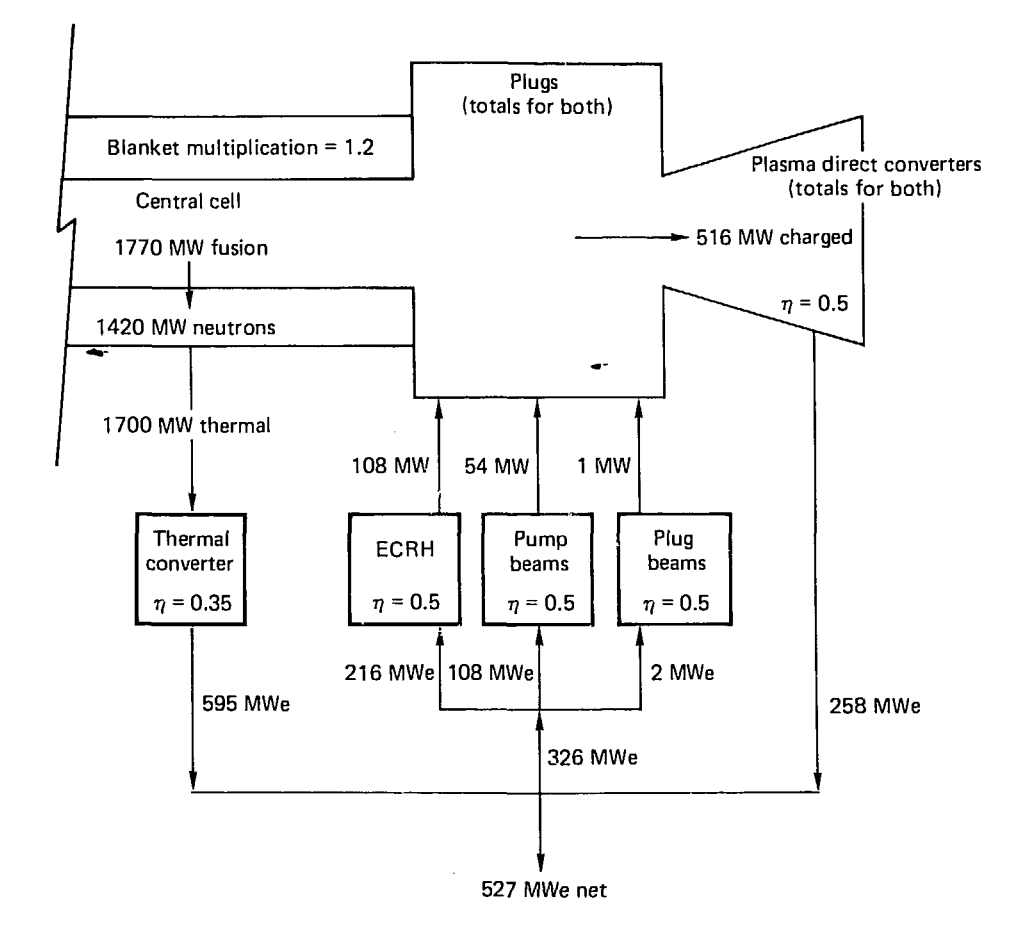
Fig. 1-2. Power flow diagram for a tandem mirror reactor with 56-m-long central cell (Q = 11).

is now 3160 MW, and because the end-plug injection requirements have not changed the plasma Q has increased to 19. The net power output of this larger reactor is 1130 MWe. Note that in this case the plasma direct converter output is more than adequate to power the neutral beams and ECRH.

It must be emphasized that the reactor parameters presented above are based on preliminary analysis and estimates and comprise the goal of our reactor design effort and not, at this time, a final, self-consistent point
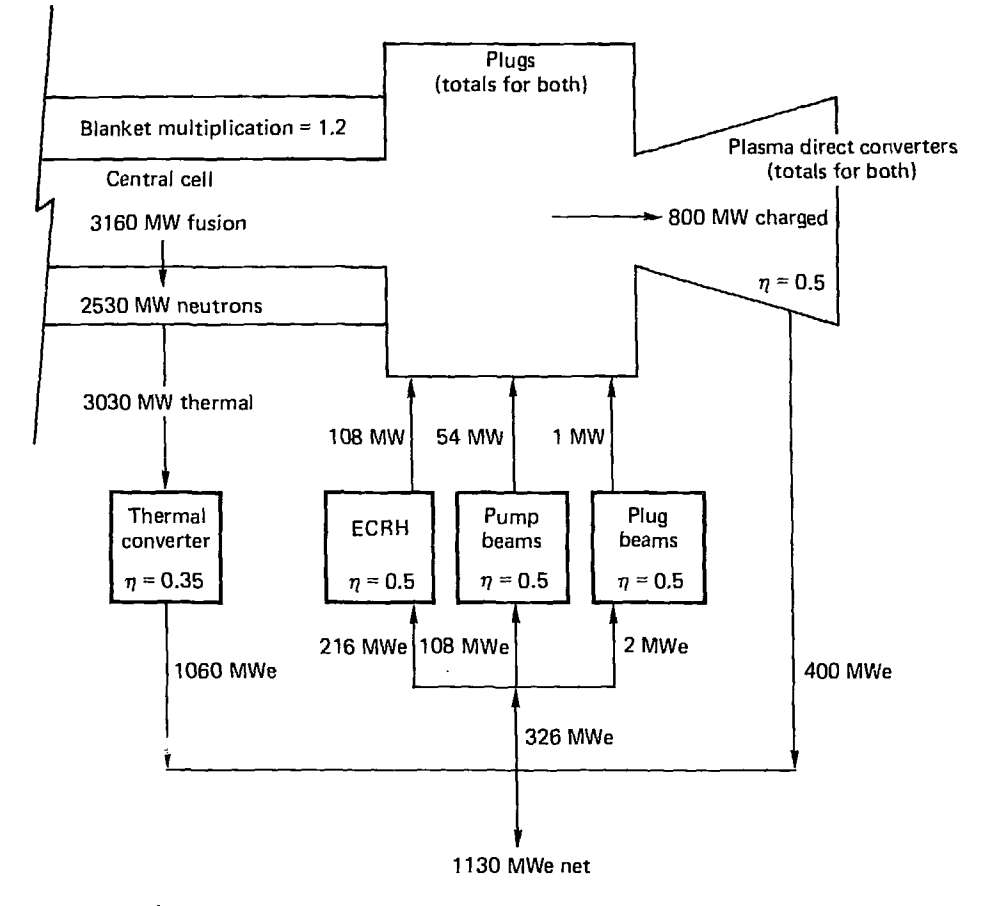
Fig. 1-3. Power flow diagram for tandem mirror reactor with
100-m-long central cell (Q = 19).

design. The following section of this overview and the body of the report de-
scribe our progress to date toward that goal.

REACTOR SUBSYSTEM DESIGN—PRESENT STATUS

In the several months since the invention of the thermal barrier con-
cept, we have made considerable progress toward the design of an improved
TMR. Several major new analytic tools have been developed: for example, a

plasma physics model incorporating a quite detailed treatment of charge-exchange pumped thermal barriers and two computer codes to assess complex tandem mirror magnet designs against plasma magnetohydrodynamic (MHD) stability criteria.

As discussed in the previous section, preliminary estimates of the performance of tandem mirrors with charge-exchange pumped thermal barriers have given us the goal of our design effort. At this time we have not yet achieved that goal. The most obvious shortfall is in the magnet design which failed the criterion for MHD ballooning stability at our assumed value for central cell β of 0.75. (This β value was demonstrated to more than meet the requirements for MHD interchange stability; unfortunately, the analytic tool to assess the ballooning criterion was not available until after the magnet design was complete.) Also, the large volume of the barrier region contributed to an undesirably large requirement for charge-exchange pumping.

Another contributing factor to the incompleteness of our design is the fact that the new physics model was just very recently completed so as to realistically treat the barrier region, and time has not permitted a thorough exercising of parameter space. Our ongoing work will emphasize the thorough exercising of the physics model and a major redesign of the magnet system. The goal of the magnet redesign will be a substantial shortening of the barrier region that will reduce the charge-exchange pumping requirements and also, we believe, improve the MHD stability situation.

In the remaining sections of the overview, we discuss briefly our progress to date on the individual subsystems of the reactor. Each of these aspects is covered in more detail in the main body of the report.

The major physics innovation in the present reactor design study is the thermal barrier concept. The thermal barrier consists of a region of much reduced magnetic field strength, plasma density, and plasma potential. The depressed positive plasma potential is an electrostatic barrier to electrons. Because of the reduced interaction of plug and central cell electrons, a modest amount of electron heating in the plugs is sufficient to establish an elevated electron temperature there. With thermal barriers the confining potential for central cell ions is given by:

$$\phi_c = T_{ep} \ln\left(\frac{n_p}{n_c}\right) + \left(T_{ep} - T_{ec}\right)\ln\left(\frac{n_c}{n_b}\right) \quad , \tag{1-1}$$

where T_{ep} is the plug electron temperature, T_{ec} is the central cell electron temperature, n_p/n_c is the plug-to-central cell density ratio, and n_c/n_b is the central cell-to-barrier density ratio. It follows that thermal barriers, giving $n_c/n_b > 1$, and ECRH, giving $T_{ep} > T_{ec}$, allow better central cell confinement with lower n_p/n_c (even $n_p/n_c < 1$) and thus a lower magnetic field ratio, B_p/B_c.

An analytic model for the tandem mirror plasma with thermal barriers has been constructed and is presented in Chapter 2. Especially noteworthy is the detailed treatment of thermal ion trapping in the barrier region and barrier pumping by neutral-beam charge exchange. Because this part of the physics analysis utilizes magnetic field data, it must be closely coordinated with the magnet design.

Two computer models were constructed to assess the interchange and ballooning modes of MHD stability for plasmas contained in the new tandem mirror

magnetic configuration. Results from the first model indicate that our present magnet design is satisfactory for the interchange mode. But recent calculations with the second model indicate that the ballooning mode would allow a central cell β of only ~0.1 for our present magnet design. Operation at this low a β would result in an unacceptably low plasma Q. A preliminary analysis indicates that a considerably shorter barrier region will be needed to meet our high Q reactor goal.

Magnets

The arrangement of magnets is shown in Fig. 1-1, and the field strength variation along the reactor axis has been described. The coil arrangement is also shown in Fig. 1-4. The goal of the design iterations was a magnet arrangement yielding the desired field strength variation, having adequate room for plasma and neutron shielding, and satisfying the MHD criterion for interchange stability at high central cell β. (The computer code for assessing ballooning stability was not available when the coils were designed.) It was found that the interchange stability condition was strongly affected by the design of the transition coil, the final version of which is a cee-shaped coil with a 130° major arc angle. The interchange stability calculation with this transition coil yielded an upper limit of 1.38 for the central cell-to-plug β ratio. The transition coil is niobium-titanium superconductor and has a peak conductor field of about 6 T.

The outside diameter of the plug yin-yang pair is ~7.5 m. We wish to use niobium-titanium superconductor for the plug yin-yang coils also, and must therefore limit their maximum conductor field strength to about 8 T. The present design has a maximum field strength of 9 T in a very localized region at
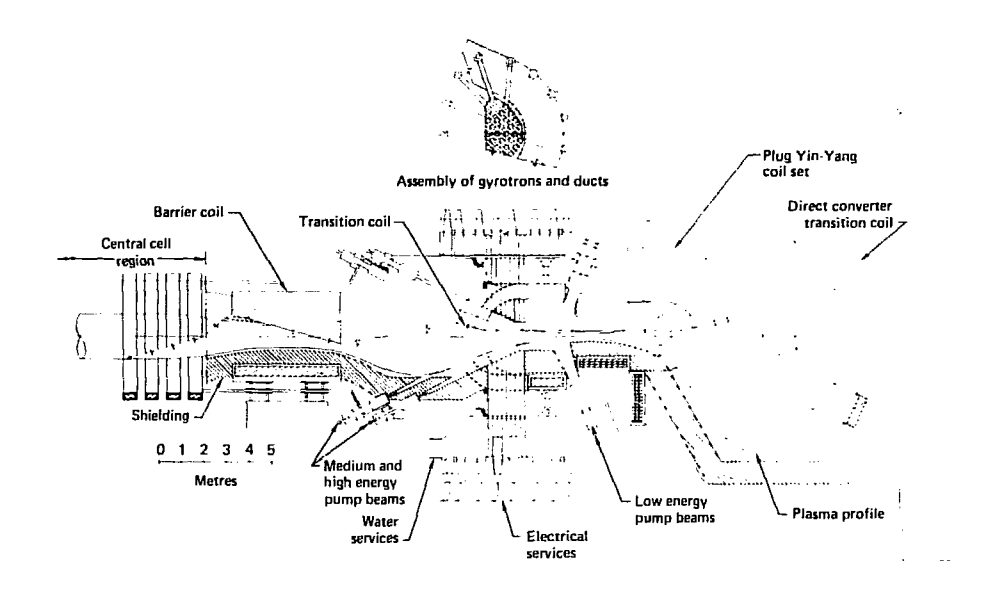
Fig. 1-4.   Tandem mirror reactor showing barrier,
transition, and plug regions.

the inside radius of the minor arc. A further spreading of the conductors in
that region should yield a reduction to 8 T.

The plug barrier coil must be of high magnetic efficiency since we want
a 12-T on-axis field and wish to use niobium-tin superconductor presently
under development for operation at ~12 T. The 4.5-m-long solenoid we designed
has an efficiency of 96% and, hence, a maximum conductor magnetic field of
12.5 T.

For comparison purposes, we designed an alternative magnet set in which
the plug coil was not required to be minimum-B. (In this more speculative

design the "anchor" for MHD stability must be provided by some other means, such as a hot electron ring in the plug, i.e., an EBT cell; we have not yet quantified the stability requirement in such a case.) There is a great simplification of the plug region for such a design. The plug coil is a pair of niobium-titanium solenoids (peak conductor field, 7.9 T) only 3.7 m in outside diameter, and the transition and circularizing cee coils are no longer needed. The plug coil conductor volume is reduced by a factor of almost 5 from the case of the yin-yang pair with two cee coils.

The magnet design is discussed more fully in Chapter 3.

End-Plug Neutral Beams

The end-plug plasmas are to be sustained by 400-keV neutral-beam injection. We designed a negative ion type neutral-beam injector that produces 1.3 MW of 400-keV neutral H^o for injection into the plasma. One injector will be used for each end plug. (Because of beam penetration, only about 0.25 MW of the injected beam will be trapped in the end-plug plasma, the remainder will enter a beam dump.)

An overall view of the injector is shown in Fig. 1-5. The H^- ions are produced by the double charge exchange method. First, 1-keV H^+ ions are extracted from a steady state positive ion source. About 20% of these ions are converted to H^- by double charge exchange in a cesium vapor cell. Several features of the cell design serve to eliminate cesium loss from the cell: the plug nozzle design, a flowing eutectic collector at -20^oC, and venetian blind collectors surrounding the cell apertures.
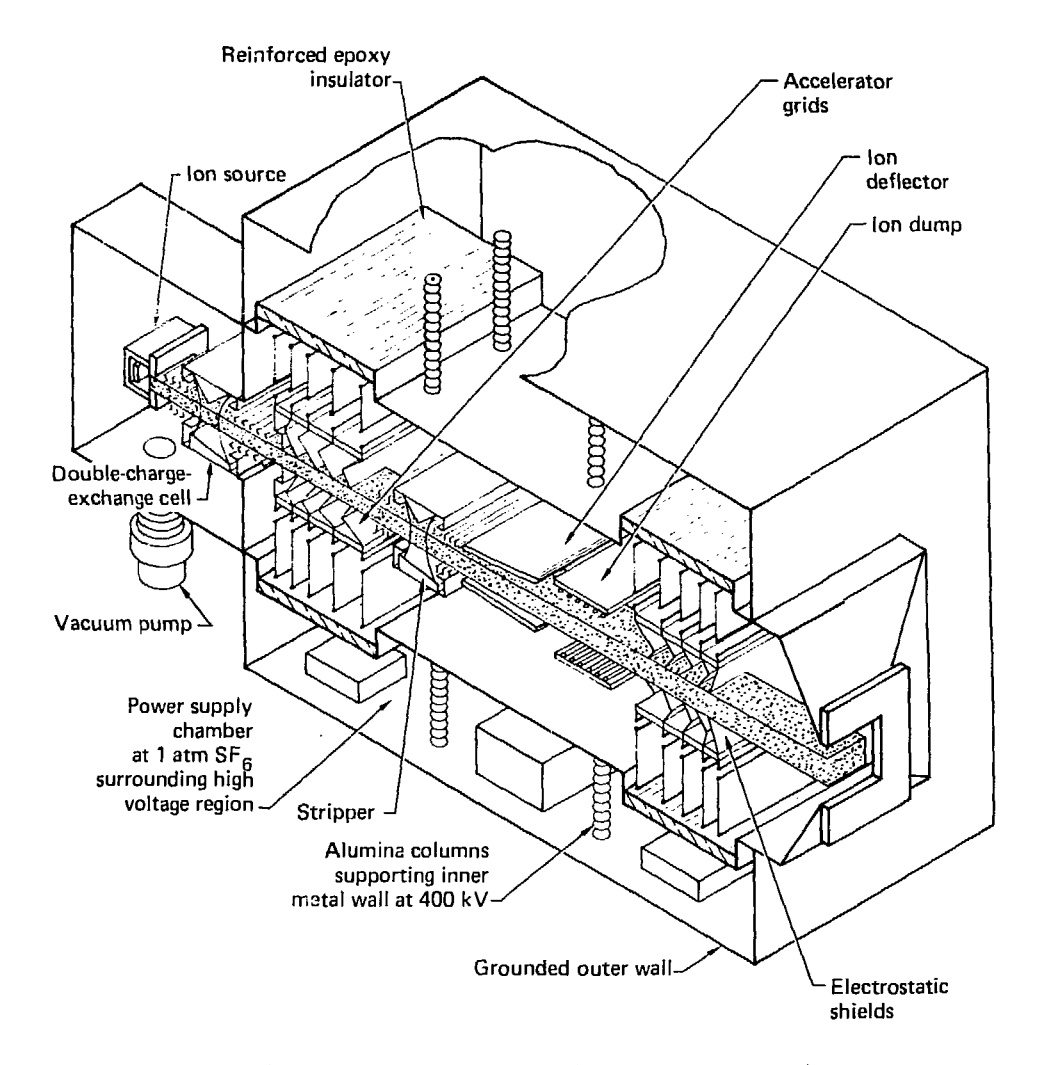
Fig. 1-5. Neutral-beam injector for plug region.

The negative ions are accelerated to 400 keV and then neutralized in a second cesium vapor cell. With line density optimized for maximum electron stripping the neutralization fraction is 0.60. The remaining ions (about half positive and half negative) are electrostatically deflected onto beam dumps.

The calculated efficiency for the plug neutral-beam injector is 53%, not including any thermal recovery of beam dump power. Thus the electrical input power requirement for each 1.3-MW injector is 2.4 MWe.

The plug neutral-beam design is discussed more fully in Chapter 4.

Barrier Pump Neutral Beams

As discussed previously, we propose the use of neutral beams to charge exchange with the thermal ions trapped in the barrier region and thereby "pump" these ions from the plasma. By proper selection of the barrier pump neutral-beam energies and injection angles, the new ions are not trapped in the barrier region, but become fuel ions for the central cell.

Analysis of the charge-exchange pumping concept has shown that to minimize the power requirements for the pump beams a multistage pumping system is desirable. In this system, decreasing fractions of the total ion load are pumped by injectors of increasing energy level (analogous to a multistage vacuum pumping system in which decreasing fractions of the total gas load are pumped at increasing vacuum levels).

Chapter 5 describes the methodology behind the design of a four-stage barrier pump system. The system consists of a gas jet to charge-exchange with those trapped ions that follow drift surfaces extending out of the main plasma column, and neutral beams at three energies: 10, 50, and 139 keV. The neutral beams are all of the positive ion type. The locations of the low-, medium-, and high-energy neutral beams are shown in Fig. 1-4.

The specific system described in Chapter 5 was designed to continuously pump a total of 1076 A of trapped ions from the two barrier regions of the reactor. This trapping rate was the result of a preliminary calculation for

the magnet system already described and is subject to change with future magnet and plasma iterations. The total neutral currents injected into the barrier region were calculated to be 615 A for the gas jet, and 697, 639, and 156 A of low-, medium-, and high-energy neutral beam, respectively. This gives a total injected current of 2107 A, nearly double the required pumping rate, largely because of the competing ionization reactions. Multiplying the currents by the beam energies gives the injected power for the pump beams, which totals 60.6 MW for all of the beams. An analysis of the performance of positive ion injectors with no energy recovery for the residual ions exiting the neutralizer yielded a total input power requirement of 119 MWe; thus the overall pump beam system efficiency is 0.51. Note that both the efficiency and the total pump beam power are very close to those in our preliminary parameter set (Figs. 1-2 and 1-3).

Electron Cyclotron Resonant Heating

Microwave heating of the electrons on the plug side of the thermal barrier is used to maintain the plug electron temperature at about 200 keV. The high plug electron temperature has two beneficial effects: it increases the plug potential and thereby the central cell ion confinement and it decreases the electron drag in the plug. The latter effect is responsible for the much reduced current and power level of the plug neutral-beam injectors.

We propose to provide the microwave power by electron cyclotron resonant heating (ECRH). Prime reasons for this choice are (1) that ECRH power can be transmitted by simple waveguides, and (2) that high power oscillators (gyrotrons) in the ECRH frequency range are now becoming available.

The ECRH power is required to balance two principal electron energy losses in the plug and transition region: (1) conduction energy transfer to those central cell electrons that pass through the thermal barrier, and (2) the introduction of cold electrons by the barrier pump neutral beams. The latter loss dominates and for the barrier pump design discussed above (and in Chapter 5) amounts to a total of 60 MW for both ends of the reactor. The conduction loss is estimated to be 18 MW. Thus, 78 MW of absorbed ECRH is required. Fortunately, as shown in Chapter 6, the absorption of ECRH power in our plasma should be essentially 100%. Thus the total injected ECRH power is 78 MW for the case considered. Note that this is somewhat less that our preliminary estimate (Figs. 1-2 and 1-3).

There is some flexibility in the choice of ECRH frequency. The frequency should be at the electron cyclotron frequency (f_{ce} = 28 B in units of GHz and T), but must be greater than the electron plasma frequency to avoid reflections from the plasma (f_{pe} = 8976 $n_e^{1/2}$ in units of Hz and cm^{-3}). Fortunately, these two conditions are mutually compatible in the tandem mirror plugs and transition region. We have chosen to introduce the ECRH in the transition region where B $\simeq$ 2T and therefore the required frequency is $\simeq$56 GHz. The locations of the ECRH gyrotrons and waveguides are shown in Fig. 1-4.

The ECRH system is discussed in more detail in Chapter 6.

Plasma Direct Converter

The most striking feature of the plasma direct converter shown in Fig. 1-1 is its circular cross section. This is made possible by the circularizing coil that is placed outside the plug yin-yang. As a result of the

flux bundle circularization, the maximum dimension of the direct converter vacuum tank is reduced.

The other unusual feature of the plasma direct converter proposed for this reactor is that it handles only the end-loss ions. The ions are preferentially lost at one end of the reactor by a slight lowering of the potential in the one plug. The electrons are preferentially lost at the other end by a relative biasing of the first grid voltages at the two ends. The advantage of this scheme is that the first grid in the plasma direct converter no longer collects all of the electron power. (In the ordinary arrangement the second grid in the direct converter repels the end-loss electrons, which then reflect back and forth through the first grid until they are finally collected.) Thus, the plasma direct converter can be designed for higher ion power density and can be more compact.

Chapter 7 describes the design of a particular direct converter that handles 180 MW of ion power. Another 205 MW of charged particle power exits at the other end of the reactor (via electrons and alpha particles) and is collected on a thermal dump. Note that the total charged particle power is 385 MW, 131 MW less than shown on our preliminary power flow diagram, Fig. 1-2. The values used in the direct converter design are from a plasma case with fusion power and Q nearly the same as Fig. 1-2, and the difference between the charged particle powers is due to the charge exchange neutral power to the wall.

The plasma direct converter has a single collector stage and two water-cooled grids and is divided into seven modules—a center module of hexagonal cross section (see Fig. 1-6) and six surrounding modules of trapezoidal shape. It is designed to handle an incident ion flux of 280 W/cm^2 and has a maximum diameter (point to point) of about 13 m. It will fit easily into the 20-m-diam vacuum vessel shown in Fig. 1-1, and probably into a smaller vessel.
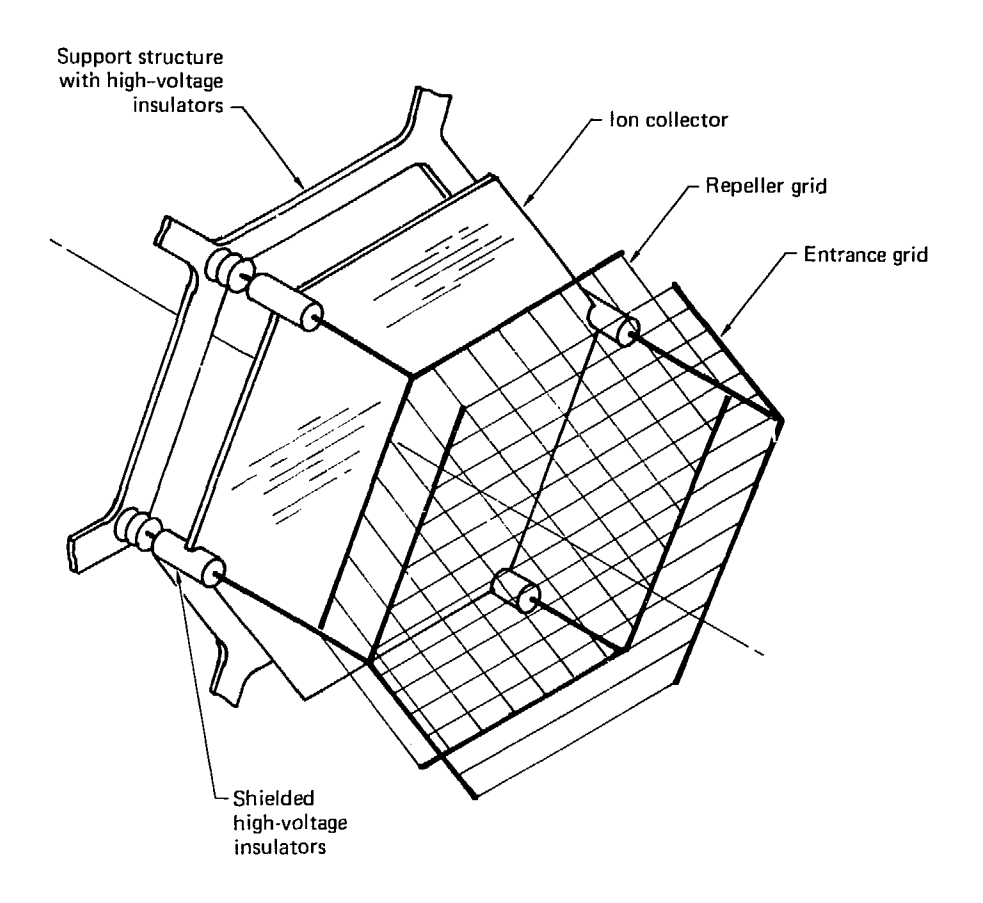
Fig. 1-6. Central module of plasma direct converter.

The calculated electrical output of the direct converter is 115 MWe; thus its operating efficiency is 64%. The electrical output is considerably less than estimated in the preliminary power flow diagram (Fig. 1-2) because of the smaller total charged particle power and because of the large electron and alpha power that is deposited on the thermal dump at the other end of the reactor. Note that if this power (205 MW) as well as the collector thermal power in the plasma direct converter (47 MW) can be thermally converted at an

efficiency of 35%, the total electrical production from the charged-particle
end loss is 203 MWe, which is only ~50 MWe short of that estimated in Fig. 1-2.

Central Cell

The design goal for the central cell is that it be compact, cost-
effective, and easily maintained. Figure 1-7 shows three adjacent central
cell modules, each 2 m in length. Each module contains an annulus of blanket
pod assemblies, a shield region, and two niobium-titanium solenoid coils.

Fig. 1-7. Three central cell modules.
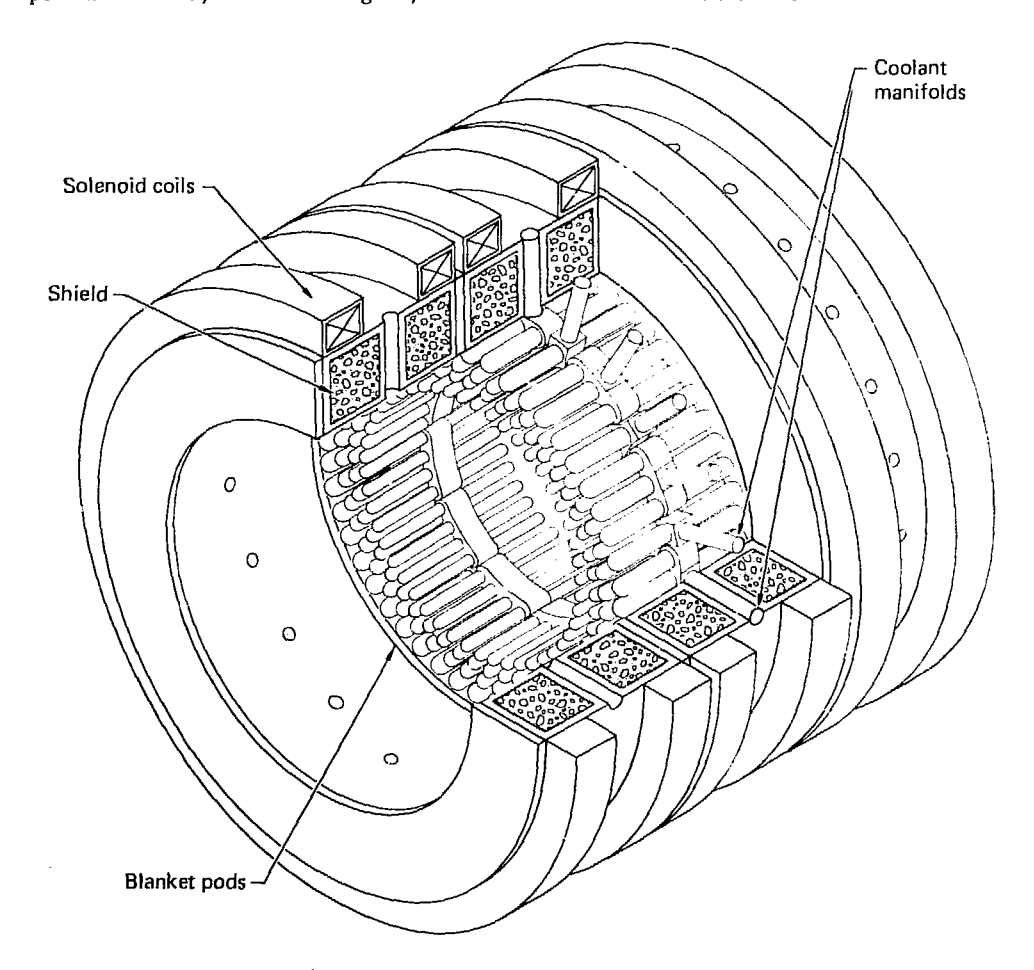
The blanket pod assemblies are arrangements of cylindrical pods mounted in coolant distributor housings. The pods contain stainless steel canisters of granulated Li_2O for neutron attenuation and tritium breeding. The can· isters, pod shells, and coolant distributor housings are all helium-cooled. The coolant inlet and outlet pipes are contained in the stems protruding through the shield from the pod assemblies. The shield is made of poured lead concrete inside a steel case.

A three-dimensional analytic model of the blanket pod assembly has been constructed for use with the Monte Carlo neutronic code TARTNP. Our neutronic calculations predict a tritium breeding ratio of over 1.1 and a blanket neutron-energy multiplication factor of about 1.05. Note that the latter value is somewhat lower than that estimated in Figs. 1-2 and 1-3.

As described previously, the central cell is housed in a vacuum trench, and intermodule seals are made by annular metal inflatable cushions in the shield region. For blanket changeout or other major maintenance the 500-tonne, central cell modules can be extracted by an overhead crane. For the repair of local blanket failures we have designed the pod assemblies so that they can be removed from inside the central cell without extracting the entire module. The defective pod assembly is removed by a remotely operated service car that travels in the bore of the central cell.

The central cell design is presented in more detail in Chapter 8.

REFERENCES

1-1. T.K. Fowler and B.G. Logan, "The Tandem Mirror Reactor," Comments Plasma Phys. 2, 167 (1977).

1-2. G.I. Dimov, V.V. Zakaidakov, and M.E. Kishinevsky, "Open Trap With Ambipolar Mirrors," Fiz. Plasmy 2, 597 (1976).

1-3. R.W. Moir, W. L. Barr, G. A. Carlson, W. L. Dexter, J. N. Doggett, J. H. Fink, G. W. Hamilton, J. E. Lee, B. G. Logan, W. S. Neef, Jr., M. A. Peterson, and M. E. Rensink, Preliminary Design Study of the Tandem Mirror Reactor, Lawrence Livermore Laboratory, Livermore, CA, UCRL-52302 (1977).

1-4. G.A. Carlson, B. M. Boghosian, J. H. Fink, J. O. Myall, and W. S. Neef, Jr., Parametric Studies of Tandem Mirror Reactors, Lawrence Livermore Laboratory, Livermore, CA, UCID-18158 (1979).

1-5. D.E. Baldwin, B.G. Logan, and T.K. Fowler, An Improved Tandem Mirror Fusion Reactor, Lawrence Livermore Laboratory, Livermore, CA, UCID-18156 (1979).

CHAPTER 2. PLASMA PHYSICS

B. G. Logan, B. M. Boghosian

In previous designs for tandem mirror reactors,[2-1] fusion ions in the center cell were axially confined by electrostatic potentials of end-plug mirror plasmas that were more dense than the plasma in the center cell—more dense in order to provide a center-cell potential well

$$\phi_c = T_e \ln \left(\frac{n_p}{n_c} \right) , \tag{2-1}$$

where n_p/n_c was the plug-to-center-cell density ratio and T_e was an assumed axially uniform electron temperature. Since ϕ_c increases only logarithmically with the density ratio n_p/n_c, whereas the ratio of center-cell fusion power density to the injection power density required to maintain the plugs varies as $(n_c/n_p)^2$, constraints on the reactor Q (Q $\gtrsim$ 5), power ($P_{net} \lesssim$ 1000 MWe), and neutron wall loading ($\Gamma \gtrsim 1$ MW/m^2) led to fairly stringent technology requirements in the plug magnetic fields ($B_{cond} \gtrsim 17$ T) and neutral-beam injection energies ($E_{inj} \gtrsim 1$ MeV). Increasing T_e by auxiliary heating of the center cell electrons improved the situation somewhat, allowing the neutral-beam energy of the plug to be decreased to about 600 keV, while Q was increased to 10 at $P_{net} = 1000$ MW(e) and $\Gamma = 0.6$ MW/m^2; however, the required plug magnetic fields were still high ($B_{mirror} > 15$ T, $B_{cond} > 20$ T).[2-2] Recent observations of axial T_e gradients in the 2XIIB experiment[2-3] have prompted consideration of the finite power/volume transferred between electrons trapped in the local plug potential well $\Delta\phi$ at temperature T_{ep} and transiting center cell electrons at temperature T_{ec} with the estimated magnitude

$$P_{cp} \approx G_e \frac{n_p^2}{(n\tau_{ee})} (T_{ep} - T_{ec}) \exp \left(-\frac{\Delta\phi}{T_{ep}} \right) , \tag{2-2}$$

where

$$(n\tau)_{ee} = \frac{8.2 \times 10^9}{\ln \Lambda_{ee}} \ [T_{ep}(keV)]^{3/2} \ cm^{-3}s \quad , \tag{2-3}$$

and G_e of order unity is a weak function of potential and mirror ratio.
(Accurate determination of this transfer rate is important for detailed re-
actor calculations and is being pursued by analytical and numerical means.)
By applying auxiliary electron heating such as electron cyclotron resonance
heating (ECRH) to the plug electrons rather than to the center-cell electrons,
and by using Eq. (2-2) with $\Delta\phi = \phi_c$ for calculating the increased local plug
electron temperature arising from the electron heating power transferred from
trapped plug electrons to passing center-cell electrons, we obtained further
improvements in neutron wall loading (to $\Gamma \gtrsim 1.2 \ MW/m^2$) at $Q = 10$ and
$P_{net} = 1000 \ MW(e)$ together with a reduction in peak plug magnetic field to
B_{cond} (max) ≈ 14 T.[2-4] These further improvements in tandem mirror reactor
(TMR) performance obtained by locating the electron heating in the plugs came
about because, for T_{ep} not too much greater than T_{ec}, the plug-to-center-cell
potential ψ_c increases roughly proportionally to the local plug electron
temperature; i.e.,

$$\phi_c \approx T_{ep} \ \ln (n_p /n_c), \ (when \ n_p > n_c). \tag{2-4}$$

Alternatively, for a given required potential well ϕ_c, the plug density n_p
could be reduced if T_{ep} were increased by heating.

A new concept called thermal barriers[2-5] promises to improve the TMR
performance much further still by exploiting a greater temperature difference
$T_{ep} - T_{ec}$ made possible by reducing the plug density n_p even below the
center-cell density n_c. Thermal barriers are localized reductions in field,
density, and potential between the center cell and the electron-heated plugs
(see Fig. 2-1). As center-cell ions pass through the peak field of the

Vacuum magnetic field, B$_{VAC}$

Central cell

End plug

Barrier region

z_{mb} z_{ob} z_{mp} z

Fig. 2-1a. Vacuum magnetic field profile.

Plasma potential, ϕ

$\phi_e + \phi_c$

ϕ_{LEPB}

ϕ_e

ϕ_{MEPB}

Trapped electrons

$\phi_{HEPB} = \phi_e - \phi_b$

z_{mb} z_{ob} z_{mp} z
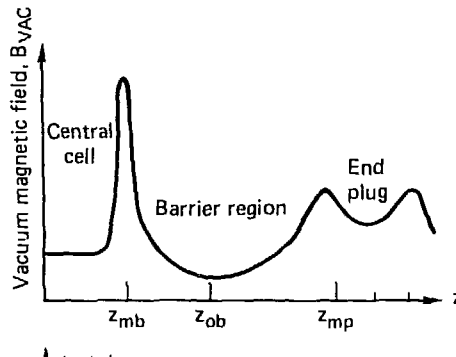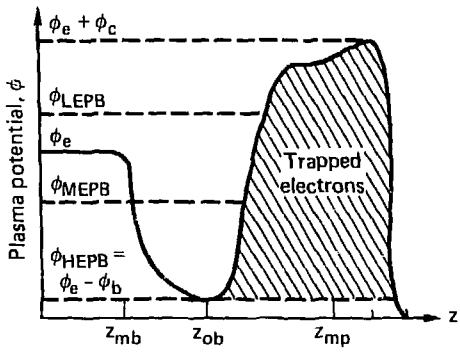
Fig. 2-1b. Plasma potential profile.

Density, n

n_c

n_p

n_b

z_{mb} z_{ob} z_{mp} z
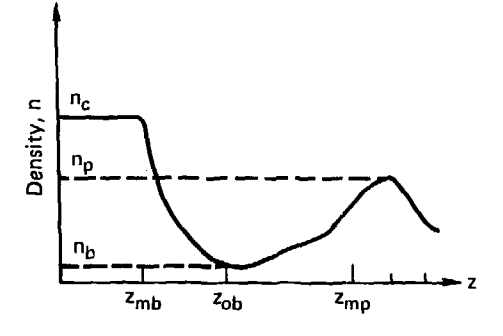
Fig. 2-1c. Ion density profile.

barrier mirror (field B_{mb} in Fig. 2-1), their density falls with the decrease in field and potential to a minimum

$$n_{pass}(b) \approx \frac{n_c \, B_b}{B_{mb}} \left(\frac{T_{ic}}{\pi \phi_b + T_{ic}} \right)^{1/2} \tag{2-5}$$

at the minimum field B_b in the barrier. Added to the density will be the density of ions trapped by collisions in the barrier region, which must be removed by some means within a collision time of order

$$\tau_{trap} \approx \frac{5 \times 10^{11} \, T_{ic}^{3/2}}{n_{pass(b)} \, \ln \Lambda} \left(\frac{1}{R_b} \right) \tag{2-6}$$

where $R_b = B_{mb}/B_b$ is the barrier mirror ratio, and T_{ic} is the temperature of the center-cell ions. If we normalize the total ion density (trapped + passing) to the density of the passing ions,

$$n_b = g_b \, n_{pass(b)} \quad , \tag{2-7}$$

a potential drop between the center cell and barrier minimum of magnitude

$$\phi_b = T_{ec} \, \ln \left(\frac{n_c}{n_b} \right) \tag{2-8}$$

occurs when $n_b < n_c$ due to removal of trapped ions (pumping). Provided n_b is also less than n_p, there is a potential rise going from the barrier to the plug given roughly by a formula similar to Eq. (2-4):

$$\phi_c + \phi_b = T_{ep} \, \ln \left(\frac{n_p}{n_b} \right) . \tag{2-9}$$

Combining Eqs. (2-8) and (2-9), we obtain

$$\frac{n_p}{n_c} \approx \exp \left(- \frac{\phi_b}{T_{ec}} + \frac{\phi_b + \phi_c}{T_{ep}} \right) \quad . \tag{2-10}$$

By heating $T_{ep} > T_{ec} (1 + \phi_c/\phi_b)$, we can achieve a plug potential greater than the center-cell potential by ϕ_c, sufficient to confine the center-cell ions, while the plug density is reduced below that of the center cell ($n_p/n_c < 1$). Then the ratio of electron heating power $\propto n_p^2$ by Eq. 2-2, using $\Delta\phi = \phi_c + \phi_b$ with thermal barriers, to the center-cell fusion power $\propto n_c^2$ is reduced relative to the case without thermal barriers for the same ϕ_c, T_{ep}, and T_{ec} by a factor of approximately

$$\frac{\left(\dfrac{n_p}{n_c}\right)^2 \begin{smallmatrix}\text{with}\\\text{thermal}\\\text{barriers}\end{smallmatrix}}{\left(\dfrac{n_p}{n_c}\right)^2 \begin{smallmatrix}\text{without}\\\text{thermal}\\\text{barriers}\end{smallmatrix}} \approx \left[\frac{\exp\left(-\dfrac{\phi_b}{T_{ec}} + \dfrac{\phi_b + \phi_c}{T_{ep}}\right)}{\exp\left(\dfrac{\phi_c}{T_{ep}}\right)}\right]^2 \approx \left(\frac{n_b}{n_c}\right)^{2[1 - (T_{ec}/T_{ep})]} \tag{2-11}$$

Note that for this factor to be desirably small, we must achieve both $n_b < n_c$ by pumping trapped ions out of the thermal barrier and also $T_{ep} > T_{ec}$ by heating electrons in the plugs, simultaneously.

The TMR reactor Q can be written in a simplified way as

$$Q \equiv \frac{P_{fusion} \ V_c}{(P_{ECRH} + P_{NB}) \ 2V_p + P_{pump} 2V_b} , \tag{2-12}$$

where P_{fusion} is the fusion power density in the center-cell volume V_c, P_{ECRH} and P_{NB} are the electron heating and neutral beam heating power densities, respectively, in the plugs of volume $2V_p$, and where P_{pump} is the power density in the barrier plasma volumes $2V_b$ required to remove the trapped ions:

$$P_{pump} \approx G_i \ \frac{n_b}{\tau_{trap}} \ \phi_b , \tag{2-13}$$

where G_i is a proportionality constant that depends on the specific pumping mechanism to be used for removing the trapped ions from the barrier. Since

P_{NB} scales with n_p^2 as well as P_{cp}, we can expect Q to improve with the addition of thermal barriers, inversely with the $(n_p/n_c)^2$ factor given by Eq. (2-11), up to the point at which P_{pump} becomes the remaining dominant term. In fact, we shall find P_{pump} $2V_b$ >> $(P_{ECRH} + P_{NB})2V_p$ once n_b << n_c is achieved with thermal barriers. The extent to which the limiting Q then given by

$$Q \approx \frac{P_{fusion}}{P_{pump}} \left(\frac{V_c}{2V_b} \right) \qquad (2-14)$$

can be greater than Q in previous TMR cases without thermal barriers depends on the efficiency of pumping [e.g., the coefficient G_i in Eq. (2-13)] and on the barrier volume V_b, which depends on the design of the magnetic field. A new pumping scheme based on a combination of charge exchange of trapped ions on neutral beams aimed within the barrier loss cone, together with bad drift orbits of some of the trapped ions ding to their radial loss[2-6], appears to be the most energy-efficient way of removing the trapped ions, as well as requiring less sophisticated technology than various other pumping schemes discussed in Ref. 2-5. The charge-exchange pumping system is described i·· more detail in Chapter 5 of this report.

Besides enhancing Q, thermal barriers are also expected to increase neutron wall loading and to reduce plug magnetic fields and injected neutral-beam current and voltage. The basic factor of reduction in $(n_p/n_c)^2$ by Eq. (2-11) for thermal barriers can be exploited two ways. The center-cell density can be increased, increasing fusion power density and correspondingly by the first-wall neutron loading Γ. A factor of about 4 higher n_c^2 from previous TMR designs should be sufficient to raise Γ to maximum economic values set by heat transfer and wall life considerations. Beyond these increases in n_c^2, we can then reduce n_p^2, allowing reductions in confining plug magnetic fields

$B_p \propto \sqrt{n_p}$. Once the maximum conductor field B_{cond} falls below 12 T, further reductions in B_p with n_p can allow increases in the plug mirror ratio $R_p = B_{mp}/B_p$, which in turn lowers the minimum neutral-beam injection energy set by the minimum cutoff energy

$$E_{inj} > E_{cutoff} = \frac{\phi_c + \phi_e}{R_p - 1} \tag{2-15}$$

that can be confined by the mirrors against the outer plug potential drop $\phi_c + \phi_e$. Perhaps the most important technology relaxation made possible by thermal barriers, however, is the reduction in neutral-beam current $\propto n_p^2$. For given beam access area through the magnets, reductions in total beam current allow reductions in the beam current density J_B, easing dc beam source design, electric fields in the accel gaps (gap spacing $d \propto 1/\sqrt{J_B}$), and grid-sputtering lifetimes. Alternatively, lower beam currents would permit smaller individual beam sizes, easing gas pumping, stored electrostatic energy, and beam dump problems. Ultimately, it may be possible to reduce individual beam sizes to less than 1 A each, where well established accelerator technology such a linacs could be used for voltages above a few hundred keV. Finally, sufficient reductions in neutral-beam power with thermal barriers will relax efficiency and cost/watt requirements.

DESCRIPTION OF THE PLASMA MODEL

Definitions and Nomenclature

Figures 2-1(a), (b), and (c) display the vacuum magnetic field profile, ambipolar potential profile, and ion density profile at one end of the barrier cell TMR. The barrier cell is the region between z_{bm} (barrier mirror) and z_{pm}

(inboard plug mirror); the transition region is the subset of the barrier cell lying between z_{b0} (barrier midplane) and z_{pm}. The ion density of the central cell is n_c, that at the barrier midplane is n_b, and that at the plug midplane is n_p. The temperature of central-cell ions is T_c, that of passing electrons is T_{ec}, and that of trapped (plug and transition region) electrons is T_{ep}.

The quantities $n^*(z)$, $n_{pass}(z)$, $B^*_{vac}(z)$, $\phi^*(z)$, and $\beta^*(z)$ are the total ion density, passing ion density, vacuum magnetic field, ambipolar potential, and perpendicular beta within the barrier-cell region, respectively. Thus, by definition:

$$n^*(z_{bm}) = n_{pass}(z_{bm}) = n_c \quad ,$$

$$n^*(z_{b0}) = n_b \quad ,$$

$$B^*_{vac}(z_{bm}) = B_{bm,vac} \quad ,$$

$$B^*_{vac}(z_{b0}) = B_{b0,vac} \quad , \tag{2-16}$$

$$B^*_{vac}(z_{pm}) = B_{pm,vac} \quad ,$$

$$\phi^*(z_{bm}) = \phi_e \quad ,$$

and

$$\phi^*(z_{b0}) = \phi_e - \phi_b \quad .$$

36

The function $g_b(z)$ is defined as the ratio of total ion density to passing ion density in the barrier cell:

$$g_b(z) = n^*(z)/n_{pass}(z) \quad . \tag{2-17}$$

Note that $g_b(z_{bm}) = 1$ since there can be no trapped ions at the barrier mirror. The quantity

$$g_{b0} \equiv g_b(z_{b0}) > 1$$

is a measure of pumping effectiveness, and approaches 1 from above as the pumping improves (fewer ions trapped in barrier). The following model is used for the $g_b(z)$ profile:

$$g_b(z) = 1 + (g_{b0} - 1) \; \frac{\left[1 - \dfrac{B^*_{vac}(z)}{B_{bm,vac}}\right]}{\left[1 - \dfrac{B_{b0,vac}}{B_{bm,vac}}\right]} \quad ; \tag{2-18}$$

that is, g_b is assumed to vary linearly with B^*_{vac}.

Finally, we note that the plasma magnetic field in the barrier cell is given by

$$B^*_{pla}(z) = B^*_{vac}(z) \; [1 - \beta^*(z)]^{1/2} \quad , \tag{2-19}$$

and that the barrier-cell vacuum and plasma mirror ratios are given by

$$R_{b,vac} \equiv B_{bm,vac}/B_{b0,vac} \quad , \tag{2-20a}$$

and

$$R_b \equiv B_{bm,pla}/B_{b0,pla} \quad , \tag{2-20b}$$

respectively.

Other miscellaneous definitions: The energy of alpha particles born in fusion reactions (3.52 MeV) is denoted by E_α, and the fractions of this super-thermal alpha energy imparted to electrons and ions are given by

$$f_{\alpha e} \approx 0.8816 \exp (-T_{ec}/67.40) \quad , \tag{2-21a}$$

and

$$f_{\alpha i} \approx 1.0 - 0.9080 \exp (-T_{ec}/101.7) \quad , \tag{2-21b}$$

respectively. (Note that the two expressions do not add up to unity because of superthermal alphas that scatter into the loss cone while slowing down.) The fusion neutron energy (14.06 MeV) is denoted by E_n, and the total fusion energy release (17.58 MeV) is denoted by E_{FUS}. The fusion reaction rate averaged over a Maxwellian plasma is modeled by[2-7]

$$\langle \sigma v \rangle_{DT} \approx \frac{3.05 \times 10^{-13} \exp \left(-17.7/T_c^{0.348}\right)}{\left(1.0 + 0.1554 \, T_c^{1/3} - 0.1418 \, T_c^{2/3} - 0.05 \, T_c + 0.0364 \, T_c^{4/3}\right)} \tag{2-22}$$

Finally, all units are in the CGS system, except energies which are in keV, currents which are in amps, and powers which are in MW, unless otherwise specified.

Determination of Potentials and Densities in the Thermal Barrier

The Maxwell-Boltzmann relation between central-cell electrons and barrier-cell electrons at $z \leq z_{b0}$ is given by

$$n^*(z) = n_c \exp \left(- \frac{\phi_e - \phi^*(z)}{T_{ec}} \right) \quad \text{for } z \leq z_{b0} \quad . \tag{2-23}$$

A specific case of Eq. (2-23) is

$$n_b = n_c \exp \left(- \frac{\phi_b}{T_{ec}} \right) \tag{2-24}$$

The Maxwell-Boltzmann relation between plug electrons and barrier-cell electrons at $z \geq z_{b0}$ is given by

$$n^*(z) = n_p \exp \left(- \frac{\phi_e + \phi_c - \phi^*(z)}{T_{ep}} \right) \quad \text{for } z \geq z_{b0} \tag{2-25}$$

A specific case of Eq. (2-25) is

$$n_b = n_p \exp \left(- \frac{\phi_c + \phi_b}{T_{ep}} \right) \quad \text{for } z \geq z_{b0} \quad . \tag{2-26}$$

Next, we note that conservation of momentum of passing ions between the central cell and the barrier cell yields the relationship

$$n_{pass}(z) \approx n_c \frac{B_{pla}^*(z)}{B_{mb,pla}} \left\{ \frac{T_c}{\pi[\phi_e - \phi^*(z)] + T_c} \right\}^{1/2} \quad \text{for } \phi^* \le \phi_e \quad . \quad (2\text{-}27)$$

A specific case of Eq. (2-27) is

$$n_{pass}(z_{b0}) \cdot g_{b0} = n_b = n_c \left(\frac{g_{b0}}{R_b} \right) \left(\frac{T_c}{\pi\phi_b + T_c} \right)^{1/2} \quad . \quad (2\text{-}28)$$

Next, we apply the Maxwell-Boltzmann relation between passing ions in the central cell and passing ions in the barrier cell to get

$$n_{pass}(z) = n_c \frac{B_{pla}^*(z)}{B_{mb,pla}} \left[\frac{\exp\left(-\dfrac{\phi^*(z) - \phi_e}{T_c}\right) - \exp\left(-\dfrac{\phi_c}{T_c}\right)}{1 - \exp\left(-\dfrac{\phi_c}{T_c}\right)} \right] \text{for } \phi^* > \phi_e \quad ,$$

$$(2\text{-}29)$$

where the factor $B^*(z)/B_{mb,pla}$ has been inserted because the passing ions are not isotropic, but rather are only found within the barrier-cell loss cone. We note that Eq. (2-29) matches Eq. (2-27) when $\phi^* = \phi_e$; indeed, this is how we selected the regimes of validity of Eqs. (2-27) and (2-29). The factors $\exp(-\phi_c/T_c)$ are required for the density of passing ions to go to zero at the plug mirror ($\phi^* = \phi_e + \phi_c$). An unmodified Maxwell-Boltzmann exponential factor could not do this simply because the passing-ion distribution is not Maxwellian (our modification is tantamount to cutting off the Maxwellian tail at $\frac{1}{2}MV_\parallel^2 = \phi_c$). This form exhibits the proper behavior as $\phi^* \to \phi_e + \phi_c$ as well as when $\phi^* \to \phi_e$.

The perpendicular ion temperature in the barrier is assumed to be (T_c/R_b), so $\beta^*(z)$ is given by the following equations:

$$\beta^*(z) = \frac{n^*(z) \ (T_c/R_b) + n^*(z) \ T_{ec}}{[B^*_{vac}(z)]^2/2\mu_0} \quad \text{if } z < z_{b0} \ , \qquad (2\text{-}30a)$$

and

$$\beta^*(z) = \frac{n^*(z) \ (T_c/R_b) + [n^*(z) - n_b] \ T_{ep} + n_b \ T_{ec}}{[B^*_{vac}(z)]^2/2\mu_0} \quad \text{if } z > z_{b0} \ .$$

$$(2\text{-}30b)$$

The following is a convenient formulary resulting from algebraic manipulations of the preceding equations. The first of these, Eq. (2-31), is a transcendental equation for ϕ_b, and is obtained by combining Eqs. (2-24) and (2-28) to eliminate n_b. The second, Eq. (2-32), is the equation for ϕ_c, and is obtained by combining Eqs. (2-24) and (2-25) to eliminate n_b. Equations (2-33) follow from Eqs. (2-17), (2-19), (2-27), and (2-29). Equations (2-34) follow from Eqs. (2-23) and (2-25). Equations (2-35) are a restatement of Eqs. (2-30). Together, Eqs. (2-33), (2-34), and (2-35) constitute three equations for the three unknowns $n^*(z)$, $\phi^*(z)$, and $\beta^*(z)$, assuming $B^*_{vac}(z)$ is given, at every point in the barrier cell.

$$\left(\frac{\phi_b}{T_c}\right) = \frac{T_{ec}}{T_c} \ \ln \left\{ \frac{R_b}{g_{b_0}} \left[1 + \pi\left(\frac{\phi_b}{T_c}\right)\right]^{1/2} \right\} \ , \qquad (2\text{-}31)$$

$$\phi_c = T_{ep} \ \ln \left(\frac{n_p}{n_c}\right) + \left(\frac{T_{ep}}{T_{ec}} - 1\right) \phi_b \ , \qquad (2\text{-}32)$$

$$n^*(z) = g_b(z) \ n_c \ \frac{B^*_{vac}(z)}{B_{mb,pla}} \ [1 - \beta^*(z)]^{1/2} \left\{ \frac{T_c}{\pi[\phi_e - \phi^*(z)] + T_c} \right\}^{1/2} \quad \text{for } \phi^* \leq \phi_e \ , $$

$$(2\text{-}33a)$$

41

$$n^*(z) = g_b(z) n_c \frac{B^*_{vac}(z)}{B_{mb,pla}} [1 - \beta^*(z)]^{1/2} \left[\frac{\exp\left(-\dfrac{\phi^*(z) - \phi_e}{T_c}\right) - \exp\left(-\dfrac{\phi_c}{T_c}\right)}{1 - \exp\left(-\dfrac{\phi_c}{T_c}\right)} \right]$$

$$\text{for } \phi^* > \phi_e \quad , \quad (2\text{-}33b)$$

$$\phi^*(z) = \phi_e - T_{ec} \ln [n_c/n^*(z)] \quad \text{for } z \leq z_{b0} \quad , \tag{2-34a}$$

$$\phi^*(z) = \phi_e + \phi_c - T_{ep} \ln [n_p/n^*(z)] \quad \text{for } z \geq z_{b0} \quad , \tag{2-34b}$$

$$\beta^*(z) = [n^*(z)\,(T_c/R_b) + n^*(z)\,T_{ec}] \Big/ \left\{ [B^*_{vac}(z)]^2 \Big/ 2\mu_0 \right\} \quad \text{for } z \leq z_{b0}, \tag{2-35a}$$

$$\beta^*(z) = \left\{ n^*(z)\,(T_c/R_b) + [n^*(z) - n_b]\,T_{ep} + n_b T_{ec} \right\} \Big/ \left\{ [B^*_{vac}(z)]^2 \Big/ 2\mu_0 \right\}$$

$$\text{for } z \geq z_{b0} \quad . \tag{2-35b}$$

Thus, given a magnetic field profile $B^*_{vac}(z)$, it is possible to determine the density, potential, and beta profiles as well. The radius of the barrier cell at any point is given by the equation for conservation of magnetic flux:

$$\pi r_c^2 \, B_{cc,vac} \, (1 - \beta_c)^{1/2} = \pi [r^*(z)]^2 \, B^*_{vac}(z) \, [1 - \beta^*(z)]^{1/2} \quad .$$

Therefore,

$$r^*(z) = r_c \left[\frac{B_{cc,vac}}{B^*_{vac}(z)} \left(\frac{1 - \beta_c}{1 - \beta^*(z)} \right)^{1/2} \right]^{1/2} \quad . \tag{2-36}$$

A differential volume element in the barrier cell is then

$$dV^* = \pi [r^*(z)]^2 \, dz = \frac{B_{cc,vac}}{B^*_{vac}(z)} \left(\frac{1 - \beta_c}{1 - \beta^*(z)} \right)^{1/2} \pi r_c^2 \, dz \quad . \tag{2-37}$$

Finally, we present the central-cell beta equation and field reduction:

$$\beta_c = \frac{n_c T_c + n_c T_{ec} + P_\alpha^{superthermal}}{(B^2_{cc,vac}/2\mu_0)} \quad , \tag{2-38}$$

and

$$B_{cc,pla} = B_{cc,vac} (1 - \beta_c)^{1/2} \quad , \tag{2-39}$$

where the superthermal alpha pressure is modeled

$$P_\alpha^{superthermal} \approx 8.3 \times 10^{10} \, n_c <\sigma v>_{DT} T_{ec}^{3/2} \, E_\alpha \, f_{\alpha e} \quad . \tag{2-40}$$

Trapped Ion Pumping in the Thermal Barrier

The rate at which passing ions trap in the barrier cells per unit barrier-cell volume is given by the following equation, which has been fitted to Fokker-Planck results:

$$J_{trap} \approx \frac{[n_{pass}(z)]^2}{5.5 \times 10^9 \, T_c^{3/2}} \left(1 + 0.55 \frac{B_{mb,pla}}{B^*_{pla}(z)} \right) \quad . \tag{2-41}$$

So the total current at which passing ions trap in the barrier cells is

$$I_{trap} = 2e \int_{z_{bc}}^{z_{pm}} \frac{[n_{pass}(z)]^2}{5.5 \times 10^9 \, T_c^{3/2}} \left(1 + 0.55 \frac{B_{mb,pla}}{B^*_{pla}(z)} \right) dV^* \quad , \tag{2-42}$$

where e is the electronic charge, the factor of 2 accounts for both ends of the machine, and the lower limit of integration is taken to be z_{bc} instead of z_{bm} because Eq. (2-43) is not valid (does not approach correct limit) as

$z \rightarrow z_{bm}$. The cutoff, z_{bc}, is defined as that point at which the fraction of velocity space available for trapped particles becomes so small that no greater a value of $g_b(z)$ than g_{b0} is possible. This is defined by

$$B_{pla}^*(z_{bc}) = \left(\frac{2 \ g_{b0} - 1}{g_{b0}^2} \right) B_{mb,pla} \quad .$$ (2-43)

Trapped ions that are far enough away from the axis in the barrier cell will have drift surfaces that extend well beyond the plasma boundary. Thus, the barrier-cell plasma will be surrounded by a "halo" of trapped particles. A gas feed into this halo may thus remove some of these trapped particles by either charge exchange or ionization.[2-6] The fraction of trapped particles that may be so removed by a gas feed is denoted by f_D. Thus, we define the gas feed current:

$$I_{GP} = f_D \ I_{trap} \quad .$$ (2-44)

The remaining trapped ions, those are not removed by the gas feed, are pumped by three neutral beams [see Figure 2-1(b)]. On the barrier cell's outboard side (the transition region) there is a low-energy pump beam at $z = z_{LEPB}$, at the barrier midplane there is a high-energy pump beam at $z = z_{HEPB} = z_{b0}$, and on the barrier cell's inboard side is a medium energy pump beam at $z = z_{MEPB}$. We define

$$\phi_{LEPB} \equiv \phi^*(z_{LEPB}) \quad ,$$ (2-45a)

$$\phi_{MEPB} \equiv \phi^*(z_{MEPB}) \quad ,$$ (2-45b)

and

$$\phi_{HEPB} \equiv \phi^*(z_{HEPB}) = \phi_e - \phi_b \quad .$$ (2-45c)

These three energetic pump beams must remove the trapping current $(1 - f_D)I_{TRAP}$ that is not removed by the gas pump. They do this by charge exchanging with trapped ions in the barrier cell, thus producing a passing ion (since the beams are aimed within the loss cone angle of the barrier cell), and a neutral which leaves the plasma.[*] The required charge exchange currents are thus

$$
I_{LEPB}^{cx} = (1 - f_D) \, f_{LEPB} \left[\frac{n^*(z_{LEPB})}{n^*(z_{LEPB}) - n_{pass}(z_{LEPB})} \right] I_{trap} \quad , \quad (2\text{-}46a)
$$

$$
I_{MEPB}^{cx} = (1 - f_D) \, f_{MEPB} \left[\frac{n^*(z_{MEPB})}{n^*(z_{MEPB}) - n_{pass}(z_{MEPB})} \right] I_{trap} \quad , \quad (2\text{-}46b)
$$

and

$$
I_{HEPB}^{cx} = (1 - f_D) \, f_{HEPB} \left[\frac{n^*(z_{HEPB})}{n^*(z_{HEPB}) - n_{pass}(z_{HEPB})} \right] I_{trap} \quad , \quad (2\text{-}46c)
$$

where

$$
f_{LEPB} + f_{MEPB} + f_{HEPB} = 1 \quad . \tag{2-47}
$$

The fractions f_{LEPB}, f_{MEPB}, and f_{HEPB} determine the way in which the total required pumping current is divided among the three energetic beams. The density ratios in square brackets in Eqs. (2-46) are ratios of total ions to trapped ions in the barrier; these are necessary because the beams will

---

[*]Some of the neutrals from charge exchange of the trapped ions reionize before escape; however, we estimate that the additional neutrals (besides beam neutrals) from charge exchange of passing ions will largely offset the reionization of trapped ions which charge exchange. Thus, we make the approximation here that all trapped ions which charge exchange, escape.

charge exchange with passing ions as well as trapped ions, though the former type of occurrence does not pump.

It must be borne in mind that I^{cx}_{LEPB}, I^{cx}_{MEPB}, and I^{cx}_{HEPB} are charge exchange currents; the total beam currents (trapped in plasma) are given by

$$I_{LEPB} = (1 - f_D) \ f_{LEPB} \ \left[\frac{g_b(z_{LEPB})}{g_b(z_{LEPB}) - 1} \right] \ \left(1 + \frac{<\sigma v>^{ion}_{LEPB}}{<\sigma v>^{cx}_{LEPB}} \right) I_{TRAP} \quad , \tag{2-48a}$$

$$I_{MEPB} = (1 - f_D) \ f_{MEPB} \ \left[\frac{g_b(z_{MEPB})}{g_b(z_{MEPB}) - 1} \right] \ \left(1 + \frac{<\sigma v>^{ion}_{MEPB}}{<\sigma v>^{cx}_{MEPB}} \right) I_{TRAP} \quad , \tag{2-48b}$$

and

$$I_{HEPB} = (1 - f_D) \ f_{HEPB} \ \left[\frac{g_b(z_{HEPB})}{g_b(z_{HEPB}) - 1} \right] \ \left(1 + \frac{<\sigma v>^{ion}_{HEPB}}{<\sigma v>^{cx}_{HEPB}} \right) I_{TRAP} \quad , \tag{2-48c}$$

where we have used Eq. (2-17). The portions of these currents that are ionized are used to fuel the central cell; this will be important when we write the particle and energy balance equations. For now, we define

$$I^{ion}_{LEPB} = I_{LEPB} - I^{cx}_{LEPB} \quad , \tag{2-49a}$$

$$I^{ion}_{MEPB} = I_{MEPB} - I^{cx}_{MEPB} \quad , \tag{2-49b}$$

and

$$I^{ion}_{HEPB} = I_{HEPB} - I^{cx}_{HEPB} \quad . \tag{2-49c}$$

The injection energies of the three beams are denoted by V_{LEPB}, V_{MEPB}, and V_{HEPB}. The requirement that ions produced by ionization and charge ex-

change of these beams be passing ions (i.e., that they be in the barrier-cell loss cone) sets lower bounds on V_{MEPB} and V_{HEPB} and an upper bound on V_{LEPB}. These bounds may be written

$$V_{LEPB} < \frac{\phi_{LEPB} - \phi_e}{\left\{\left[\frac{B_{mb,pla}}{B_{pla}^*(z_{LEPB})}\right] \sin^2 \theta_{LEPB}^{inj} - 1\right\}} , \quad (2\text{-}50a)$$

$$V_{MEPB} \gtrsim \frac{\phi_e - \phi_{MEPB}}{\left\{1 - \left[\frac{B_{mb,pla}}{B_{PLA}^*(z_{MEPB})}\right] \sin^2 \theta_{MEPB}^{inj}\right\}} , \quad (2\text{-}50b)$$

and

$$V_{HEPB} \gtrsim \frac{\phi_e - \phi_{HEPB}}{\left\{1 - \left[\frac{B_{mb,pla}}{B_{pla}^*(z_{HEPB})}\right] \sin^2 \theta_{HEPB}^{inj}\right\}} , \quad (2\text{-}50c)$$

where θ_{LEPB}^{inj}, θ_{MEPB}^{inj}, and θ_{HEPB}^{inj} are the injection angles of the low-, medium-, and high-energy pump beams, respectively. Of course, these injection angles must be within the loss cone, so, in the latter two cases, it must be further specified that

$$\theta_{MEPB}^{inj} \leq \arcsin \left[\frac{B_{pla}^*(z_{MEPB})}{B_{mb,pla}}\right]^{1/2} , \quad (2\text{-}51a)$$

and

$$\theta_{HEPB}^{inj} \leq \arcsin \left(\frac{1}{\sqrt{R_b}}\right) . \quad (2\text{-}51b)$$

Finally, the pumping power necessary is given by

$$P_{PUMP} = (I_{LEPB} V_{LEPB} + I_{MEPB} V_{MEPB} + I_{HEPB} V_{HEPB})/1000.0 , \quad (2\text{-}52)$$

47

where the factor of 1000.0 yields an answer in MW, since the currents are in amperes, and the energies are in keV.

Plug Model

The plug model used is essentially identical to that developed by Logan and Rensink in 1978, and used in previous TMR studies at Livermore. The model is an analytic fit to Fokker-Planck studies of plug mirror confinement.

Let the potential drop seen by the plug ions be denoted by ϕ_p. Thus

$$\phi_p = \phi_e + \phi_c \quad . \tag{2-53}$$

The plug vacuum mirror ratio and plug plasma mirror ratio are given by

$$R_{p,vac} \equiv B_{mp,vac}/B_{0p,vac} \tag{2-54a}$$

and

$$R_p \equiv B_{mp,pla}/B_{0p,pla} \quad , \tag{2-54b}$$

respectively. There is no field reduction at the plug mirror, and the "long-thin approximation" is used at the plug midplane:

$$B_{mp,pla} = B_{mp,vac} \quad , \tag{2-55a}$$

and

$$B_{0p,pla} = B_{0p,vac} \; (1 - \beta_p)^{1/2} \tag{2-55b}$$

First we define

$$E_c \equiv \frac{\phi_p}{R_p \sin^2 \theta_{inj} - 1} \quad , \tag{2-56}$$

and

$$R_{p,eff} \equiv \frac{R_p \sin^2 \theta_{inj}}{1 + (\phi_p/E_{p,inj})} \quad , \tag{2-57}$$

where θ_{inj} is the injection angle of the plug neutral beam, and $E_{p,inj}$ is the injection energy of the plug neutral beams, respectively. Then we calculate

$$\ln \Lambda_{ei} \approx \ln (5.7 \times 10^{13} \, T_{ep}/\sqrt{n_p}) \quad , \tag{2-58a}$$

and

$$\ln \Lambda_{ii} \approx \ln [1.4 \times 10^{15} \, (T_{ep} \, E_p/n_p)^{1/2}] \quad , \tag{2-58b}$$

where E_p is the plug ion energy (for which one must provide an initial guess to begin this calcuation).

Next, we solve the following two equations numerically for $(\overline{E}_L/E_{p,inj})$ and (τ_{ii}/τ_{drag}):

$$\left(\frac{\overline{E}_L}{E_{p,inj}}\right) = \frac{1 + (E_c/E_{p,inj}) \, (\tau_{ii}/\tau_{drag})}{1 + (\tau_{ii}/\tau_{drag})} \quad , \tag{2-59}$$

and

$$\left(\frac{\tau_{ii}}{\tau_{drag}}\right) = \frac{0.156}{\sqrt{A_p}} \left(\frac{E_{p,inj}}{T_{ep}}\right)^{3/2} \frac{\log_{10} (R_{p,eff})}{\ln[1/(\overline{E}_L/E_{p,inj})]} \left(\frac{\ln \Lambda_{ei}}{\ln \Lambda_{ii}}\right) , \tag{2-60}$$

where A_p is the plug ion mass in AMU. Then we calculate

$$(n\tau)_{drag} = 1.0 \times 10^{13} \, A_p T_{ep}^{3/2}/\ln \Lambda_{ei} \quad , \tag{2-61}$$

$$(n\tau)_p^{ii} \equiv 2.76 \times 10^{12} \, \sqrt{A_p} \, E_{p,inj}^{3/2} \, \log_{10} (R_{p,eff})/\ln \Lambda_{ii} \quad , \tag{2-62}$$

$$(n\tau)_p^{ei} \equiv 1.0 \times 10^{13} \, A_p \, T_{ep}^{3/2} \, \ln [1/(\overline{E}_L/E_{inj})]/\ln \Lambda_{ei} \quad , \tag{2-63}$$

and

$$(n\tau)_p = \left[\frac{1}{(n\tau)_p^{ii}} + \frac{1}{(n\tau)_p^{ei}} \right]^{-1} \quad . \tag{2-64}$$

To complete the iterative process, we use the ion energy balance of the plug
(neglecting charge exchange) to solve for

$$E_p = \frac{3}{2} T_{ep} + \frac{(n\tau)_{drag}}{(n\tau)_p} (E_{p,inj} - \overline{E}_L) \quad . \tag{2-65}$$

This new value of E_p is then inserted back into Eq. (2-58b), and the entire
process is repeated until it converges onto a self-consistent set of param-
eters. At very high values of T_{ep}, such as are encountered in tandem mir-
rors with barrier cells, it has been found that the Logan-Rensink plug model
can yield anomalously high values of E_p. Consequently, in this study, if
we obtain $E_p > 2.5\ E_{p,inj}$, we set $E_p = 2.5\ E_{p,inj}$ before beginning the next
iteration. In this way, we ensure $E_p \leq 2.5\ E_{p,inj}$.

The particle balance equation for the plug ions may be written

$$I_{p,inj} = e \frac{n_p^2}{(n\tau)_p} \cdot \left(\frac{4\pi}{3} r_p^3 \right) \quad , \tag{2-66}$$

where $I_{p,inj}$ is the neutral beam current into one plug, e is the electronic
charge, and r_p is the plug radius given by conservation of magnetic flux:

$$r_p = r_c \left[\frac{B_{cc,vac}}{B_{0p,vac}} \left(\frac{1 - \beta_c}{1 - \beta_p} \right)^{1/2} \right]^{1/2} \quad . \tag{2-67}$$

The total neutral-beam power into both plugs is then

$$P_{NB} = (2\ I_{p,inj}\ E_{p,inj})/1000.0 \quad , \tag{2-68}$$

where the factor of 2 accounts for both ends of the machine, and the factor of 1000.0 yields an answer in MW, since $I_{p,inj}$ is in amperes and $E_{p,inj}$ is in keV.

Finally, we present the plug beta equation:

$$\beta_p = \frac{n_p (0.9 E_p) + n_p T_{ep}}{(B_{0p,vac}^2 / 2\mu_0)} \quad , \tag{2-69}$$

where the factor of 0.9 accounts for the fact that most of the plug ion energy is perpendicular (the factor would be 2/3 for a perfectly isotropic plasma).

The Particle and Energy Balance Equations

The particle balance of the central-cell ions is written[*]

$$\frac{n_c^2 V_c}{(n\tau)_c} + \frac{1}{2} n_c^2 <\sigma v>_{DT} V_c + I_{GP} = I_{LEPB}^{ion} + I_{MEPB}^{ion} + I_{HEPB}^{ion} + I_{AUX}^{ion} \quad , \tag{2-70}$$

where

$$I_{AUX}^{ion} \equiv \frac{<\sigma v>_{AUX}^{ion}}{<\sigma v>_{AUX}^{ion} + <\sigma v>_{AUX}^{cx}} I_{AUX} \tag{2-71a}$$

and

$$I_{AUX}^{cx} \equiv \frac{<\sigma v>_{AUX}^{cx}}{<\sigma v>_{AUX}^{ion} + <\sigma v>_{AUX}^{cx}} I_{AUX} \tag{2-71b}$$

comprise an auxiliary fuel source located at the central-cell potential,

$$(n \tau)_c \approx 5.547 \times 10^{11} \frac{g(R_{ci}/2)}{\ln \Lambda_{ii}} T_c^{3/2} \left(\frac{\phi_c}{T_c}\right) \exp\left(\frac{\phi_c}{T_c}\right) \tag{2-72}$$

---

[*]Throughout this section, we neglect radial loss compared to end loss for DT fuel ions as well as electrons. No thermal alpha population is assumed to be present.

is the Pastukhov $(n\tau)$,

$$R_{ci} \equiv B_{0p,pla}/B_{cc,pla} \quad , \qquad (2\text{-}73)$$

$$\ln \, \Lambda_{ii} = \ln \, \left[3.08 \times 10^{14} \left(\frac{T_c^{3/2}}{n_c^{1/2}} \right) \right] , \qquad (2\text{-}74)$$

and

$$g(x) \equiv \frac{\sqrt{\pi}}{2} \left(1 + \frac{1}{x} \right)^{1/2} \ln \left\{ \left[\left(1 + \frac{1}{x} \right)^{1/2} + 1 \right] \Big/ \left[\left(1 + \frac{1}{x} \right)^{1/2} - 1 \right] \right\} \quad . \quad (2\text{-}75)$$

The first term on the left-hand side of Eq. (2-70) is the Pastukhov end loss of central-cell ions, and the second term is the ion burnup rate in fusion reactions. The third term on the left-hand side of Eq. (2-70) reflects the following fact: The current of passing ions that becomes trapped is, in steady-state, exactly equal to the current of trapped ions that is pumped back into passing space minus the current of trapped ions that is pumped by the gas feed. Any trapped ion that either ionizes or charge exchanges with the gas feed produces an ion that, being born on a flux surface so far outside of the plasma, is essentially lost from the plasma. Thus, the entire gas-feed current is a drain on the central-cell ion population.

The first three terms on the right-hand side of Eq. (2-70) are the fueling due to the pump beams, and the last term on the right-hand side is the ionization current of an auxiliary fueling source. It may be preferable to do all fueling via the pump beams, in which case this term would be equal to zero.

The central-cell ion energy balance may be written (note: $E_{c,inj}$ may be zero if, for example, pellets are used for auxiliary fueling):

$$\frac{1}{4} n_c^2 <\sigma v>_{DT} \left[E_\alpha \left(1 + \frac{E_R}{E_{FUS}}\right) f_{\alpha i} - E_R \right] V_c - \frac{n_c^2 V_c}{(n\tau)_c} (\phi_c + T_c)$$

$$+ \frac{n_c^2 V_c}{(n\tau)_{ei}} \cdot \frac{3}{2} (T_{ec} - T_c) + \left[I_{AUX}^{ion} E_{c,inj} + I_{AUX}^{cx} (E_{c,inj} - \frac{3}{2} T_c) \right.$$

$$+ I_{LEPB}^{ion} (V_{LEPB} + \phi_{LEPB} - \phi_e) + I_{LEPB}^{cx} (V_{LEPB} + \phi_{LEPB} - \phi_e - \frac{3}{2} T_c)$$

$$+ I_{MEPB}^{ion} (V_{MEPB} + \phi_{MEPB} - \phi_e) + I_{MEPB}^{cx} (V_{MEPB} + \phi_{MEPB} - \phi_e - \frac{3}{2} T_c)$$

$$+ I_{HEPB}^{ion} (V_{HEPB} + \phi_{HEPB} - \phi_e) + I_{HEPB}^{cx} (V_{HEPB} + \phi_{HEPB} - \phi_e - \frac{3}{2} T_c)$$

$$\left. - I_{GP} (\frac{3}{2} T_c) \right] \Big/ e = 0, \qquad (2\text{-}76)$$

where

$$E_R \approx 45.0 + \frac{3}{2} T_c \quad , \qquad (2\text{-}77)$$

$$(n\tau)_{ei} \approx \frac{2.50 \times 10^{13} \, T_{ec}^{3/2}}{\ln \Lambda_{ei}} \qquad (2\text{-}78)$$

and

$$\ln \Lambda_{ei} \approx \ln [2.65 \times 10^{13} \, T_{ec}/\sqrt{n_c}] \quad . \qquad (2\text{-}79)$$

The first term of Eq. (2-76) is the alpha heating of ions; E_R is the reactant energy, which is assumed to be distributed between the fusion neutron and fusion alpha in the same proportion as is the fusion energy. The second term is the Pastukhov energy loss out the ends. The third term is the energy transfer between ions and electrons. The fourth, sixth, eighth, and tenth terms are the energy gains due to ionization of the auxiliary fuel beam, LEPB,

MEPB, and HEPB, respectively. The fifth, seventh, ninth, and eleventh terms are the charge-exchange energy transfers between the auxiliary fuel beam, LEPB, MEPB, and HEPB, respectively. Finally, the twelfth term is the energy loss due to either ionization or charge exchange with the gas feed.

The central-cell (passing) electron particle balance, which determines ϕ_e, may be written as follows:

$$(I_{LEPB}^{ion} + I_{MEPB}^{ion} + I_{HEPB}^{ion} + I_{AUX}^{ion} + I_s)/e + \frac{n_p^2 (2V_p)}{(n\tau)_p} = \frac{n_c^2 V_c}{(n\tau)_{ec}} , \qquad (2\text{-}80)$$

where

$$(n\tau)_{ec} \approx 8.19 \times 10^9 \frac{g(R_{ce}/2)}{\ln \Lambda_{ee}} T_{ec}^{3/2} \left(\frac{\phi_e}{T_{ec}}\right) \exp\left(\frac{\phi_e}{T_{ec}}\right) , \qquad (2\text{-}81)$$

and

$$\ln \Lambda_{ee} \approx \ln (2.83 \times 10^{13} T_{ec}/\sqrt{n_c}) . \qquad (2\text{-}82)$$

The first four terms on the left-hand side of Eq. (2-80) are the electrons produced by ionization of the LEPB, MEPB, HEPB, and auxiliary fuel beam, respectively. The fifth term is an auxiliary current, I_s, of cold electrons that one may wish to inject into the central cell. The sixth term reflects the fact that every time a plug ion is lost out the end of the machine, a plug electron must become a passing electron in order to maintain quasi-neutrality in the plugs. The term on the right-hand side of Eq. (2-80) is the Pastukhov end loss of electrons.

The central-cell (passing) electron energy balance may be written as follows (note: potential energies in this equation are referenced to the central-cell potential, ϕ_e):

$$\frac{1}{4} n_c^2 <\sigma v>_{DT} \left[E_\alpha \left(1 + \frac{E_R}{E_{FUS}} \right) f_{\alpha e} \right] V_c + \frac{1}{e} I_s \phi_e$$

$$- \frac{n_c^2 V_c}{(n\tau)_{ec}} (\phi_e + T_{ec}) + \frac{n_p^2 (2V_p)}{(n\tau)_p} (\phi_b + T_{ep}) - \frac{n_c^2 V_c}{(n\tau)_{ei}} \cdot \frac{3}{2} (T_{ec} - T_c)$$

$$+ P_{cp}^* + P_{cp} = \frac{-1}{e} \left[I_{LEPB}^{ion} (\phi_b + \overline{E}_e{}_{LEPB}) \right.$$

$$+ I_{MEPB}^{ion} (\phi_e - \phi_{MEPB})$$

$$\left. + I_{HEPB}^{ion} (\phi_b) \right] \quad , \tag{2-83}$$

where

$$\overline{E}_e{}_{LEPB} \approx \phi_b + \phi_{LEPB} - \phi_e \quad , \tag{2-84}$$

$$P_{cp} \approx G_{ep} \frac{n_p^2}{(n\tau)_p^{ee}} (T_{ep} - T_{ec}) \exp \left(- \frac{\phi_c + \phi_b}{T_{ep}} \right) \quad (2V_p), \tag{2-85}$$

$$P_{cp}^* \approx \int_{z_{b0}}^{z_{pm}} G_{et} \frac{n_p^2}{(n\tau)_t^{ee}} (T_{ep} - T_{ec}) \exp \left(- \frac{\phi_e + \phi_c - \phi^*(z)}{T_{ep}} \right) 2 \cdot dV^* , \tag{2-86}$$

$$G_{ep} \approx G_{et} \approx 1 \quad , \tag{2-87}$$

$$(n\tau)_p^{ee} \approx 8.19 \times 10^9 \frac{T_{ep}^{3/2}}{\ln \Lambda_p^{ee}} \tag{2-88}$$

$$(n\tau)_t^{ee} = 8.19 \times 10^9 \ \frac{T_{ep}^{3/2}}{\ln \ \Lambda_t^{ee}} \quad ,$$

$$\ln \ \Lambda_p^{ee} = \ln \ (2.83 \times 10^{13} \ T_{ep} \ / \ \sqrt{n_p}) \quad , \tag{2-89a}$$

and

$$\ln \Lambda_t^{ee} = \ln \left\{ 2.83 \times 10^{13} \ T_{ep} \ / \ [n^*(z)]^{1/2} \right\} \quad . \tag{2-89b}$$

The first term on the left-hand side of Eq. (2-83) is the alpha heating of the passing electrons. The second term on the left is the gain due to the influx of cold auxiliary electrons [see fourth and fifth terms of Eq. (2-80)]. The third term on the left is the Pastukhov energy loss. The fourth term on the left is the energy gain each time a trapped electron becomes a passing electron. The fifth term on the left is the energy transfer between central-cell ions and electrons. The sixth and seventh terms on the left model the thermal energy transfer between the passing electrons and the trapped electrons in the transition region and plug, respectively.

The terms on the right-hand side of Eq. (2-83) are contributions to passing-electron energy due to the arrival of electrons in the LEPB, MEPB, and HEPB, respectively.

The final energy balance we present to complete the system of equations describing the barrier cell tandem mirror is the trapped electron energy balance:

$$P_{ECRH} + \frac{n_p^2(2v_p)}{(n\tau)_{drag}} (E_p - \frac{3}{2} T_{ep}) - \frac{n_p^2(2v_p)}{(n\tau)_p} (\phi_c + \phi_b + T_{ep})$$

$$= P_{cp}^* + P_{cp} + P_{synchrotron} + \frac{1}{e} I_{LEPB}^{ion} \left[(\phi_{LEPB} + \phi_b - \phi_e) + \overline{E}_{e\ LEPB} \right] . \quad (2\text{-}90)$$

The first term on the left-hand side of Eq. (2-90) is the ECRH power input, and the second term is the heating due to plug ion drag. The third term is the energy loss due to cooling by incoming neutral-beam electrons. The first two terms on the right-hand side are the energy losses to the passing elec-trons in the transition region and plug, respectively. The third term on the right is the loss of energy due to synchrotron radiation in the plugs and transition regions. The final term is the cooling effect of electrons that arrive with the LEPB.

    Finally, we take the fusion power to be given by

$$P_{fusion} = \frac{1}{4} n_c^2 <\sigma v>_{DT} E_{FUS} (\pi r_c^2 L_c) \quad , \qquad (2\text{-}91a)$$

and the neutron wall loading to be given by

$$\Gamma = (E_n/E_{FUS}) P_{fusion}/(2\pi r_{FW} L_c) \quad . \qquad (2\text{-}91b)$$

TMR SCALING WITH THERMAL BARRIERS

    At present, there are many pieces of the physics model described in the preceeding section, such as the plug-to-center-cell electron transfer power P_{cp}, the relationship between $\phi_c + \phi_b$, T_{ep}, T_{ec} and n_p, n_b, the precise barrier ion trapping rate J_{trap}, and the center-cell MHD beta limit, which are only crudely estimated and which are the subject of ongoing theoretical inves-tigation. Until uncertainties associated with these parts of the physics model are resolved by further work, a detailed point design for a TMR with

thermal barriers is unwarranted. However, at this time we have identified the essential physics and basic scaling laws for the thermal barrier concept, and so we can project trends in the various parameters that should lead us to the TMR goals set forth in the first section of this report: $Q \gtrsim 10$, $P_{net} \lesssim 500$ MWe, $L_c \lesssim 50$ m ($\Gamma \gtrsim 2$ MW/m^2), and $B_{cond} \lesssim 12$ T.

The most important and, at present, least known parameter is the center-cell beta limit β_c, which is determined by MHD stability considerations, ballooning in particular. The ballooning-mode beta limit for β_c will depend on plasma pressure profiles in the barrier (pumping), radial electric fields (rotation), and detailed magnet design (field-line lengths and curvatures). Radial electric fields may or may not exist, depending on whether radial electron transport rates compete with end loss. The first iteration magnet design described in Chapter 3, developed only with interchange as an MHD stability constraint, has been subsequently evaluated for ballooning by an MHD code[2-8] recently modified to treat geometries appropriate for tandem mirrors with thermal barriers. The resulting low beta limit ($\beta_c \lesssim 10\%$) for ballooning stability in the present thermal barrier TMR design, as compared to stable betas $\beta_c \approx 50\%$ found in previous tandem mirror design appears to be due in part to the rather long length of the present thermal barrier regions ($L_b \gtrsim 14$ m), which reduces field line-bending energy. Ongoing magnet design efforts seek to improve the center-cell beta by reducing the length of the thermal barrier.

Since the center-cell beta and the thermal barrier length L_b are important unresolved parameters, we characterize the TMR Q scaling in terms of these parameters in an approximate way as follows: assuming a sufficiently small barrier density $n_b \ll n_c$ makes the pump power dominate, we use Eq. (2-14) for Q. Integrating the ion-trapping current density Eq. (2-41) over the axial field profile of the barrier cell in the present magnet set,

and assuming that half of the pumping is achieved by charge exchange with appropriate neutral beams injected into the barrier as described in Chapter 5 (the other half of the trapped ion current is assumed to be lost radially by non-omnigeneous drift surfaces[2-6] we can estimate a pump-power (trapped) scaling as

$$P_{pump} \; 2V_b \approx k_b \; \frac{n_c^2}{T_{ic}^{3/2}} \; \left[\frac{\pi r_c^2 \; B_c \; (1 - \beta_c)^{1/2}}{B_{mb}} \right] L_b \; \phi_b (MW) \quad , \qquad (2\text{-}92)$$

where the proportionality constant $k_b \approx 3.6 \times 10^{-41} \; T_{ic}^{3/2}$ is a weak function of the axial field profile shape in the barrier, with the indicated temperature dependence valid in the range $20 < T_{ic} < 40$ keV. Here n_c is in m^{-3}, r_c and L_b in metres, T_{ic} and ϕ_b in keV. With this expression for $P_{pump} 2V_b$, and approximating $\phi_b \approx 3 \; T_{ic}$ (ϕ_b/T_{ic} varies only logarithmically), Eq. (2-14) for Q can be written as

$$Q \approx \frac{\frac{1}{4} n_c^2 \; \langle\sigma v\rangle_{DT} \; (17.6) \; (1.6 \times 10^{-19}) \; \pi r_c^2 \; L_c}{k_b \; \dfrac{n_c^2}{T_{ic}^{3/2}} \left[\dfrac{r_c^2 \; B_c \; (1 - \beta_c)^{1/2}}{B_{mb}} \right] L_b \; \phi_b}$$

$$Q \approx 6.5 \times 10^{21} \left(\frac{\langle\sigma v\rangle_{DT}}{T_{ic}} \right) \left[\frac{B_{mb}}{B_c \; (1 - \beta_c)^{1/2}} \right] \left(\frac{L_c}{L_b} \right) \quad . \qquad (2\text{-}93)$$

We note that $\langle\sigma v\rangle_{DT}/T_{ic}$ has a broad maximum around $T_{ic} \approx 30$ keV. We can take the maximum $B_{mb} \approx 12$ T, assuming the solenoidal barrier coil can have an efficiency approaching 100%. An economic neutron wall loading $\Gamma \approx 3$ MW/m^2 is achieved for a center-cell plasma radius $r_c \approx 1$ m and first-wall radius $r_w \approx 1.5$ m, accommodatable in the present magnet set, at a center-cell density $n_c \approx 1.4 \times 10^{20}$ m^{-3}. For this density, the required center-cell field scales as $B_c \approx 2.1/\sqrt{\beta_c}$ (tesla), assuming $T_{ec} = T_{ic}$, including alpha pressure.

With these assumptions, and taking $P_{fusion} \, V_c/[(P_{ECRH} + P_{NB}) \, 2V_p] \approx L_c$ (in m) to take into account the plug power, the overall Q reduces to roughly

$$Q \approx \left\{ \left[0.8 \left(\frac{\beta_c}{1 - \beta_c} \right)^{1/2} \frac{L_c}{L_b} \right]^{-1} + L_c^{-1} \right\}^{-1} \quad . \qquad (2\text{-}94)$$

Figure 2-2 shows a plot of Q versus L_b for several values of β_c and for a center-cell length $L_c = 50$ m, which gives a reactor power $P_{net} \approx 500$ MW(e). Longer L_c give proportionally more Q and P_{net}. We see from Fig. 2-2 that we need β_c in the range of 60 to 70% at barrier lengths of 5 to 6 metres in order to meet our reactor goals of Q = 10 at $L_c = 50$ m [500 MW(e)]. To achieve Q = 10 at lower β_c would require longer center-cell lengths and correspondingly more power.
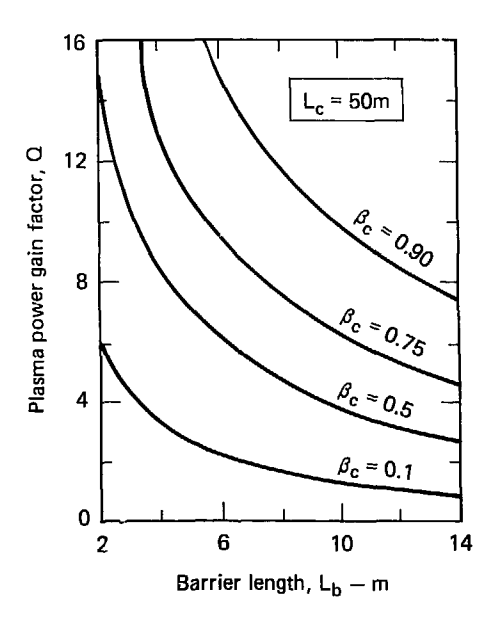

Fig. 2-2. Plasma gain factor, Q, with thermal barriers as a function of barrier length for center cell length $L_c = 50$ m.

60

If our present design approaches for adding thermal barriers to a TMR (as in Fig. 2-1) do not ultimately yield a satisfactory center-cell MHD beta limit for a small reactor, we can explore other magnet design options to improve the center-cell beta. One promising approach we are presently examining capitalizes on the fact that the shorter transition regions between center cell and yin-yang plugs in standard tandem mirrors without thermal barriers already have ballooning beta limits $\beta_c \approx 0.5$. The idea is to add thermal barriers between the yin-yang plugs and the A-cells of a previous TMR design,[2-4] as schematically shown in Fig. 2-3. The yin-yang plugs, operated at lower density, magnetic field, and beam power, would serve primarily as MHD anchors close to the center cell, where beta can then be high. The lower density A-cells, which previously served only to reduce the potential drop from the yin-yang plugs, would now be ECRH-heated to a potential greater than the yin-yang plugs, so that the A-cells have the primary function of electrostatic confinement of the center-cell ions. The required ECRH power to raise the A-cell potential would be small because of the thermal barriers added to the gaps between the yin-yang plugs and the A-cells. Since the functions of MHD anchor and electrostatic plug are now separated, the A-cell at low betas need not also be minimum-B, allowing flexibility in its magnet design. Pursuit of this promising candidate for a TMR with thermal barriers may result in improved performance through its greater flexibility as well as higher center-cell beta.
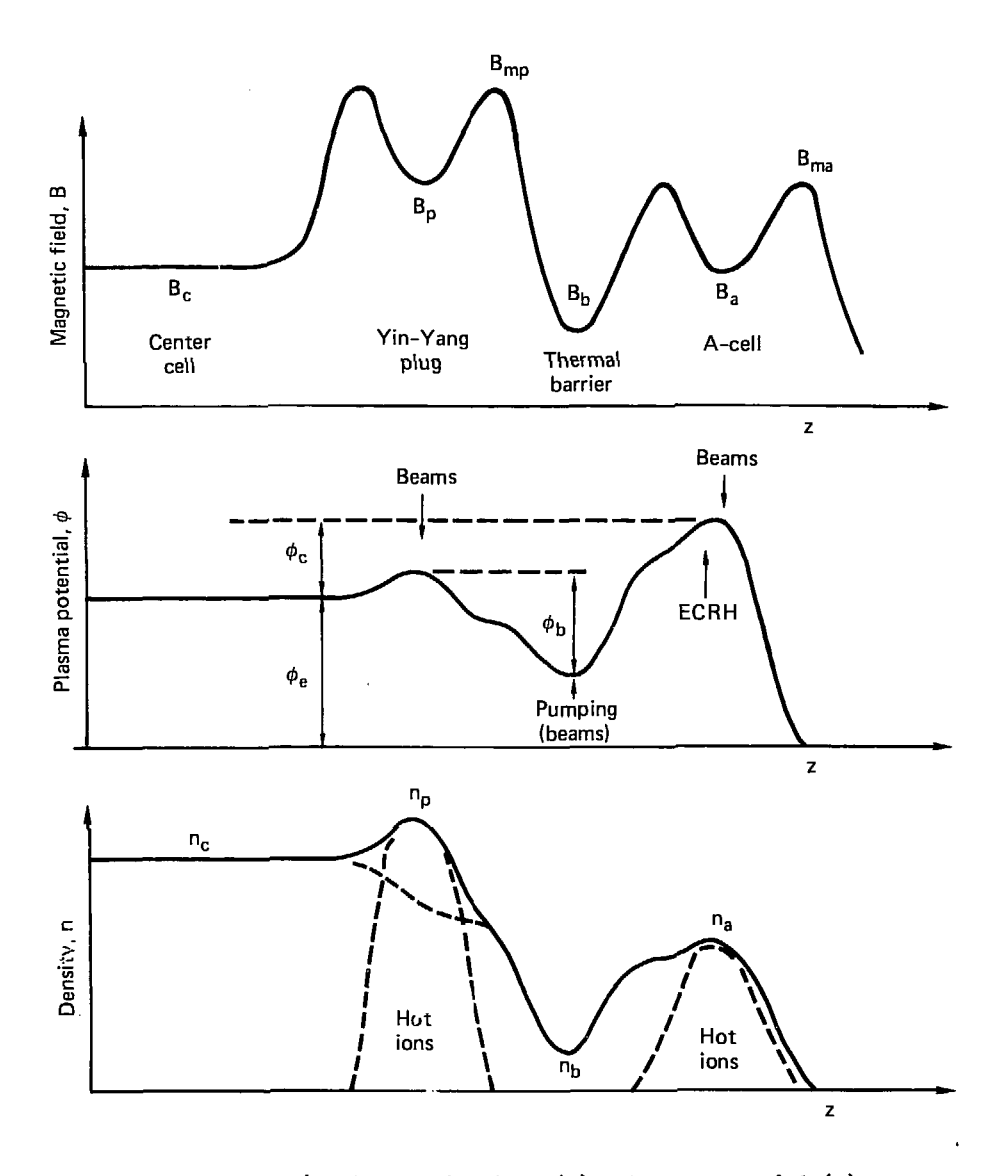
Fig. 2-3. Schematic of magnetic field (B), plasma potential (ϕ), and density (n) as functions of z for tandem mirror reactor with thermal barriers and A-cells.

REFERENCES

2-1.   R. W. Moir, W. L. Barr, G. A. Carlson, W. L. Dexter, J. N. Doggett,
        J. H. Fink, G. W. Hamilton, J. D. Lee, B. G. Logan, W. S. Neef, Jr.,
        M. A. Peterson, and M. E. Rensink, Preliminary Design Study of the
        Tandem Mirror Reactor, Lawrence Livermore Laboratory Rept. UCRL-52302
        (1977).

2-2.   B. G. Logan, W. L. Barr, D. J. Bender, G. A. Carlson, W. L. Dexter,
        J. N. Doggett, R. S. Devoto, J. F. Fink, T. K. Fowler, G. W. Hamilton,
        D. Lappa, J. D. Lee, W. D. Neef, Jr., A. A. Mirin, R. W. Moir,
        M. A. Peterson, and M. E. Rensink, in Proc. 7th Intern. Conf. on Plasma
        Physics and Cont. Fusion Research, Innsbruck, Austria, 1978 (IAEA, in
        press); also Lawrence Livermore Laboratory, Rept. UCRL-80644 (1978).

2-3.   J. F. Clauser, R. K. Goodman, and G. M. Melin, "Measurements of Axial
        Electron Temperature Profiles in 2XIIB," Bull. Am. Phys. Soc. 23, p. 775
        (1978).

2-4.   G. A. Carlson, B. M. Boghosian, J. H. Fink, J. O. Myall, and W. S. Neef,
        Jr., Parametric Studies of Tandem Mirror Reactors, Lawrence Livermore
        Laboratory, Rept. UCID-18158 (1979).

2-5.   D. E. Baldwin, B. G. Logan, and T. K. Fowler, An Improved Tandem Mirror
        Fusion Reactor, Lawrence Livermore Laboratory, Rept. UCID-18156 (1979).

2-6.   J. Kesner, Passive Generation of Ambipolar Potential Barriers in a
        Tandem Mirror, University of Wisconsin Report UWFDM-303 (May 1979).

2-7   D. L. Galbraith and T. Kammash, The Dynamic Behavior of a Mirror Fusion
        Reactor, EPRI. Rept. ER-521 (1978).

2-8.   T. B. Kaiser, "Numerical Investigation of the Ballooning Stability of
        TMX at Finite β," Bull. Am. Phys. Soc. 23, 754 (1978).

CHAPTER 3. MAGNETS

J. O. Myall

The arrangement of magnets that we studied for the tandem mirror reactor is shown in Figure 3-1. The components are:

- Central cell solenoid (actually a series of short solenoidal coils with gaps for blanket coolant pipes)

- Barrier solenoidal coil

- Inner transition "cee" coil

- Plug yin-yang coils

- Outer circularizing "cee" coil.

The total system is symmetric about the center except for a 90° rotation about the axis.

Central cell solenoid

Barrier coil
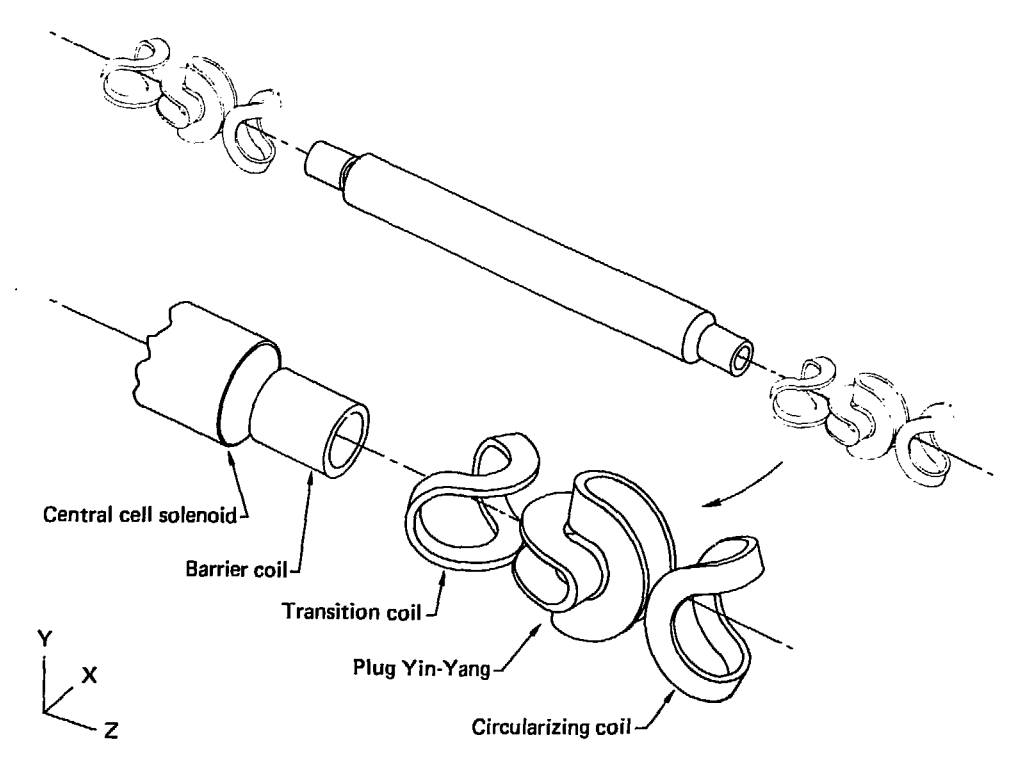
Transition coil

Plug Yin-Yang

Circularizing coil

Y
X
Z

Fig. 3-1. Arrangement of magnets.

The magnets have been designed by means of the EFFI computer code[3-1]. They give the magnetic field values indicated in Fig. 3-2, which shows the variation in field magnitude on the machine axis. The shape of the curve is characteristic of tandem mirrors incorporating thermal barriers; the absolute field magnitudes are those chosen for our particular design. The thermal barrier concept requires that the uniform field in the central cell rise sharply at both ends to a peak, in this case 12 T, followed by a minimum point at 10% of this value, i.e., 1.2 T. This magnetic field profile is provided by a high field solenoid and a gap separating it from the outer group of plug and transition coils. The length of the barrier cell between the 12-T peak and the inner mirror point of the plug is 14.3 m. The plug coils are required to give an axial mirror ratio of 1.5 and also a positive radial well. These requirements are satisfied by means of a yin-yang coil pair. The yin-yang distorts the plasma cross section into an elliptical shape. In consequence, we have provided transition cee coils on both sides of the yin-yang in order to restore circularity. A primary constraint to the coil design is the need for magnetohydrodynamic (MHD) stability. This system has been designed to achieve interchange stability (which significantly affected the design of the transition coils). The interchange stability calculation with the final transition coil yielded an upper limit of 1.38 for the central cell-to-plug β ratio.

The only coil with a high field requirement and hence a high conductor field (12.5 T) is the barrier solenoid. This is therefore the only coil for which niobium-tin superconductor is required. It is also the only coil for which structural requirements are here considered; the other coils should not present any difficulty in this regard.

In the following paragraphs, the several coils are discussed individually.

Distances from
center — m
31.4
37.25
45.75
48.2
50.65
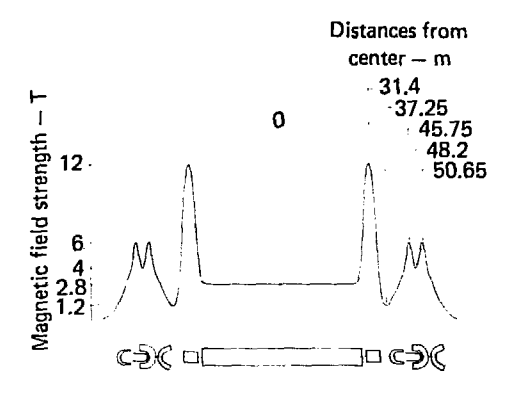
Fig. 3-2. Field magnitude |B| on machine axis.

CENTRAL CELL

Figure 3-1 shows the central cell magnet represented as a continuous solenoid 56 m in total length (actually it will have discrete short solenoids occupying about 30% of the total cylindrical surface—see the section on Central Cell Design, Chapter 8). The inside coil radius for this magnet model is 2.6 m, and the centerline field is 2.8 T.

BARRIER COIL

This coil is required to give a peak field of 12 T on its centerline. It is a solenoid having an inside radius of 1.3 m, a length of 4.5 m, a radial thickness of 0.46 m, and a current density of 24.3 MA/m^2. The conductor volume is 19.9 m^3. The inside radius accommodates approximately 0.7 m of shielding around the plasma. The length and thickness were chosen to give a high magnetic efficiency (96%) so that the peak field in the conductor is only 12.5 T. This efficiency is expensive in terms of conductor volume, but the conductor field is the controlling factor, being at the limit of current niobium-tin superconductor development with ordinary liquid helium coolant.

The conductor field is a maximum only at the inner radius—it falls off rapidly as the radius increases. Figure 3-3 shows a contour plot of the magnitude of the magnetic field $|B|$ for a section through the coil. The outer (radial) two-thirds of the section experiences fields of less than 8 T. Thus only the inner third of the coil requires niobium-tin superconductor. The coil would be built in two layers, with a supporting ring between them.
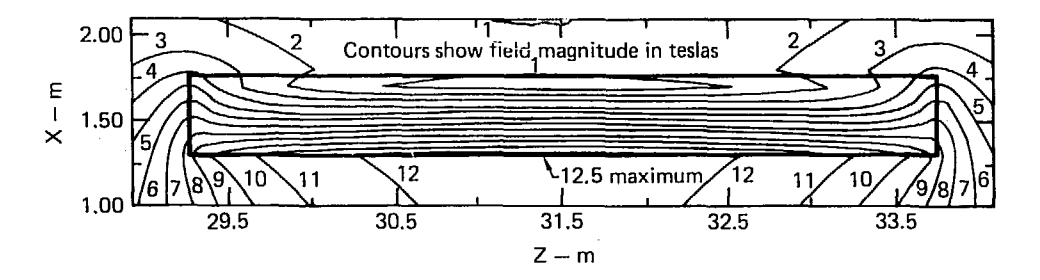
Fig. 3-3. Section through barrier coil showing contours of field magnitude $|B|$.

The upper curve in Fig. 3-4 shows the average radial force per unit of conductor volume plotted against the radius; it is approximately linear. If we ignore the hoop stress in the conductor and assume that the radial force is taken entirely by the supporting ring, the radial stress in the niobium-tin layer of the conductor is given by the lower curve. Figure 3-4 also shows the radial variation of the conductor field at the midplane of the coil. At a radius of approximately 1.45 m, the conductor field has decreased to 8 T. This radius defines the location of the supporting ring. The radial compressive stress at this point is approximately 32 MPa (4640 psi), which is an acceptable stress in the conductor. The niobium-tin superconductor will be in a matrix of copper. The strain in copper ($E = 117 \times 10^3$ MPa) at the above stress is only 0.027%. If we assume that the support ring is made of a steel with a working stress of about 100,000 psi at cryogenic temperature, its
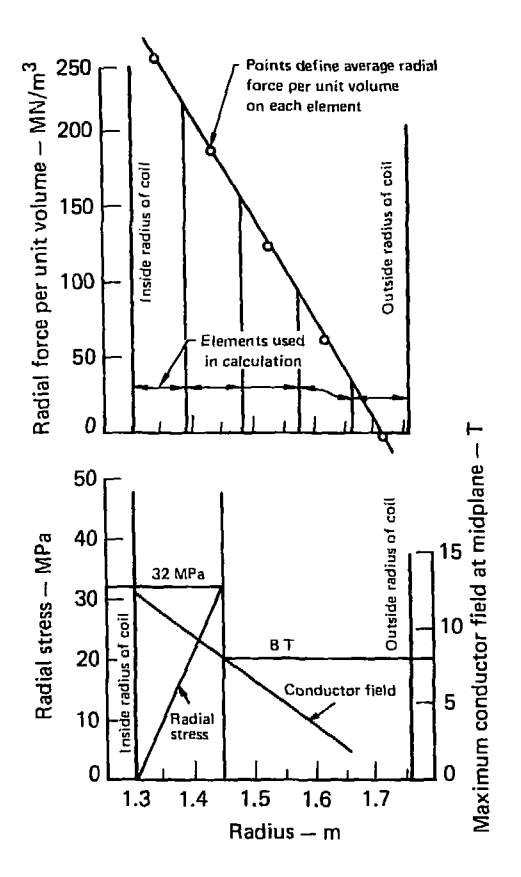
Fig. 3-4. Radial body force and stress in barrier coil.

thickness needs to be only ~0.07 m, and its tensile strain is ~0.33%. The same strain would occur in the superconductor. The combined strain in the superconductor is well within the limit for niobium-tin (~0.6% with no degradation in current carrying capacity [3-2]. If the hoop stress in the conductor were taken into account, the support ring could be significantly thinner.

Improved plasma performance would be obtained if the field in the barrier coil were even larger—this improved performance could be achieved by designing the niobium-tin superconductor to operate at lower temperature through the use of superfluid helium.

The plasma within the central cell and the barrier coil is of circular cross section. If this plasma were allowed to enter the plug yin-yang directly it would be distorted to an elongated (elliptical) shape. The transition coil elongates the plasma in the opposite (perpendicular) direction, thus opposing the subsequent effect of the yin-yang and enabling the plasma to return to an approximately circular section at the center of the latter. The distortion is illustrated in Fig. 3-5, in which vacuum field lines are shown plotted in two perpendicular planes (both of these field lines begin at a radius of 1 m at the center of the reactor).
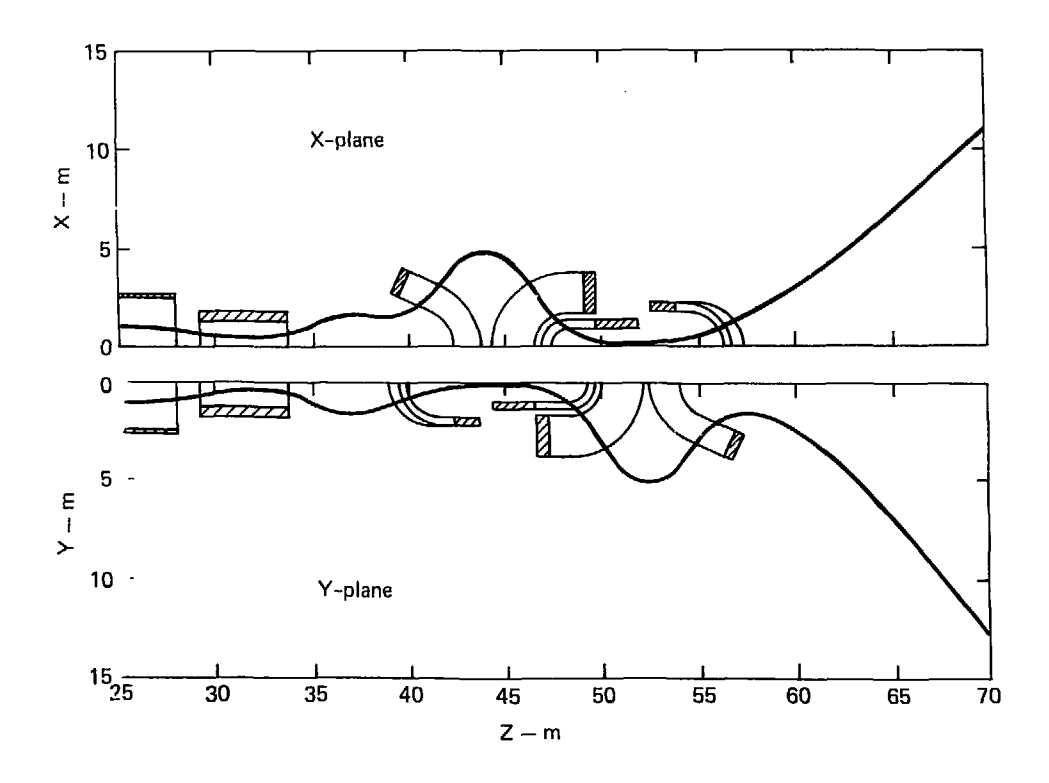
Fig. 3-5. Line plots through outer part of machine.

The field shaping requirement of the transistion coil can be achieved by four axial conductors, one in each quadrant, with adjacent quadrant currents in opposite directions; i.e., Ioffe bars. In practice, the axial currents can be provided by a cee coil. The minimum total current would result with a 180° cee coil; however, several additional factors affect the design of the coil. It must be close to the plug yin-yang and produce a significant axial field in order to keep the elliptical excursion of the flux bundle within reasonable limits (if the latter extends too far beyond the coils the ends of the ellipse spread into a dog-bone shape). On the other hand, the cee coil must not contribute more than a small proportion of the total field within the yin-yang; otherwise the latter will not develop its necessary magnetic well. These complications (and more) are quantified by the requirement for MHD interchange stability, in which if:

x, y = field line distances from axis,

$\ddot{x}, \ddot{y}$ = curvatures $\left(\dfrac{d^2 x}{ds^2} \text{ and } \dfrac{d^2 y}{ds^2} \right)$,

p = plasma pressure,

$|B|$ = magnitude of magnetic field;

then the integral:

$$\int \frac{p(x\ddot{x} + y\ddot{y})}{|B|} \, ds \quad ,$$

taken along a field line close to the machine axis and between the two outer mirror points is required to be ≥ 0. With reference to Fig. 3-5, the field line excursion that occurs in the xz plane between the transition and yin-yang coils has a small value of $|B|$, a large value of y, and a large negative curvature; the field line excursion therefore makes a major negative contribution

to the above integral. The magnitude of the negative effect is determined by the geometry of the transition coil. In our design, the major arc angle of the coil has been roughly optimized at 130°. The reduced angle necessitates a larger current (and a bulkier coil) in order to maintain the required quadrupole effect, but thereby increases the local axial component of the field sufficiently to produce the required stability.

The transition coil is separated from the barrier coil sufficiently to give a minimum field on centerline in the barrier region of 1.2 T.

Dimensions of the transition coil are:

Major arc mean radius, m	2.7
Minor arc mean radius, m	2.0
Cross section, m	1.4 × 0.4
Conductor volume (one coil),m^3	13.9
Angular length of major arc,$^\circ$	130
Current density, MA/m^2	22.4

Niobium-titanium superconductor will be used; the maximum conductor field is slightly over 6 T.

PLUG YIN-YANG COILS

The plug coils are specified to have an on-axis central field of 4 T and a mirror field of 6 T (hence, a vacuum mirror ratio of 1.5). They must also have a radial magnetic well to provide the "anchor" for MHD stability. This requirement led to the choice of a full 180° yin-yang.

Each half of the yin-yang consists of three layers of equal thickness; these are separated in the minor arc portion of the coils. The purpose of this separation is to reduce the average current density and thereby the magnitude of the field within the conductor (the maximum normally occurs on the

inside of the minor arc). For the same reason, the conductor section is relatively deep and narrow. A maximum conductor field of 9.0 T was calculated, giving a magnetic efficiency of 66%. Contours of $|B|$ are shown in Fig. 3-6 for a section of the yin-yang in the yz plane. Further refinement of the design (by using still deeper and narrower sections and/or more spreading of the conductor in the minor arc) should permit the reduction of the maximum conductor field to the specified 8 T. Niobium-titanium superconductor will be used. The following are the dimensions of the coils:

Mean radius of major arc, m	2.7
Mean radii of minor arcs, m	1.06, 1.18, and 1.30
Depth of conductor section, m	2.1
Thickness of each of 3 layers of conductor section, m	0.12.
Conductor volume (yin-yang pair), m^3	40.9

The center and outer layers have short straight sections between the major and minor arcs in order to give the required 0.04-m separation between layers. These dimensions permit a minimum shielding thickness around the plasma of approximately 0.8 m at the corner of the section.

The current density is 22.8 MA/m^2 for each half of the yin-yang. Figure 3-7, a transverse section at the center of the plug, illustrates the magnitude of the radial magnetic well.

CIRCULARIZING COIL

This coil performs a function similar to that of the transition coil. The circularizing coil converts the elliptical magnetic flux bundle leaving the plug to an approximately circular cross section, thus facilitating the
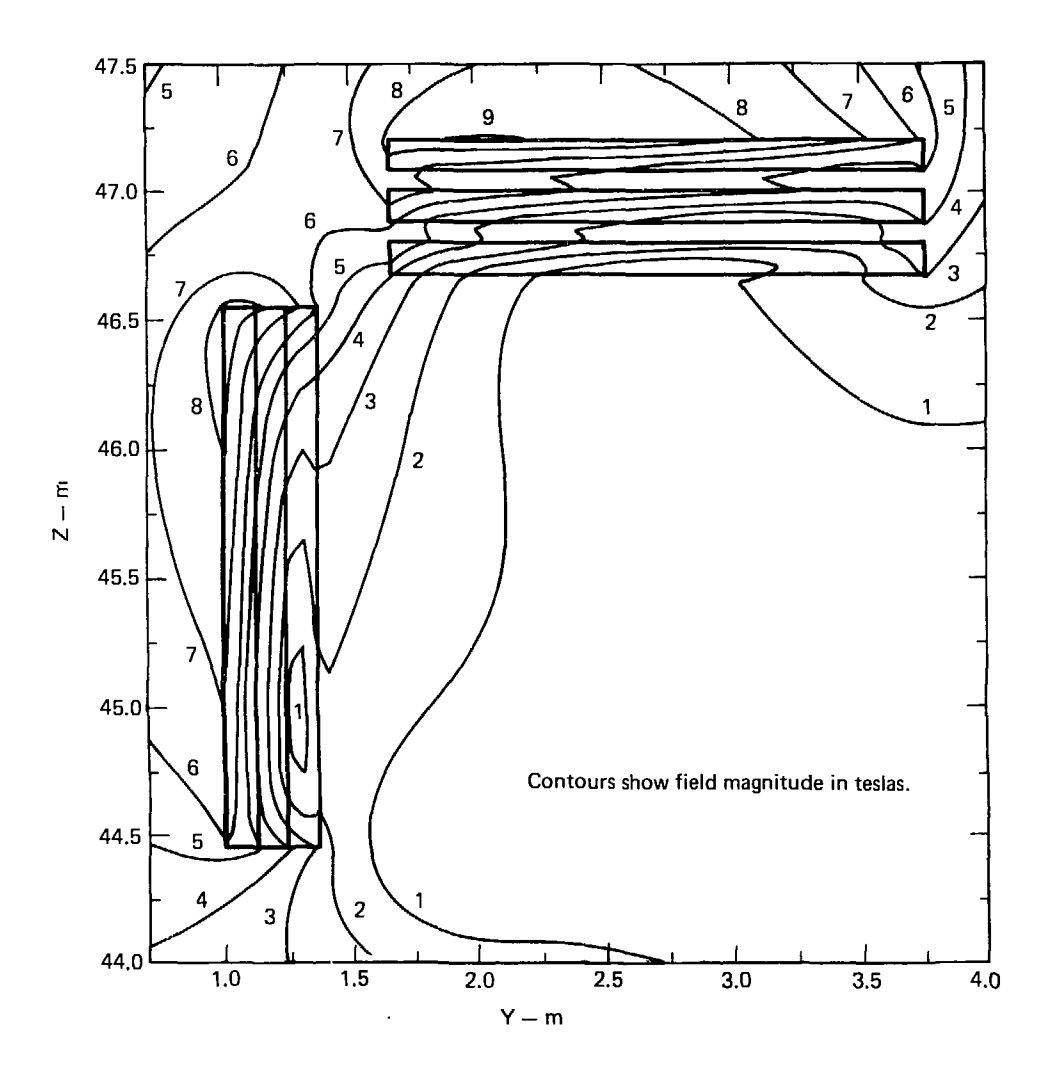
Contours show field magnitude in teslas.

Fig. 3-6. Section through plug yin-yang coils showing contours of field magnitude $|B|$.

76
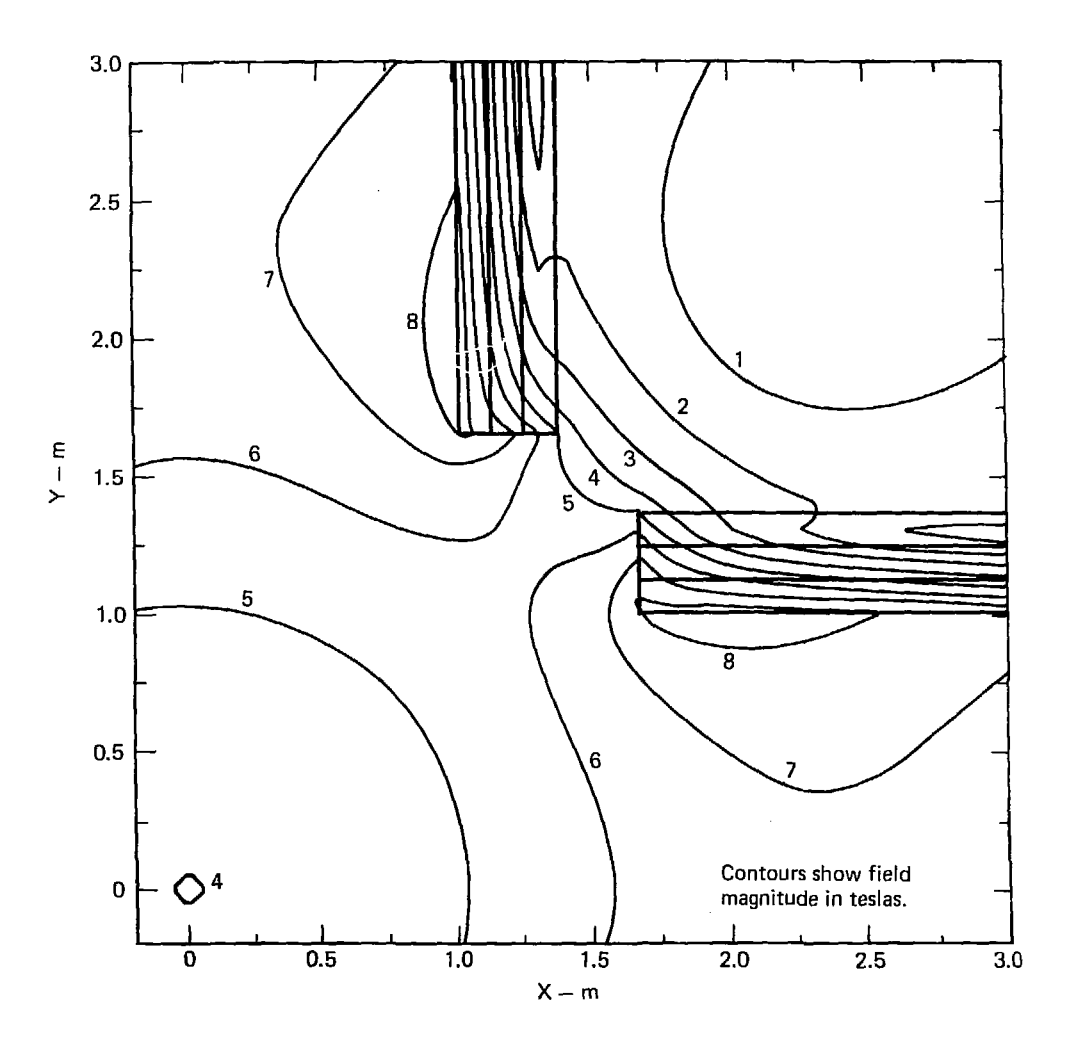
Fig. 3-7. Transverse section through center of plug (Z = 48.2 m) showing contours of field magnitude, and illustrating radial well.

design of the plasma direct converter. For calculational convenience the coil has been made identical to the transition coil (only the orientation is different). Making the coil identical is not strictly necessary, however, since the stability criterion does not involve the circularizing coil. A full 180° major arc cee coil would be equally effective and would have a smaller conductor volume.

The following are the dimensions of the circularizing coil:

Mean radius of major arc, m	2.7
Mean radius of minor arc, m	2.0
Conductor cross section, m	1.4 × 0.4
Conductor volume (one coil), m^3	13.9
Angular length of arc, °	130
Current density, MA/m^2	22.4
Superconductor material	Niobium-titanium

ALTERNATIVE REACTOR DESIGN WITH SOLENOIDAL PLUG COILS

For comparison purposes, a magnet set has been designed in which the plug is not required to have a radial well. (In this more speculative design the "anchor" for MHD stability must be provided by some other means, such as a hot electron ring in the plug, i.e., an EBT cell; we have not yet quantified the stability requirement in such a case.) This alternative design permits the plug coils to be merely a pair of short solenoids giving the required axial mirror ratio. There is no elliptic distortion of the plasma and therefore no need for either the transition or circularizing coils. The result is a considerable reduction in the length of the reactor, and in the volume (and hence cost) of the conductor. The overall length of the plug and barrier coil set is reduced from 28 to 16.3 m. The length of the barrier

region (from the barrier peak field to the first plug mirror) is reduced from 14.3 to 9.3 m. This reduction would considerably improve the reactor performance because the barrier "pump" beam power is proportional to the volume of the barrier region. The conductor volume for the plug coils is reduced from 40.9 m^3 for a yin-yang pair to only 14.3 m^3 for a solenoidal pair. The conductor volume reduction is even more dramatic because the alternative design has no transition or circularizing coil—a combined volume of 27.8 m^3. Thus, the total reduction is from 68.7 to 14.3 m^3, a factor of almost 5. The peak conductor field goes from 9.0 to 7.9 T. The following are the actual dimensions of the two plug solenoids: inside radius, 1.5 m; radial thickness, 0.34 m; length, 2.0 m; current densities, 24.6 and 25.0 MA/m^2. Figure 3-8 shows the magnitude of the magnetic field plotted along the axis of the machine (this figure should be compared with the corresponding Fig. 3-2 for the normal design).
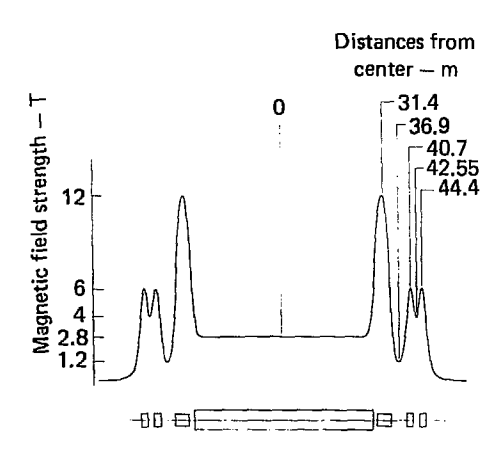
Fig. 3-8. Field magnitude $|B|$ on machine axis for tandem mirror reactor with solenoidal plug coils.

REFERENCES

3-1. S. J. Sackett, EFFI—A Code for Calculating the Electromagnetic Field,
      Force and Inductance in Coil Systems of Arbitrary Geometry, Lawrence
      Livermore Laboratory, Livermore, CA, UCRL-52402 (1978).

3-2. D. W. Deis, D. N. Cornish, A. R. Rosdahl, and D. G. Hirzel, Mechanical
      Strain of Large, Multifilament Nb_3Sn Conductors for Fusion Magnets,
      Lawrence Livermore Laboratory, Livermore, CA, UCRL-78890 (1977).

CHAPTER 4. END-PLUG NEUTRAL BEAMS

G. W. Hamilton, J. L. Erickson, J. H. Fink

Neutral beam requirements for the end plugs of a Tandem Mirror Reactor (TMR)[4-1] have been greatly reduced by the increased plug electron temperature made possible by thermal barriers and by electron cyclotron resonance heating (ECRH). In this version neutral beams in the end plugs are required only to maintain the density of fast H^+, for which the loss rate is low because of the reduction of electron drag. The neutral-beam requirement for each plug of the TMR is now only 0.25 MW of 400-keV H^0 trapped in the plasma.

Several changes in viewpoint are possible because of the reduced requirements. One change is the fact that it is not essential to have a high trapping fraction of the injected neutrals to have a favorable power balance, making it possible to reduce the density and size of the plasmas in the end plugs, with resulting economies in the magnets and structure. Another change is the fact that the neutral-beam design can be conducted with only a few extrapolations beyond existing technology. It is possible to be rather specific about the technical developments required for such a system to become operational.

As part of an operating system, the injectors must be compact, operate at better than 50% efficiency, and require scheduled maintenance shutdown not more than once a year. These injectors are estimated to cost about $1.00/W, injected[4-2].

While such injectors seem advanced with respect to today's low duty cycle, short pulse, 120-keV beams[4-3], their development is consistent with today's beam programs. Our need for beams of longer pulse length—about 1.5 s in the Tokamak Fusion Test Reactor (TFTR) or 30 s in the Magnetic Fusion Test Facility (MFTF)—and for beams delivering higher energy will lead to progress

that should make the TMR injector an acceptable engineering goal within the next decade.

In the process of designing such units, some of the problems encountered involve more than filling in "engineering details." They call for good judgment when available data are inadequate. In some cases ingenious inventions are needed to meet the specific requirements of the support structure, or perhaps the beam alignment, heat transfer, circuitry, continuous pumping, radiation hardening, magnetic shielding, safety, etc. We believe that engineers can be relied upon to provide satisfactory answers to such questions. However, before the design of the TMR neutral-beam injector can be started, the feasibility of the overall design objectives must be demonstrated.

Fortunately, these developments are either an outgrowth of the positive ion program or are related to it. Thus the initial development efforts to demonstrate feasibility need not be very expensive, nor need they radically alter present beam programs. However, subsequent efforts, such as TFTR upgrade or MFTF-B, that utilize these concepts will incur large costs and some engineering risk. Getting the first injector operational may require as much as $3/W.

Figure 1-5 is an overall view of the 400-keV injector assembly we will describe to show how the TMR injection requirements may be met. Figure 4-1 is a schematic of the injector. The injector consists of a low-energy source of H^- ions, a 400-kV acceleration column, a vapor stripping cell to convert the H^- ions to H^0, a charged beam disposal section, and the systems required for high-voltage power and protective circuits, voltage insulation, gas pumping, and radiation protection. Each of these components will be discussed in the following sections.
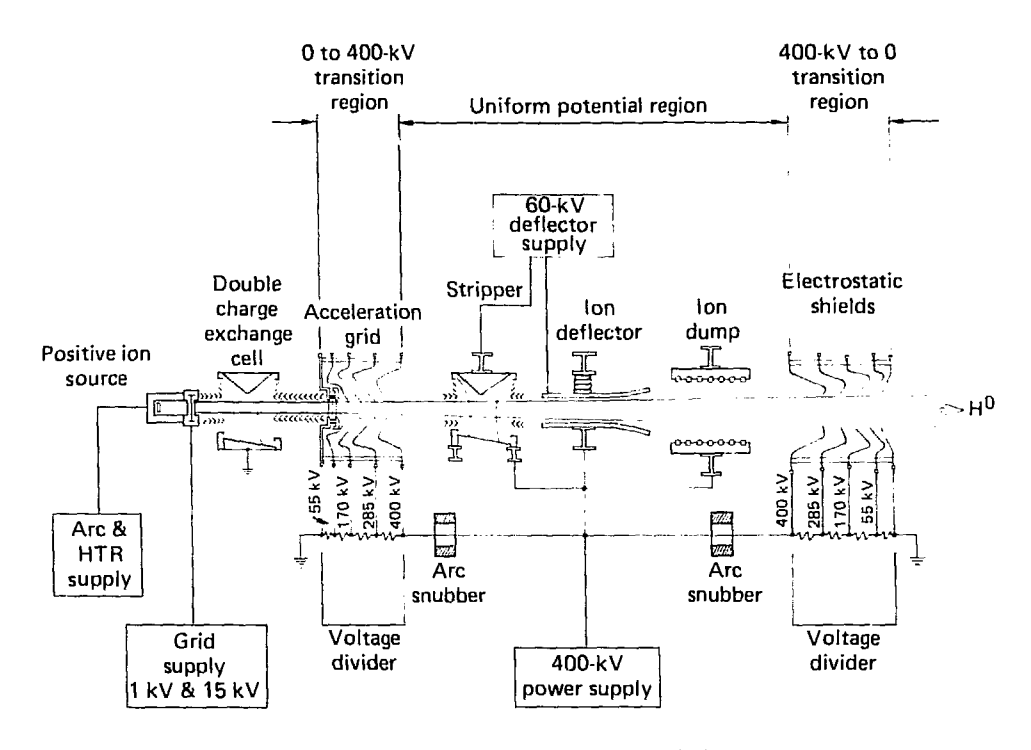
Fig. 4-1. Components of 400-keV injector.

NEUTRAL-BEAM SPECIFICATIONS

The specifications for the neutral-beam system are determined by the basic requirement for 0.25 MW trapped in each end-plug plasma at 400 keV. We have chosen H^0 rather than D^0 or T^0 for this system to reduce the gyro-radius and thereby to improve the DCLC plasma stability criterion. This choice is also convenient to reduce the neutron radiation from the end-plug plasma. The neutralization efficiency for negative ions is independent of the choice of isotope.

Table 4-1 indicates the specifications of the components of the 400-keV neutral-beam system calculated from the TMR requirements, for a design using negative ions produced by double-charge-exchange and neutralized by a vapor stripping cell optimized for maximum H^0 output. No attempt is made for electrostatic direct energy conversion of the residual charged beams. Thermal energy recovery of the 1.9 MW deposited on beam dumps is a possibility.

We have considered other options for each component of the injection system. These considerations will be discussed in the following sections.

ION SOURCE

The fundamental component of a neutral-beam injector is the ion source. If an injector is to be efficient and reliable, and to operate continuously for at least one year, its ion source must be capable of such performance. To adapt today's positive ion sources to meet the goals of the future, considerable development is required. Progress must be made to ensure extended cathode life, to provide grid cooling, and to form beams that are 80 or 90% atomic ions.

To achieve operating efficiencies of 50% or better with hydrogen at energies in excess of 75 keV or deuterium at energies greater than 150 keV, the neutrals must be formed from high-energy negative ions instead of from positive ions as is the current practice. This is because the charge-exchange cross section of negative ions is large and relatively independent of the beam energy. At present there are several types of negative ion sources under development.

TABLE 4-1. Neutral-beam performance specifications.

Item	Efficiency	Voltage (keV)	Current (A)	Power (MW)
H^0 trapped in plasma, each plug	--	400	0.625	0.25
Trapping fraction $= n_p \overline{L\sigma_T v}/v_B$	0.195			
H^0 injected into plasma	--	400	3.205	1.282
Neutralizer efficiency (optimized metal vapor stripping cell)	0.60			
H^- beam from accelerator	--	400	5.342	2.137
Power loss in accelerator	--	400	0.33	0.132
Power loss in voltage divider	--	400	0.10	0.040
Transparency of electron suppressor before acceleration	0.80			
H^- beam produced	--	1	7.09	0.007
Double charge exchange conversion efficiencies--				
from 1-keV H^+	0.20 (net after electron detachment in gas between Cs vapor and accelerator)			
from H_2^+ and H_3^+	0 (assuming no dissociation of low-energy molecular ions)			
Composition of 1-keV beam--				
H_1^+	0.80			
H_2^+ and H_3^+	0.20			
1-keV positive beam	--	1	44.3	0.044
Extractor grid transparency	0.5			
Ion source current density	0.25 A/cm^2 at plasma			
Area of extraction grids $= 44.3/(0.5 \times 0.25) = 354$ cm$^2 = 7 \times 50$ cm				

TABLE 4-1. (cont.)

Item	Efficiency	Voltage (keV)	Current (A)	Power (MW)
Beam dumps required				
(1) 1-keV H^0, after double charge exchange cell		1	37.2	0.037
(2) 1-keV H^-, intercepted by electron suppression grids		1	1.42	0.001
(3) 400-keV H^+ and H^-, after optimized stripping cell		400	2.137	0.855 .
(4) 400-keV H^0 after passing through plasma		400	2.580	1.032
Total beam dumps			41.052	1.926
Power requirements without thermal energy recovery				
400-kV accelerator (if 100% efficient)		400	5.77 .	2.31
1-keV ion source extractor		1	44.3	0.044
Other power requirements (arc, filament, vapor cells)			44.3	0.089
2 kW/A			44.3	0.089
Total power requirements				2.443

Injector efficiency (not including thermal recovery) = 1.282/2.443 = 0.525

Thermal energy recovery from beam dumps—

1.926 MWt × 30% = 0.58 MWe

Net power requirement = 2.443 − 0.58 = 1.87 MWe

One approach to source design produces negatives from positives by means of a metal-vapor double-charge-exchange cell. Approximately 20% of an incoming positive ion beam at 1 keV becomes negative in a cesium vapor cell of proper design. The remaining 80% of the beam leaves the cell as unwanted low-energy neutrals. To make this process functional a positive ion source is needed that can continuously deliver 1-keV ions that are 80 or 90% atomic. This requirement is very similar to that of the ongoing positive ion program. However, in this case the desired beam energy is much lower. As a consequence, the ion source needed for the double-charge-exchange method of forming negative ions will be a by-product of the present neutral-beam program.

A second approach to negative ion source design uses direct extraction of H^- produced in a plasma by bombardment of surfaces with low work function. A transverse magnetic field is required to separate the extracted H^- from the plasma electrons. Both approaches have assets and liabilities; we are choosing the double-charge-exchange approach for the TMR design study because the requirements are straightforward and because we expect a somewhat higher attainable current density per unit length of a long module.

Figure 4-2 is a drawing of our concept of a continuously operating source of 1-keV atomic hydrogen ions (H_1^+). We show a large-area longlife cathode, which could be made of lanthanum hexaboride, supporting 10 A/cm^2 of thermionic electron emission. The walls of the arc chamber are covered with magnets to form magnetic cusps called a picket fence. This configuration reduces the rate of ion recombination at the walls and thereby increases the yield of atomic ions.

The extracted low-energy beam current is 0.87 A per linear centimetre of a long plasma source. This current requires about 87 A of thermionic emission per centimetre—that can be provided by 9 cm^2 of emission surface per linear centimetre.
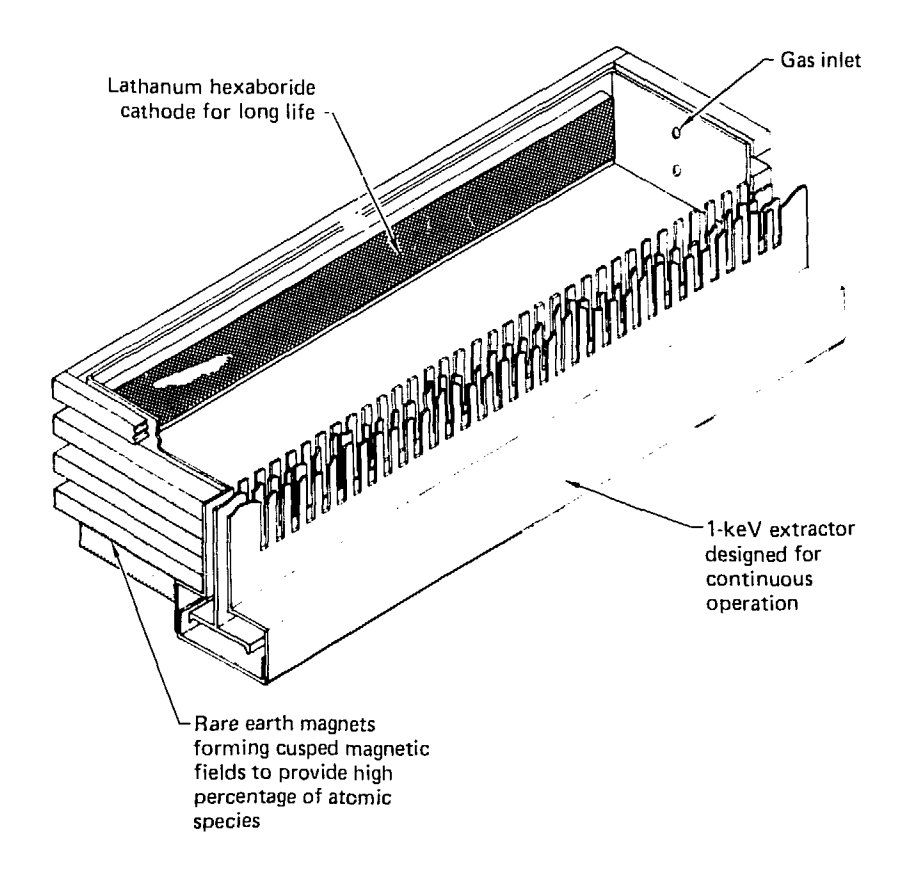
Fig. 4-2. Low-energy H^+ ion source for H^- production by double-charge-exchange.

To provide continuous operation, a 1-keV extractor grid is required to remove the energy dissipation resulting from ion bombardment of the grid rods. A proposed extractor[4-4] has been studied using conduction-cooled grid rods. This extractor is capable of dissipating a power loading of 40 W/cm^2 — adequate for the purpose.

Experiments now being performed at Lawrence Berkeley Laboratory[4-5] and in the Soviet Union[4-6] are producing negative ions by passing a positive ion beam through a plume of sodium vapor. The plume is produced in a cell that confines the metal vapor while allowing the beam to pass.

Of the several types of nozzles that could be considered for producing the plume, we have chosen a plug-type nozzle.[4-7] As shown in Fig. 4-3, the vapor is collected in manifolds on both sides of the nozzle. The vapor undergoes a Prandtl-Meyer expansion around the edge of a slit with the free-jet direction limited by the background pressure in the cell. The boundary layer flow along the nozzle surface is trapped between two well-directed jets, thus eliminating any significant loss of material.
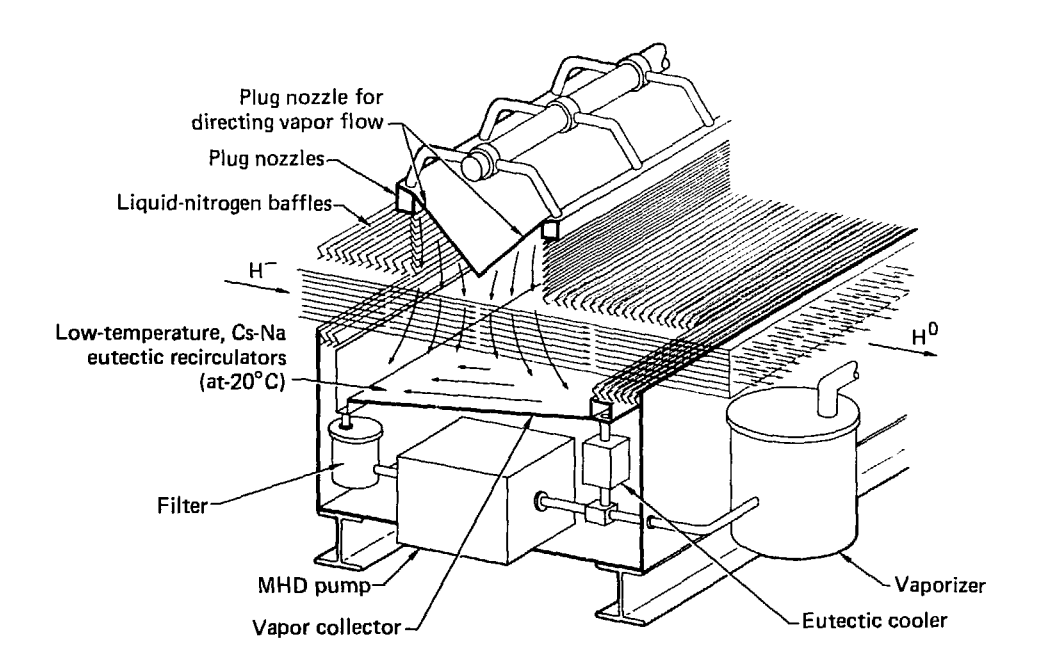
Fig. 4-3. Double-charge-exchange cell using cesium-sodium eutectic.

The alkali metals are all capable of performing as double-charge-exchange targets for the positive beam. Present experiments most often use sodium, but passing a 1-keV positive through cesium or rubidium vapor produces a higher equilibrium fraction (21%).[4-8] However, since the beam is at only 1 keV, it is more difficult to focus than the 7-keV beam that produces the maximum equilibrium fraction in sodium (12%). We have chosen cesium as the material for this double-charge-exchange cell.

When the beam enters the cesium plume it is assumed to be 80% H^+ and 20% H_2^+ and H_3^+. As the hydrogen ions collide with cesium atoms they capture an electron to become neutral, or capture two electrons to become negative. The cross sections for these two processes are designated σ_{10} and σ_{1-1}, respectively. Some of the neutral hydrogen atoms so formed can become positives (σ_{01}) or negatives (σ_{0-1}) by further collisions. Eventually, the beam will reach an equilibrium state in which the charge-exchange processes are balanced. We assume that the H_2^+ and H_3^+ are not dissociated at this low energy and do not contribute to the H^- production.

The thickness, π, of the vapor plume is its density, n, times the beam path length, ℓ. The fractions of positive, neutral, or negative hydrogen atoms (F^+, F^0, F^-) at any given point along the path length are determined by the cross sections for the various atomic processes between 1-keV hydrogen and thermal cesium. A series of differential equations characterizes the situation:

$$dF^+/d\pi = -(\sigma_{10} + \sigma_{1-1})F^+ + \sigma_{01} F^0 + \sigma_{-11} F^-$$

$$dF^0/d\pi = \sigma_{10} F^+ - (\sigma_{01} + \sigma_{0-1}) F^0 + \sigma_{-10} F^-$$

$$dF^-/d\pi = \sigma_{1-1} F^+ + \sigma_{0-1} F^0 - (\sigma_{-11} + \sigma_{-10}) F^- \tag{4-1}$$

The solution[4-9] of these equations results in Fig. 4-4. The maximum conversion from H^+ to H^- occurs at a plume thickness, π, of greater than 2×10^{15} atoms/cm^2. This is the design thickness for the double-charge-exchange cell.
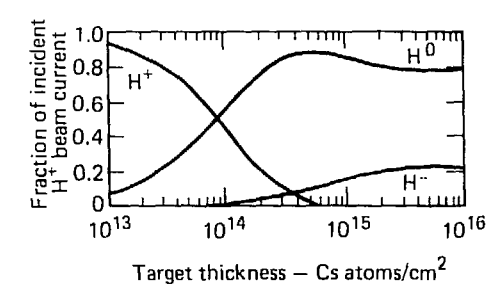
Fig. 4-4. Beam composition in cesium double-charge-exchange cell.

Molecular ions (H_2^+, H_3^+) entering the double-charge-exchange cell are a potential problem. At 1 keV, the optics of the ion beam are tenuous at best. If 1-keV molecular ions dissociate in the cesium to become half or third energy components, the situation worsens. One current goal of the Lawrence Berkeley Laboratory source development program is to produce a positive ion beam that is 90% atomic. With this goal achieved, the beam can be transported efficiently through the cell.

The utmost concern when using a metal vapor cell in a high-voltage beam line is that all vapor be confined to the cell. The minutest coating of cesium on an insulator or an electrode will enhance field emission characteristics or provide enough of a conducting path to encourage breakdown. An additional concern is that cesium would become a contaminant in the reactor plasma.

Several features of the cell design serve to eliminate metal vapor loss. They include a flowing eutectic collector at $-20^{\circ}C$, the plug nozzle design, and the venetian blind collectors surrounding the cell apertures. By taking these precautions, we limit the cesium flux from the cell to less than

10^{11} atoms/cm^2/s. The loss of cesium during periodic shutdowns is pre-
vented by shutter valves at each aperture. The valves guard against cesium
loss both during routine maintenance and in the event of a sudden reactor
shutdown.

The key to cesium vapor control is the liquid collector. The normal
melting point of cesium is 28°C. By forming a eutectic with sodium (see
Fig. 4-5), the cesium can be contained as a liquid at as low as -29°C.[4-10]
Therefore, all collection of vapor once it has crossed the beamline can be
made as a liquid at -20°C rather than above the normal cesium melting
point. Use of the eutectic results in a drop in vapor pressure of more than
2 orders of magnitude. Cesium could be collected as a solid at even lower
temperatures with lower vapor pressures, but the problem of recirculating this
solid cesium without heating and melting the surface is not a trivial one.

Fig. 4-5. Melting point depression
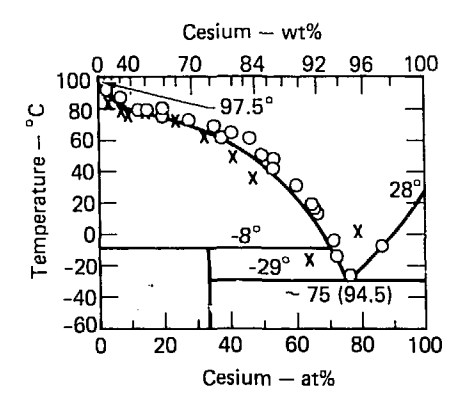for cesium-sodium eutectic.

The vapor pressure of cesium is much higher than that of sodium. Thus
when we boil the eutectic to produce the vapor plume, the plume is predomi-
nantly (99%) cesium and performs the double-charge-exchange function as
cesium. The potential for losing enough cesium to disrupt the viscosity of
the flowing collector is very low. First, the quantity of cesium lost from

94

the recirculating volume is very small due to the precautions discussed above. Second, at -20°C (the operating point for the collector), the atomic percentage of cesium can vary from 73 to 81% without the eutectic solidifying. For these reasons, careful monitoring of the makeup in the eutectic will not be necessary. We propose an 80% (atomic percent) cesium—20% sodium eutectic mixture for the double-charge-exchange cell. But since the vapor plume remains 99% cesium, the cell will produce a 20% double-charge-exchange efficiency for the 1-keV H^+ beam.

All cesium-sodium eutectic is continuously recycled to permit extended beamline operation. As the flow leaves the collector it is filtered to remove cesium or sodium hydrides, which may tend to form a solid residue. The material can be further purified before it is sent to a holding manifold. From here, it is pumped to the collector or to the boiler.

There is a secondary beneficial characteristic of having a metal vapor plume crossing the beamline. The plume acts as a gas curtain that prevents background hydrogen from diffusing through it. In theory and based on data from the Soviet Union,[4-11] this effect can produce an order-of-magnitude pressure drop across the double-charge-exchange cell. This pressure drop enables us to pump the large quantity of gas escaping from the source at a higher pressure, and reduces the flow of gas into the accelerator region.

A current of I^+ A enters the double-charge-exchange cell. When it leaves as a 20% negative beam, it has collected 1.2 I^+ A of electrons. This electron flow must be provided for in the overall beamline circuit. However, on a local scale, it must come from the cesium vapor plume. As this electron flow takes place, a positive plasma is formed in the plume that expands in all directions until the electron debt is equalized. Work at Lawrence Berkeley Laboratory is determining the consequences of this plasma formation with respect to metal vapor confinement. It may be necessary to provide a source of

electrons (an emitter) in the cesium plume prior to the point at which it crosses the beamline. With this source of electrons, the plasma formation and therefore its growth out of the plume will be limited.

The nozzle design and the characteristics of the plume as it undergoes an isentropic expansion are described elsewhere.[4-12] The mass of cesium flowing across the beamline is determined from the relation $Q_{MV} = n\ell wv$, in which n = density, ℓ = length of plume along the beamline, and v = velocity. For this cell with width, w = 110 cm, the vapor flow is 1.3 g/s.

The mass flow is used to determine the power required to operate the double-charge-exchange cell. The majority of the eutectic is maintained at $-20^{\circ}C$ with constant refrigeration losses due to conduction and the energy of the incoming vapor plume on the collector. Vapor in the plume must be heated from -20 to $425^{\circ}C$. Also, the manifolds, slits, and nozzle surfaces must be maintained at $425^{\circ}C$ to guarantee the proper flow characteristics. Circulating the eutectic involves a pump load, and the liquid nitrogen-cooled venetian-blind collector vanes add to the power required by the cell. An estimate for this total is 30 kW. Neutral-beam power requirements are often expressed as electrical input power divided by injected neutral-beam power. This double-charge-exchange cell has a power need (as defined above) of 0.023 We/W.

400-kV ACCELERATION COLUMN

The 400-kV H^- acceleration column will be similar to the 1.2-MV Pierce-type acceleration column previously described.[4-13] The potential along the beamline will vary according to the planar Child's Law; i.e.,

$$j = (4/9) \; \varepsilon_0 (2q/m)^{1/2} \; V(x)^{3/2}/x^2$$

$$= 5.46 \times 10^{-8} \; V(x)^{3/2}/x^2 \text{ for } H^- \quad , \tag{4-2}$$

in units of A, V, and cm. The current density is $j = 5.34 \text{ A}/(7 \times 50) \text{ cm}^2$ = 0.016 A/cm^2; therefore, the length of the acceleration column is 30 cm.

As shown in Fig. 4-6, the acceleration column will be divided into four stages by three intermediate electrodes at positions x = 7.5, 15.0, and 22.5 cm. The required voltages relative to the H^+ ion source at these points are 55, 170, and 285 kV; these voltages will be supplied by a voltage divider feeding the intermediate electrodes. The maximum electric field required is only 17 kV/cm.

It is necessary to prevent the electrons in the background plasma from entering the 400-kV acceleration column. The most straightforward technique for electron suppression is the immersion of two or more grids in the low-energy beam, biased to repel thermal electrons produced by ionization of background gas and cesium vapor. Electron suppression by immersed grids has been tested by a series of direct conversion experiments at Lawrence Livermore Laboratory and at Fontenay-aux-Roses.[4-14] Radiation-cooled grids immersed in the low-energy beam have been proven effective for suppressing plasma electrons if the beam power density is not greater than the limitation established by thermionic emission from the negative grid wires (100 to 200 W/cm^2).

Figure 4-7 shows a grid assembly at the entrance of the 400-kV acceleration column. The assembly consists of three sets of aligned grids of 80% transparency. The suppression field is established between Grid 1 at ground potential and Grid 2 at -300 V. Fringing field effects are reduced by Grid 3, also at -300 V. Spacing between wires is determined by the requirement that the potential midway between wires be negative relative to the plasma potential by several times the electron temperature. The wire diameter is
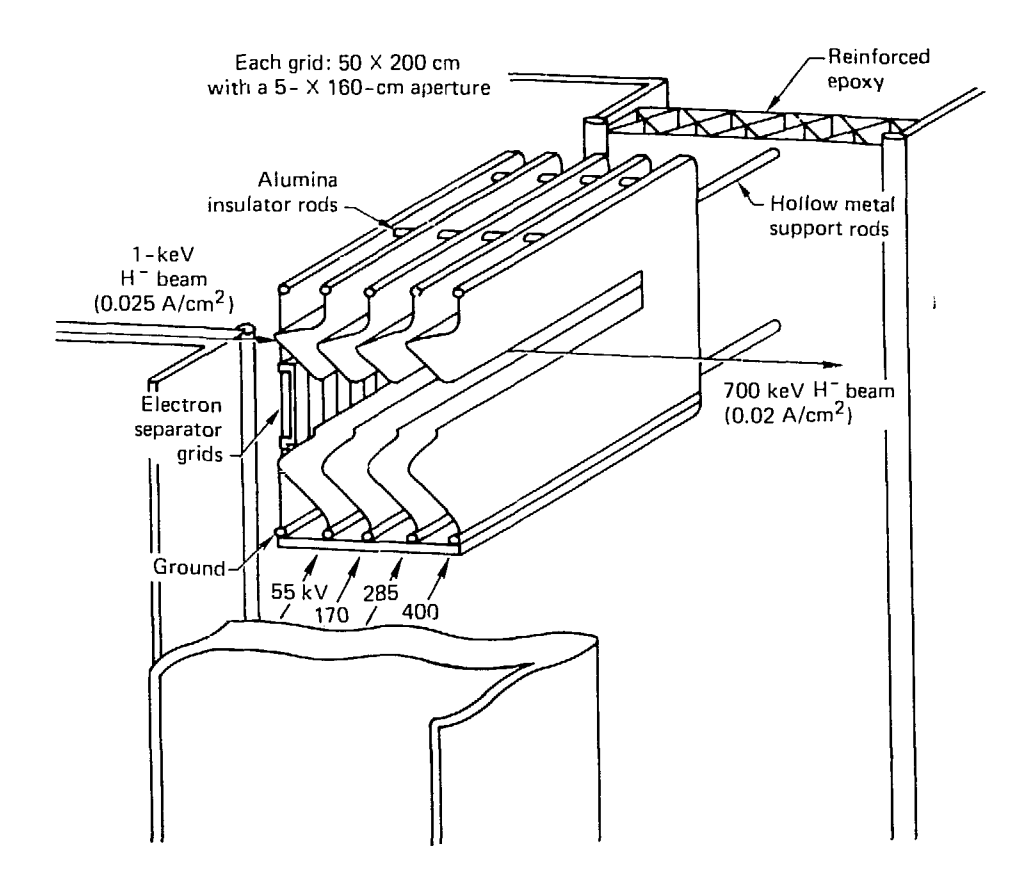
Fig. 4-6. Details of 400-keV grid assembly.

determined by the sputtering lifetime required and by the effect of wire diameter upon fringing fields.

The negative grids will collect about 1 mA/cm^2 of positive ions (mostly H_2^+) extracted from the background plasma. The grid power requirement at 300 V will be only about 100 W.

It is possible to ground either end of the acceleration column and to operate the other end at positive or negative high voltage. It is convenient in this design to ground the ion source end of the accelerator to simplify the
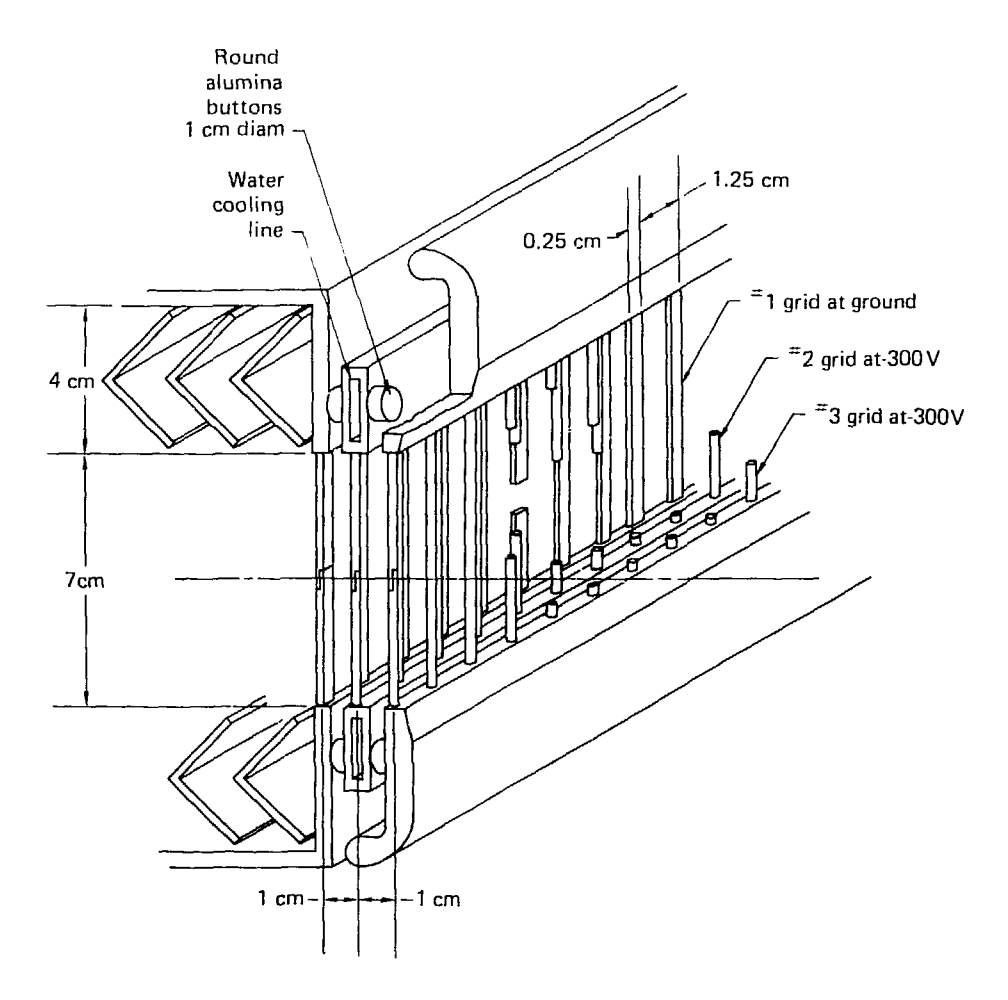
Fig. 4-7. Electron suppression grids to prevent thermal electrons from entering H⁻ accelerator.

pumping of gas from the ion source and to simplify the many electrical and mechanical connections to the low-energy positive ion source and to the charge-exchange cell. The output end of the accelerator will be at +400 kV, where the H^- beam will enter a region of uniform potential including the stripping cell, the ion deflector, and the ion dump collecting the charged components emerging from the stripping cell. A transition region is then required to return the neutral beam to ground potential for injection into the TMR.

Equipotential shields are required on all sides of the region at +400 keV to maintain uniform potential gradients. We specify four equipotential shields at voltages corresponding to those of the intermediate electrodes along the acceleration column.

The energy released during a high-voltage breakdown ($\frac{1}{2}CV^2$) must be not more than a few joules to avoid pitting and deconditioning the electrodes.[4-15] This limitation requires an external voltage protective circuit to isolate the effects of a breakdown and to suppress the arc. The limitation on capacitively stored energy also limits the areas and spacings of high-voltage electrodes and shields.

The maximum size of the acceleration column is limited by the interelectrode capacitance of the fourth acceleration stage, for which V = 115 kV and the spacing d is a minimum of 7.5 cm. Because of the electrode shape the average value of d will be at least 10 cm. In the vacuum of 10^{-4} Torr we can tolerate an energy release of 2 to 10 J per breakdown. This release leads to an allowable interelectrode capacitance of 250 pF and a maximum electrode area of 3 m^2. This area is ample for the 400-kV acceleration column. Because of the stored energy limitation, several parallel sets of equipotential shields are required to enclose the 400-kV uniform potential region.

Electrons and positive ions will be produced within the acceleration column by electron detachment of H⁻ and by ionization of the background H_2. Some of the electrons and positive ions will be collected by the intermediate electrodes and will constitute a load on the voltage divider. This load can be computed by integrating the rates of electron and ion production along the 30-cm beam path through the accelerator.

The rate of electron production within the acceleration column by detachment from H⁻ and by ionization of H_2 gas is

$$\int n_{gas} (\sigma_{-1,0} + \sigma_i) \, I^- \, dx = 0.33 \text{ A} \quad , \tag{4-3}$$

if $n_{gas} = 3.3 \times 10^{12}$ cm⁻³ and $I^- = 5.342$ A. In the integration we have taken into account the variation of the cross sections with H⁻ energy.

Similarly, the rate of slow ion production by ionization of H_2 is

$$\int n_{gas} \sigma_i \, I^- \, dx = 0.46 \times 10^{-14} \, n_{gas} \, I^- = 0.081 \text{ A} \quad . \tag{4-4}$$

Most of the ions and electrons will be accelerated with the beam, but some fraction will be collected by the electrodes. We should design for an electron load of about 0.03 A and for an ion load of about 0.01 A collected by the intermediate electrodes and constituting a load upon the potential divider. This computation assumes that the background gas density is equivalent to a gas pressure of 10^{-4} Torr at room temperature.

The accelerator efficiency will be determined by the power consumed by the electrons and slow ions produced in the background gas. When we assume that the total energy consumed by an ion-electron pair or by an electron detachment is 400-keV, the power loss is 132 kW.

Experience is available on long-term operation of accelerators in the 400-kV voltage range at lower beam currents.[4-16]

Insulation Problems

Accelerator standoff insulators will be ceramic with a resistive coating to avoid electrostatic charge accumulation. This resistive coating must be developed for the purpose because previous attempts to apply such coatings have resulted in enhanced emission of secondary electrons.[4-17] The insulators must be shielded from direct exposure to radiation and to particles emitted by the beam. Standoff insulators are also required to support the equipotential shields. Figure 1-5 shows the standoff insulators and the other insulators required.

A large portion of the main vacuum tank will be at 400 kV to enclose the uniform potential region. This is done by enclosing the main vacuum tank in a pressurized atmosphere of sulfur hexafluoride, which has an insulation strength several times better than vacuum or atmospheric air. All of the external high-voltage circuitry is enclosed in the same SF_6 pressurized tank, and will also be enclosed in equipotential shields for high-voltage reliability.

Two large-area epoxy insulators are required to isolate the 400-kV portion of the vacuum tank from the grounded portion. The epoxy insulators are exposed to vacuum on one side and to the pressurized SF_6 on the other side. The geometry of the vacuum tank provides shielding from x-ray and particle bombardment.

A filled epoxy matching the coefficient of expansion of the metal housing and reinforced with fiberglass rods is cast in place to form the insulator.[4-18] A conductive coating is applied to the epoxy surface to suppress secondary emission and to inhibit outgassing.

High-Voltage Protective Circuit

The high-voltage protective circuit must be designed to extinguish a
breakdown across a high-voltage gap before the breakdown becomes fully de-
veloped and without perturbing the voltages across adjacent gaps in the high-
voltage assembly. The protection is accomplished by limiting to a few joules
the energy released in a breakdown and thereby avoiding the production of
charge carriers by damage to electrode surfaces.

The protection is easier to accomplish in high vacuum than in gas dis-
charges because of the slower risetime (1 to 2 μm) and lower peak currents of
high vacuum sparks in comparison with gas discharge sparks. Consequently, the
allowable release of stored energy in a breakdown without damaging electrode
surfaces by pitting is several joules perhaps as high as 40 J.[4-15]

Safety circuits are required in addition to the arc suppression cir-
cuits. In Fig. 4-8 we show the high-voltage protective circuit, which in-
cludes seven components. We shall describe these components beginning at the
acceleration electrodes and working back to the 400-kV power supply to show
how the components perform the required function.

As shown in Fig. 4-8, each branch of the high-voltage circuit requires a
voltage divider to supply the three intermediate electrodes of each acceler-
ation column and each assembly of equipotential grids. The current capacity
of the voltage dividers should be larger than the electrical load on the
intermediate electrodes, about 0.03 A. The voltage dividers may be either
resistors or zener diodes and will consume about 40 kW.

The RC time for recharging the interelectrode capacitance will be
0.7 μs, representing the recovery time to reestablish normal voltage after the
quenching of a breakdown. Faster operation and less power loss is possible if
zener diodes are used in series with resistors.
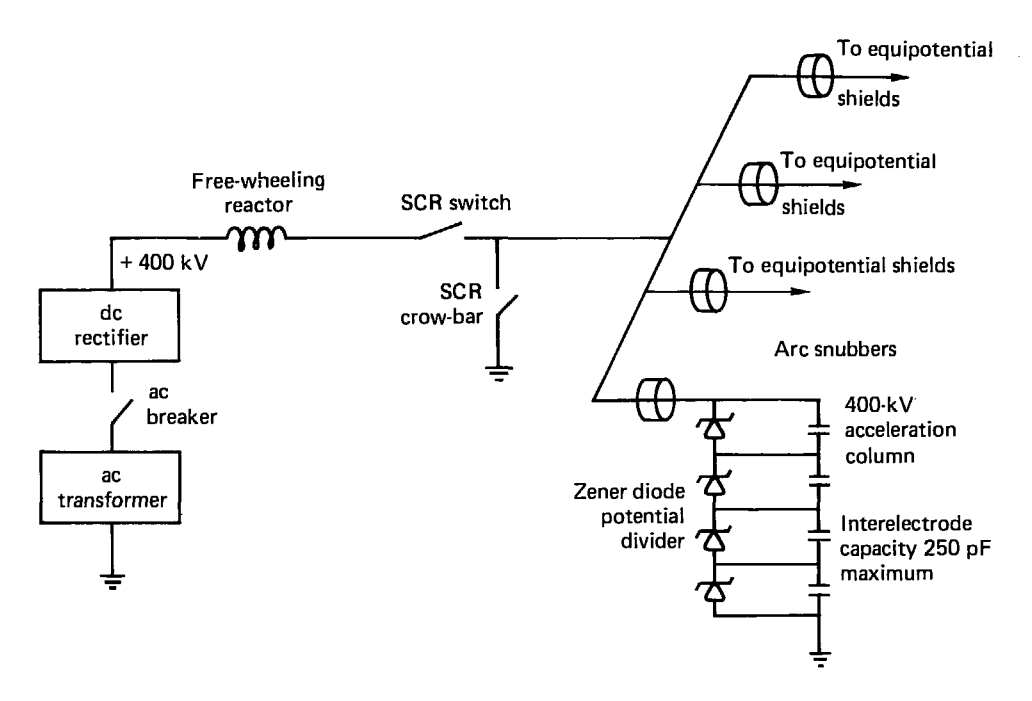
Fig. 4-8. High-voltage protective circuit.

The electrical load of the equipotential grids will be very small because $I^- = 0$ and n_{gas} is reduced by an order of magnitude. A few milliamperes of divider current will be sufficient to supply these grids, with negligible power consumption.

Each branch of the high voltage circuit feeding the acceleration column and the four or five sets of equipotential grids will be protected by an arc snubber[4-19] capable of dropping the applied voltage within a microsecond of the onset of a breakdown between electrodes. The arc snubber consists of an assembly of ferromagnetic cores in which eddy currents are generated by the fast current pulse caused by the breakdown.

The eddy currents in the arc snubber have the effect of a time-dependent pure resistance. Therefore, the total voltage applied to the acceleration column will be reduced at the onset of an arc such that the arc will be quenched at one electrode gap without increasing the voltages at adjacent gaps. With proper design most of the arcs will be quenched by the snubber and voltage divider, which have no active components.

Tests of snubber performance for a single-gap 40-kV accelerator indicate time constants between 0.07 and 0.27 µs, depending upon the capacitance and initial voltage. This range is fast enough to quench a vacuum arc with a risetime of several microseconds.

Other high-voltage elements, such as the electrostatic shields that do not carry significant currents, can be protected by inductive type arc suppressors[4-20] which are considerably smaller components than the magnetic-core arc snubbers previously described.

It will be necessary to back up the passive arc snubber with an actively operated crowbar and high-voltage switch to interrupt the high-voltage dc power in about 2 µs. A well-tested and economical design for this purpose consists of a string of SCR's as a switch in series with the dc high-voltage power supply and load, and a second string of SCR's as a crowbar to ground. It is possible to open the SCR series switch by momentarily shorting the power supply to ground through the crowbar. The crowbar is then reopened by an LC commutation network.

An SCR valve operating on this principle has been developed and tested at 400-kV for HVDC transmission.[4-21] A similar valve is now operating at the 120-kV LBL test stand.[4-22]

Vacuum tubes have also been used as high-voltage switches and crowbars, but not at 400 keV. It appears that SCR's are less expensive and require less development for this purpose than vacuum tubes.

The system will be programmed to close the SCR switch and to reestablish operation a few milliseconds after an interruption. The interruption time should be short in comparison with the 0.1-s ion lifetime in the TMR plug.[4-23] If for some reason this is not possible within a specified time interval, it may be necessary to open the ac circuit breaker.

It will be necessary to protect the 400-keV power supply from over-current and over-voltage when the SCR crowbar is fired. The current limitation must be effective until either the SCR crowbar is reopened by the commutation circuit or until the ac breaker is opened, which may be a maximum of 1/60 s later when the ac current passes through zero.

The commutation circuit in the 120-kV LBL system reopens the SCR crowbar in a half-period of 23 μs. Therefore, a current-limiting inductance of 0.1 Henry is sufficient to limit the current rise to 100 A while 400 kV is applied to the inductance for 23 μs. Such a pulsed voltage can be supplied by a free-wheeling back-biased reactor.

The ac circuit breaker would normally be installed to interrupt the low-voltage ac feeding the primary of the transformer in the 400-kV power supply. However, it may be considered more positive to install the breaker in the high-voltage output of the transformer, as shown in Fig. 4-8. A high-voltage ac breaker interrupts the circuit when the current goes through zero, so the maximum delay time may be 1/60 s.

There are several motivations for changing the ac frequency to 400 Hz rather than 60 Hz. The faster response time of the breaker is one of these motivations. Other motivations would be the smaller size of the transformer core and of the ripple filter, if any. A cost study is required to resolve this possibility.

Voltage Regulation

A great saving in capital cost and operating efficiency is possible if the 40-MW high-voltage power supply is not regulated in the usual sense of the word. A large shunt regulator or series regulator would be very expensive and would consume a large fraction of the output power. If the TMR can tolerate 5 to 10% fluctuations of injected neutral-beam energy, a large savings would result.

It would be necessary to regulate the arc power of the ion sources to follow fluctuations in power supply voltage in order to maintain the proper conditions for optimized beam optics. Arc power regulation is much more simple than high-voltage acceleration regulation because of the low voltages and low power involved.[4-15]

It is also possible to eliminate the need for regulation by making the extracted current density and thereby the beam current fluctuate with the 3/2 power of the high voltage. This fluctuation results in a beam of constant cross section and could be accomplished by making the positive ion extraction voltage track with the high-voltage ripples.

METAL VAPOR STRIPPING CELL

The physics of atomic collisions in a metal vapor stripping cell have been described in our previous reactor designs.[4-13] The mechanical design of the metal vapor stripping cell is essentially the same as that of the cesium vapor double-charge-exchange cell previously described. Therefore, the only new material required in this section is a discussion of some design decisions applying to this application.

The purpose of the stripping cell is to convert the H^- beam to H^0 at maximum efficiency by collisional electron detachment. The maximum conversion efficiency F^0 is limited by ionizing collisions converting the H^0 to H^+. The conversion efficiency is relatively high (up to 65% for vapor cells or 85% for plasma cells) because the cross section for detachment of the first electron is several times larger than the ionization cross section. For 400-keV H^-, the optimum stripping cell thickness for maximum F^0 is 1×10^{16} vapor atoms/cm^2 or 0.2×10^{16} plasma ions/cm^2. Such a plasma cell without background gas is not a trivial development; therefore, we choose a vapor cell for this application that is adequate for the purpose.

Metal vapors are preferred to other types of gases because they can be easily condensed without large gas pumping systems. Other condensable vapors such as CO_2 or H_2O have disadvantages, such as electrostatic charge build-up on condensed insulating surfaces and production of incondensable gases by dissociation of molecular vapors. Atomic gases such as argon, xenon, etc., are undesirable because they form thermally insulating layers on the condens-ing target and therefore can be used for a limited time only. The choice of metal vapor for the stripping cell will be determined largely by the scat-tering of the vapor by the beam. This scattering will be the only major loss of vapor, if we use LN cooled baffles, suitably located, and a plug type noz-zle. A low-Z metal such as lithium may be less objectionable as a reactor contaminant than a high-Z metal, but it is more subject to loss by momentum transfer from the D^- beam to the target.

For several reasons it will be necessary to develop the metal vapor stripping cells to such a level of efficiency that there is negligible vapor contamination of the system outside the cells. It is assured that a metal vapor flux of less than 10^{11} atoms/cm^2-s will be tolerable. This flux should be sputtered away by a background current density of several $\mu A/cm^2$.

Cold fingers in noncritical locations will be required to collect whatever does escape. With these assumptions any of the alkali metals will be satisfactory for the stripping cell.

Finally, a design decision must be made whether or not to operate the stripping cell in a mode suitable for beam direct conversion, in which the kinetic energy of the residual charged beam is electrostatically recovered to improve the overall efficiency. As previously described,[4-13] beam direct conversion probably requires an overdense stripping cell to eliminate the residual H^-. Consequently, the conversion efficiency F^0 will not be optimum. The F^0 penalty for an overdense plasma cell is small, but is somewhat more significant for an overdense vapor stripping cell. For an optimized vapor cell $F^0 = 0.6$, while for an overdense cell F^0 may be as small as 0.45.

Furthermore, we believe that thermal conversion of the residual charged beam energy is practical only if electrostatic direct conversion is not used. The two types of beam energy conversion may not be compatible.

From these considerations we can compute the injection efficiency of three alternative systems using a consistent set of assumptions:

$F^0 = 0.6$ for optimized cell; 0.45 for overdense cell

Cost of H^- production = 20 keV/H^-

Thermal conversion efficiency = 30%

Direct conversion efficiency = 70%

Under these assumptions the injection efficiencies for three alternative systems are as follows, not including thermal conversion in the H^0 beam dump:

System		Percent
1.	Optimized stripping cell without thermal conversion	57.1
2.	Optimized stripping cell with thermal conversion in the H^+ and H^- collectors	64.5
3.	Overdense stripping cell with beam direct conversion of H^+ only	67.7

The difference in efficiency between System 2 and System 3 is trivial, depending upon details in the assumptions. System 2, with thermal conversion, has two advantages over System 3:

- The beam direct-converter system, operating upon H^+, requires a collection electrode at a potential 400-kV above the stripping cell potential; this makes a total voltage difference of 800 kV relative to the negative ion source, while the thermal converter requires a voltage difference of only 400 kV.

- The useful beam per unit area is greater with an optimized stripping cell.

For these reasons we choose an optimized stripping cell with thermal conversion of the residual H^- and H^+ beams, these beams will be approximately equal in current as they emerge from the stripping cell.

DISPOSAL OF CHARGED BEAMS

The charged beam emerging from the optimized stripping cell will consist of roughly equal currents of H^+ and H^- that must be deflected from the neutral-beam line and disposed of. Magnetic deflection using the fringing field of the magnetic containment device is the usual solution for this. However, the TMR fringing field at this point is in the wrong directon for charged beam deflection. A sweep magnet suitable for a beam cross section 7 × 50 cm would occupy an inconveniently large volume near the reactor. Therefore, it is expedient to use a transverse electrostatic field of about 5 kV/cm to deflect the H^- and H^+ $\pm$ 15°, as shown in Figs. 1-5 and 4-7.

The deflection electrodes should be about 50 cm long, followed by a drift space of 75 cm to deflect the charged beams $\pm$ 20 cm. The beams will then be collected at grazing incidence by pressurized water-cooled collectors

connected to a steam generator for thermal energy recovery. No attempt will be made to decelerate the beams before collection, since this may be difficult when both positive and negative ions are involved in the same system.

The electric field induced by separation of the H^- and H^+ beams will probably be neutralized by the background plasma and therefore will not affect the trajectories. However, it is easy to compute an upper limit for the electric field strength using a one-dimensional model and Gauss's law, neglecting the neutralization by background plasma. This upper limit is $E = jb/\varepsilon_0 v$, where $jb = 2.2-A/m$ charged-beam current per unit length. Therefore, E is not more than 0.7 kV/cm, which is small compared to the applied field of 5 kV/m. The maximum possible deflection due to beam space charge is 5 cm, which can be allowed for in the design of the collectors.

Stripping of the H^0 and H^- in this region will be small because we are designing for a residual gas pressure of 10^{-5} Torr. The largest gas load in this region will be from the charged beam dumps.

In order to avoid loading the deflection electrodes with electrons produced in the stripping cell, we will operate one electrode at +400 kV (the same potential as the stripping cell) and operate the other electrode at +340 kV. Consequently, the H^- will be accelerated by a few percent while passing through the deflection electrodes and the H^+ will be decelerated. The asymmetry in the deflections will be small and not important.

VACUUM PUMPING AND DRIFT DUCT BLOCKING

In any negative-ion-based neutral-beam system, a tremendous volume of gas must be pumped relative to the neutral-beam current.

The positive-ion source has a gas efficiency of 30%. Thus, for every ampere of positives leaving the source, 2.33 A of equivalent neutral current escapes.

The double-charge-exchange cell is 20% efficient; i.e., for every ampere of positives that enters the cell, 0.2 A is changed to negatives but 0.8 A escapes as neutrals that must be pumped away.

An optimum cesium stripping cell is 62% effective. Then for every ampere of high-energy neutral beam that leaves the cell, 0.61 A of high-energy residual ions are lost to the beam dumps. Gas in this region must be pumped at the lowest possible pressure as any reionization of the beam on background gas is a direct loss of high-energy beam.

The advantage, as far as pumping goes, of negative-ion-based systems using double-charge-exchange is that the additional cesium vapor plume that crosses the beamline acts as a gas curtain. This high resistance to gas flow through the cell allows us to pump more of the gas in a higher pressure zone ahead of the double-charge-exchange cell. The metal vapor stripping cell also prevents gas in the accelerator region from diffusing downstream into the drift duct.

Figure 4-9 is a graphic representation of gas flow in the plug injector, and illustrates that the negative-ion gas efficiency of a double-charge-exchange source is 4%, i.e., 4% of input gas is converted to negative ion beam. Figure 4-9 also shows that for an ampere of neutral-beam injected, 39 equivalent A must be pumped at various pressures.

The largest fraction of gas is pumped at 2×10^{-3} Torr in the region between the source and the double-charge-exchange cell. From Table 4-1 and Fig. 4-9, the gas involved is

$$Q_A = \frac{0.19 \times \frac{70\%}{2.5\%} \times 3.2 \text{ A}}{2 \text{ ions per molecule}} = 8.5 \frac{\text{Torr-litre}}{\text{s}} \tag{4-5}$$

At 2×10^{-3} Torr, this throughput requires a pumping speed of 4250 litres/s. This speed will be accomplished using two large diffusion-ejector pumps.
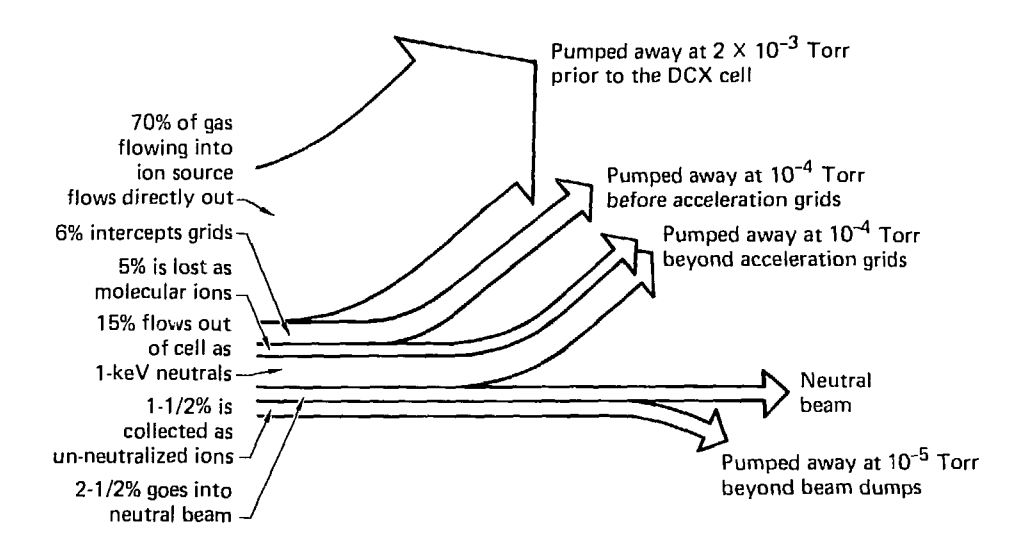
Fig. 4-9. Beamline pumping load—97.5% of input gas.

The throughput required in the region between the double-charge-exchange cell and the stripping cell is

$$Q_B = \frac{0.19 \times 26\%/2.5\% \times 3.2 \text{ A}}{2 \text{ ions per molecule}} = 3.2 \frac{\text{Torr-litre}}{\text{s}} \quad . \tag{4-6}$$

This throughput will be accomplished using recycling cryocondensing panels, shown in Figure 4-10, in the region surrounding the acceleration grids. The area of cryopanel in this region is

$$A_B = \frac{3.2 \text{ Torr-litres/s}}{10^{-4} \text{Torr} \times 4 \text{ litres/s/cm}^2} = 0.8 \text{ m}^2 \quad . \tag{4-7}$$

The third pumping region is between the stripping cell and the reactor and involves pumping residual gas from the beam dumps at 10^{-5} Torr. Because the vapor pressure of H_2 at 4.2 K is greater than 10^{-7} Torr, the panel

113

LN$_2$/LHe out

LN$_2$/LHe in

Gas evacuation ducts

Movable vacuum shield door

LN$_2$ cooled chevrons

LHe cryopanel
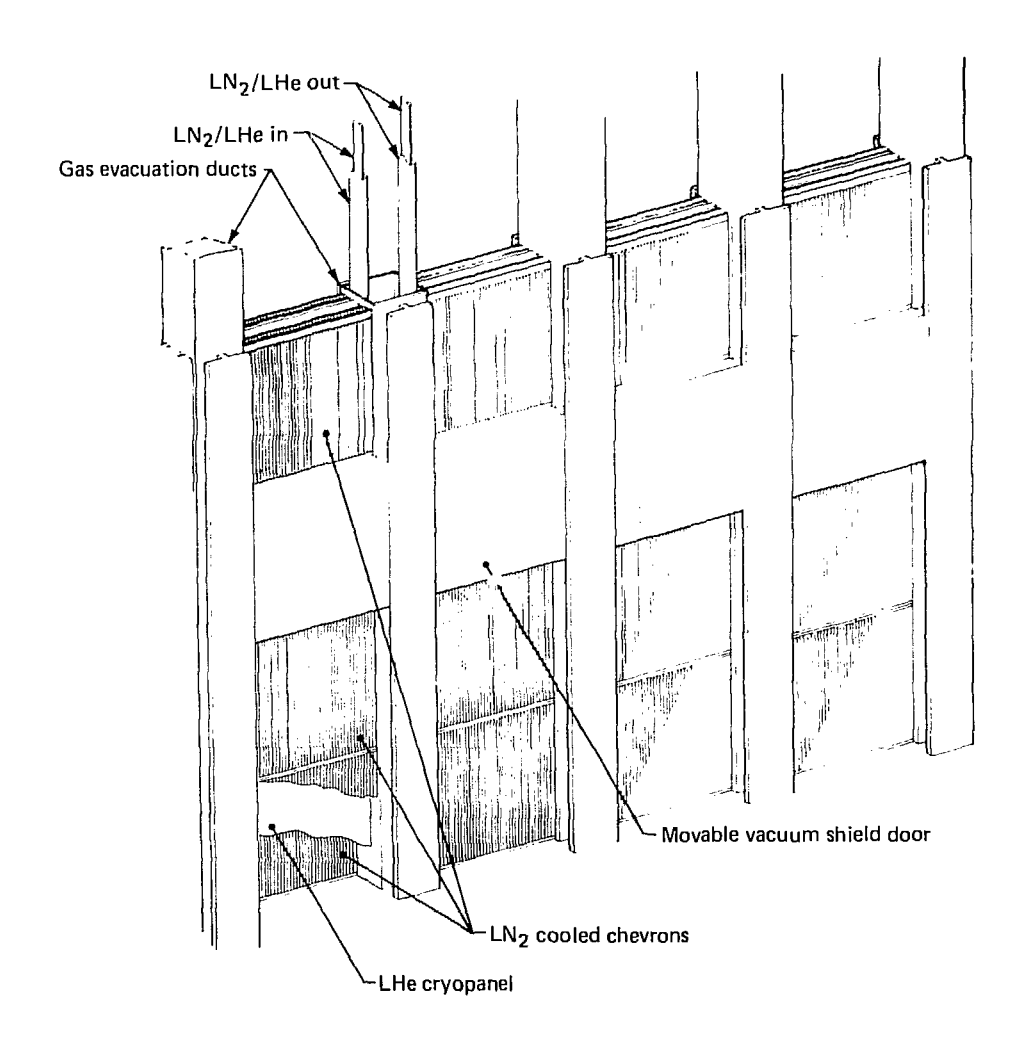
Fig. 4-10. Cryopanels for continuous operation.

must be subcooled to 3.8 K in order to maintain a sticking fraction of nearly unity. The panel area required is

$$A_C = \frac{\frac{1}{2} \times 0.19 \times 1.5\%/2.5\% \times 3.2 \text{ A}}{10^{-5} \text{ Torr} \times 4 \text{ litres/s/cm}^2} = 0.5 \text{ m}^2 \tag{4-8}$$

Modern experiments using neutral beams in a pulsed application have encountered beam attenuation in the drift duct leading to the reactor.[4-24] This beam attenuation is primarily due to out-gassing of the duct walls caused by bombardment with reionized high-energy particles. Drift duct blocking will not present a problem in this design for two reasons. First, the neutral-beam current density is low enough that the density of particles reionized and striking the walls will be reduced. Second, and more important, modern neutralizers use gas while the TMR design uses metal vapor; i.e., where the TMR stripper isolates the duct from the majority of beamline gas, the modern neutralizers are suppliers of the gas that initiates the duct blocking phenomenon.

PROTECTION AGAINST NEUTRON, MICROWAVE, AND SYNCHROTRON RADIATION

An injector can be damaged by excessive levels of radiation impinging on sensitive elements. The usual form of this sensitivity is degradation due to bulk heating. The TMR plug injector will be subjected to four main types of radiation (neutrons, gamma, synchrotron, and microwaves injected for rf heating) which it must survive for one year of dc operation, at least. Actual Monte Carlo calculations of the neutron and gamma radiation striking various components have not yet been made for this injector design. This discussion will be based on estimates of synchrotron and microwave radiation as well as comparisons to Monte Carlo calculations that have been performed for other injector designs.

D-D reactions produce 2.45-MeV neutrons, and D-T reactions produce 14.1-MeV neutrons. Neutrons produced in the plug plasma will be able to enter the neutral beam duct at various angles, with some small fraction streaming directly down the beamline until stopped either by a beamline component or the back wall. Primary neutrons striking the duct walls will produce gamma radiation and secondary neutrons. Neutron radiation from the plasma is line-of-sight dependent, and sensitive beamline components are therefore located where a direct view of the plasma is not possible. However, gammas and secondary neutrons evolved from primary neutron interactions prevent radiation levels from dropping off to zero anywhere in the injector.

Synchrotron radiation is higher in the plug than elsewhere in the reactor due to the combination of high electron temperature and high magnetic field. The synchrotron radiation and any ECRH microwave energy not absorbed by the plasma is able to turn corners based on what waveguide characteristics are perceived by the wave as it travels throughout the injector chamber.

Susceptible materials in the injector include the large-area epoxy insulating walls, the alumina insulators, and high-voltage feedthroughs, liquid-nitrogen-cooled chevrons, and liquid-helium-cooled aluminum cryopanels (see Table 4-2). Each of these has been observed in Monte Carlo analysis of other beamlines[4-25] and found to have sufficient radiation resistance to operate for a full year. All epoxy and LHe surfaces can be shielded from line-of-sight to the plasma to avoid most high-energy neutron and synchrotron radiation. Even so, it may be necessary to cover the inside surface of the epoxy wall with ceramic tiles to inhibit outgassing. Alumina insulators must be located in the acceleration and deceleration regions of the injector at locations near the injector centerline. Previous data have shown, however, that the radiation levels at this distance from the plasma are low enough.

TABLE 4-2. Preliminary design limits for radiation-sensitive components.

Cryopanel neutron and gamma heating rate design limits
      Peak, W/kg   2000
      Average,W/kg   6

Insulator gamma plug neutron dose rate design limits
      Epoxy, rad/s   5000
      Alumina, rad/s   1000

Insulator gamma fluence design limits
      Epoxy, rads 3×10^9 to 3×10^{10}
      Alumina, rads 3×10^{11} to 3×10^{12}

Insulator-fast neutron fluence design limits
      Epoxy, n/cm^2 10^{18} to 10^{19}
      Alumina, n/cm^2 10^{20} to 10^{21}
(Damage caused by a neutron fluence of 4×10^8 n/cm^2 is
approximately equal to damage caused by 1 rad of gamma.)

Some regions of the beam duct near the first-wall aperture will require water
cooling but the power density falls off rapidly due to the glancing angle of
the neutrons striking the duct walls.

    Two factors help to reduce the neutron radiation entering the injector.
First, the plasma is lower density than in the cases studied in Ref. 4-25.
Second, this is a hydrogen injector and produces a predominantly hydrogen plug
plasma. Thus, the number of fusion reactions delivering neutrons to the in-
jector will be lower than the cases for which we have Monte Carlo data that
were D^0 injectors. In addition, the injection of ECRH (39 MW) into each
transition region of the plasma takes place 7 m from the injector aperture;
therefore any unabsorbed ECRH is mostly attenuated before reaching the in-
jector. A conservative estimate of ECRH power levels entering the duct is
3 W/cm^2.

    The power density of synchrotron radiation is an order-of-magnitude
higher than the ECRH level. Synchrotron radiation in the amount of 3 MW is
produced in each plug. Let us assume a first-wall radius of 2.25 m and a line

source of radiation 50 cm long (equal to the length of the injector aperture). This assumption gives a power density of 30 W/cm^2 at the first wall. This level is still an order of magnitude or more below the neutron and gamma levels discussed in Ref. 4-25 so that our situation is less severe.

Neutron and gamma radiation remain the most significant source of potential damage in the plug injector. We are confident that careful placement of the most sensitive elements of the beamline will enable the injector to operate reliably for a year before some maintenance may be required.

REFERENCES

4-1. R. W. Moir, W. L. Barr, G. A. Carlson, W. L. Dexter, J. N. Doggett, J. H. Fink, G. W. Hamilton, J. D. Lee, B. G. Logan, W. S. Neef, Jr., M. A. Peterson, and M. E. Rensink, Preliminary Design Study of the Tandem Mirror Reactor (TMR), Lawrence Livermore Laboratory, Livermore, CA, UCRL-52302 (1977).

4-2. Value Engineering: Approach to Optimizing Neutral Heating Cost and Performance, Office of Fusion Energy, U.S. Department of Energy report, DOE/ET-0113, (1979).

4-3. H. S. Staten, "Neutral Beam Injectors for the Magnetic Fusion Energy Program: Progress and Prognosis for the Future," IEEE Trans. Nucl. Sci., NS-26, No. 1 (1979).

4-4. J. H. Fink, The Design of a Continuously Operated 1-keV Deuterium-Ion Extractor, Lawrence Livermore Laboratory, Livermore, CA, UCID-17825 (1978).

4-5. E. B. Hooper, Jr. and P. Poulsen, Conference Abstracts of the IEEE International Conference on Plasma Science, June 4-6, 1979, Montreal, Canada, (IEEE Service Center, Piscataway, NJ, 1979), Abstract 1S4, p. 32.

4-6. N. N. Semashko, V. V. Kusnetsov, and A. I. Krylov, Proceedings of the Symposium on the production and Neutralization of Negative Hydrogen Ions and Beams, Brookhaven National Laboratory, Upton, Long Island, NY, (1970), BNL-50727, p. 170.

4-7. K. Berman, "The Plug Nozzle: A New Approach to Engine Design," Astronautics 5, No. 4, 22, (1960).

4-8. A. S. Schlachter, K. R. Stalder, and J. W. Stearns, "D⁻ For tion by Charge-Transfer Collisions of 0.3 to 10-keV Deuterium Ions and Atoms in Cesium, Rubidium, and Sodium Vapors," in *Proc. of XI International Conference on the Physics of Electronic and Atomic Collisions, Kyoto, Japan (1979)*, (Society for Atomic Collision Research, Japan, 1979), p. 526.

4-9. J. E. Osher, *Formation of a D⁻ Beam for Efficient Production of D⁰ at High Energies*, Lawrence Livermore Laboratory, Livermore, CA, UCID-15893 (1971).

4-10. M. Hansen, *Constitution of Binary Alloys* (McGraw-Hill Book Co., New York, 1958), p. 577.

4-11. W. R. Ellis, "Description of OGRA-4 at Kurchatov," Foreign Travel Report, August 28-September 30, 1978, U.S. Department of Energy, Office of Fusion Energy, Germantown, MD.

4-12. J. H. Fink and J. L. Erickson, *Direct Extraction of Negative Deuterium Ions to Form a 0.2 MeV Neutral Beam*, Lawrence Livermore Laboratory, Livermore, CA, UCRL-52843 (1979).

4-13. J. H. Fink and G. W. Hamilton, "A Neutral-Beam Injector for the Tandem-Mirror Fusion Reactor Delivering 147-MW of 1.2-MeV D⁰, *IEEE Trans. Plasma Sci.*, *PS-6*, 417 (1978).

4-14. W. L. Barr and R. W. Moir, *A Review of Direct Energy Conversion for Fusion Reactors*, Lawrence Livermore Laboratory, Livermore, CA, UCRL-78204 (1976), in *Technology of Controlled Fusion, Second ANS Topical Meeting, Richland, WA (1976)*.

4-15. W. R. Baker and D. B. Hopkins, *Present and Future Technology of High Voltage Systems for Neutral Beam Injectors*, Lawrence Berkeley Laboratory, Berkeley, CA, LBL-7261 (1978), presented at Plasma Heating Development Requirements Workshop, Gaithersburg, MD.

4-16. J. Huguenin, and G. Visconti, "CERN-PS 540-keV High Gradient Preinjector Tube: Results of Two Years' Operation and Complementary Tests," Proc. of the 3rd Intern. Symposium on Discharges and Electrical Insulation in Vacuum, Paris (1968).

4-17. D. K. Davies, "Secondary Electron Characteristics of Insulator Surfaces Before and After Impulse Flashover," 8th Intern. Symposium on Discharges and Electrical Insultation in Vacuum, Albuquerque, NM (1978), (Sandia Laboratories, Albuquerque, NM, 1978).

4-18. J. P. Burkhart and C. F. Hofmann, "Applications of Cast Epoxy Resins in Power Circuit Breakers" C 74 064-2, Proc. of IEEE Power Engineering Society Winter Meeting, New York, NY (1974), (IEEE, Piscataway, NJ, 1974).

4-19. J. H. Fink, W. R. Baker, and H. M. Owren, Analysis and Application of a Transformer Core that Acts as an Arc Snubber, Lawrence Livermore Laboratory, Livermore, CA, UCRL-79016, Rev. 2 (1979).

4-20. W. F. Praeg, "Protection of Neutral Beam Accelerator Electrodes from Sparking," in Proc. 7th Symposium on Engineering Problems of Fusion Research, Knoxville, Tenn. (1977), (IEEE, Piscataway, NJ, 1977).

4-21. C. Beriger, I. Boban, and W. Faust, "A New SCR Valve for the Performance Test Circuit of the 400-kV Working Group at Mannheim-Rheinau", Brown Boveri Review 60, No. 2/3, 100 (1973).

4-22. J. V. Franck, A. A. Arthur, L. A. Brusse, and W. Low, "An SCR Series Switch and Impulse Crowbar at the Lawrence Berkeley Laboratory for CTR Neutral Beam Development", Proc. 7th Symposium on Engineering Problems of Fusion Research, ORNL (1977), (Oak Ridge National Laboratory, Oak Ridge, TN, 1977).

4-23. R. S. Devoto and D. J. Bender, "Plasma Models for Standard Mirror Reactors," Lawrence Livermore Laboratory, Livermore, CA, UCRL-81792 (1978).

4-24. L. D. Stewart, Neutral Beam System Reionization Losses, Princeton Plasma Physics Laboratory, Princeton, NJ, PPPL-1469 (1978).

4-25. J. D. Lee, R. H. Condit, C. L. Hoenig, T. P. Wilcox, and J. L. Erickson, Progress Report on the Neutral Beam Radiation Hardening Study, Lawrence Livermore Laboratory, Livermore, CA, UCID-18017 (1978).

CHAPTER 5. BARRIER PUMP NEUTRAL BEAMS

G. W. Hamilton, B. G. Logan

INTRODUCTION

The required low plasma density in the thermal barriers of the Tandem Mirror Reactor (TMR) (g_b not much larger than unity) can be maintained by pumping out trapped ions by means of charge exchange with neutral atoms (D^0 and T^0) injected for the purpose. Conditions must be arranged so that after the charge exchange the ion trapped in the barrier goes to the wall as a neutral and the ion derived from the injected neutral goes into the central cell to become a passing particle trapped between the ambipolar plug potentials. In effect, the injected neutral has pumped out the trapped ion.

In this chapter, we deal with the special problems involved in charge-exchange pumping; we should avoid discussing neutral-beam technology that has been developed for other purposes.

PHYSICS REQUIREMENTS

For the injected neutral to escape from the barrier into the central cell the pitch angle θ after charge exchange must be sufficiently small, and the injected beam energy E_B must be sufficiently large that

$$\sin^2\theta < (1 - \Delta\phi/E_B)/R \quad . \tag{5-1}$$

The potential difference $\Delta\phi(z)$ and the mirror ratio $R(z)$ are defined relative to the potential ϕ_e and magnetic field $B_{mb} = 12$ T at the entrance of the central cell; i.e.,

$$\Delta\phi(z) = \phi_e - \overset{*}{\phi}(z) \quad ,$$

and

$$R(z) = B_{mb}/B(z) \quad . \tag{5-2}$$

The potential $\phi^*(z)$ and magnetic field B(z) are defined at the point the charge exchange occurs. Obviously, the beams for the charge-exchange pump must be injected where the values of ϕ^*, B, and θ are appropriate for the beam energy used. Also, the neutral atom produced by charge exchange must escape from the plasma to the wall without being re-ionized by collisions with plasma ions and electrons. This escape probability should be not much less than unity.

Figure 5-1 shows those regions of velocity space in the thermal barrier where the ions either are passing through the thermal barrier or are trapped within the barrier. The equation of the hyperbola separating the trapped region from the passing region is the following:

$$v_{\parallel}^2 - (R - 1)\, v_{\perp}^2 = \Delta\phi(2q/m) \quad , \tag{5-3}$$

and the loss-cone angle θ_{LC} defined by the asymptotes of the hyperbola is

$$\theta_{LC} = \sin^{-1}(R^{-1/2}) \quad .$$
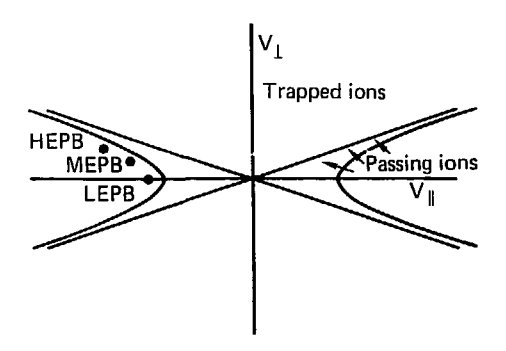
Fig. 5-1. Velocity space diagram showing the regions of velocity space at the center of the thermal barrier in which ions are either passing through the well or trapped within the well—asymptote angle is $\sin^{-1}(R^{-1/2}) = 18.4^\circ$ if R = 10 (arrows indicate the diffusion of trapped and passing ions in velocity space filling up the barrier; ions injected by the three pump beams LEPB, MEPB, and HEPB are indicated in velocity space after acceleration by the potential well).

The passing ions diffuse into the trapped region of velocity space and must be pumped out by the charge-exchange pumps. We must compute the diffusion rate and design the pumps accordingly.

Not all of the injected neutrals will be effective for charge-exchange pumping. Some of the neutrals will be ionized collisionally before they charge exchange, some will penetrate without collisions of any sort, and some will charge exchange with passing ions rather than with trapped ions. Correction factors for each of these effects must be included in the design.

TRAPPING RATE

Central-cell ions passing through the thermal barrier are trapped within the barrier by diffusion through velocity space by ion-ion multiple scattering. If the local mirror ratio $R(z)$ is large, the trapping is caused by pitch-angle diffusion, which is proportional to R. On the other hand, if R is not much larger than unity, the trapping is caused by diffusion of $v_\parallel$, which is independent of R. An empirical equation combining these two effects, scaled from Fokker-Planck results, is

$$J_{trap} = \frac{n_{pass}^2}{5.5 \times 10^9 \, T_{ic}^{3/2}} \, [1 + 0.55 \, R(z)] \text{ trapped ions/cm}^3 \cdot \text{s} \quad . \quad (5\text{-}4)$$

This must be integrated over the volume of the barrier, taking into consideration the reduction in $n_{pass}(z)$ as the ions are accelerated by the ambipolar potential and as the area of the flux tube expands in the reduced magnetic field. The total trapped ion current in each barrier is

$$I_{trap} = 2q \int_{z_{bc}}^{z_p} J_{trap}(z) \, \frac{\pi r_c^2 \, B_c (1 - \beta_c)^{1/2}}{B(z)} \, dz \text{ amperes} \quad . \quad (5\text{-}5)$$

In this integration, the passing-ion density $n_{pass}(z)$ and the potential $\psi^*(z)$ relative to ground can be modeled as follows:

$$n_{pass}(z) = \begin{cases} \dfrac{n_c B_b(z)}{B_{mb}} \left[\dfrac{T_{ic}}{\pi[\phi_e - \psi^*(z)] + T_{ic}} \right]^{1/2} & \text{for } \psi^*(z) < \phi_e \quad , \\[20pt] \dfrac{n_c B_b(z)}{B_{mb}} \left[\dfrac{\exp\ -[\psi^*(z) - \phi_e]/T_{ic}\ -\ \exp\ (-\phi_c/T_{ic})}{1 - \exp\ (-\phi_c/T_{ic})} \right] & \text{for } \psi^*(z) > \phi_e \quad , \end{cases} \tag{5-6}$$

and

$$\psi^*(z) = \begin{cases} \phi_e - T_{ec}\ \ln \left[\dfrac{n_c}{g_b\ n_{pass}(z)} \right] & \text{for } z_b^c < z < z_{b0} \quad , \\[20pt] \phi_e + \phi_c - T_{ep}\ \ln \left[\dfrac{n_p}{g_b\ n_{pass}(z)} \right] & \text{for } z_{b0} > z > z_p \quad . \end{cases} \tag{5-7}$$

These profiles of density and potential are shown schematically in Fig. 2-1. For the magnet design of Chapter 3 the result of the above integration is I_{trap} = 1,076 A for both ends of the TMR.

FOUR-STAGE PUMPING SYSTEM

The power requirement for the pump beam, which may be substantial, is proportional to the beam energy E_B, which Eq. (5-1) shows to be at least equal to ϕ. A large economy is possible by arranging conditions so that ϕ is as small as possible and perhaps even negative. This requires four pumping stages, similar in philosophy to a multi-stage differential pumping system for gas, in which most of the gas is pumped at a high pressure. Only a small fraction of the gas load is pumped in the high-vacuum stage of a well-designed system.

The four stages of the charge-exchange pump will be designated as the gas pump (GP), the low-energy pump beam (LEPB), the medium-energy pump beam (MEPB), and the high-energy pump beam (HEPB).

It is possible to use the gas-pump (GP) stage to pump out most of the trapped particles by charge exchange in the region where $\Delta\phi < 0$ and therefore where E_B may be zero. This charge-exchange pumping requires merely a gas jet directed into the appropriate plasma region--where $\phi^*(z) > \phi_e$ and where the plasma density is low enough for the gas to penetrate into the plasma. This region is in the low-density plasma surrounding the main plasma column of the thermal barrier. Computations[5-1] indicate that trapped particles follow drift surfaces extending out of the barrier plasma because of asymmetric confinement by the plug quadrupole magnetic field. The fraction f_D of the trapped ions on such drift surfaces can be pumped by the gas pump; i.e., $I_{GP} = f_D I_{trap}$.

Another large part of the trapped-ion population is accessible for charge exchange with a low-energy pump beam (LEPB) having sufficient speed merely to penetrate the barrier plasma to the z-axis before undergoing charge exchange or re-ionization. The only requirement for pumping by the LEPB is that the trapped ion be in the region of velocity space such that it spends part of its time in the region $\phi^*(z) > \phi_e$. This requirement defines the fraction $f_{LEPB} = I_{LEPB}/I_{trap}$. To economize on pump beam power, conditions should be arranged to maximize f_D and f_{LEPB}.

The injection speed v_B of the LEPB should be chosen so that a finite fraction of the injected neutrals reaches the z-axis but that a small fraction penetrates completely through the barrier; i.e.,

$$1 < n_b \times \overline{\sigma_T v}/v_B < 4 \quad , \tag{5-8}$$
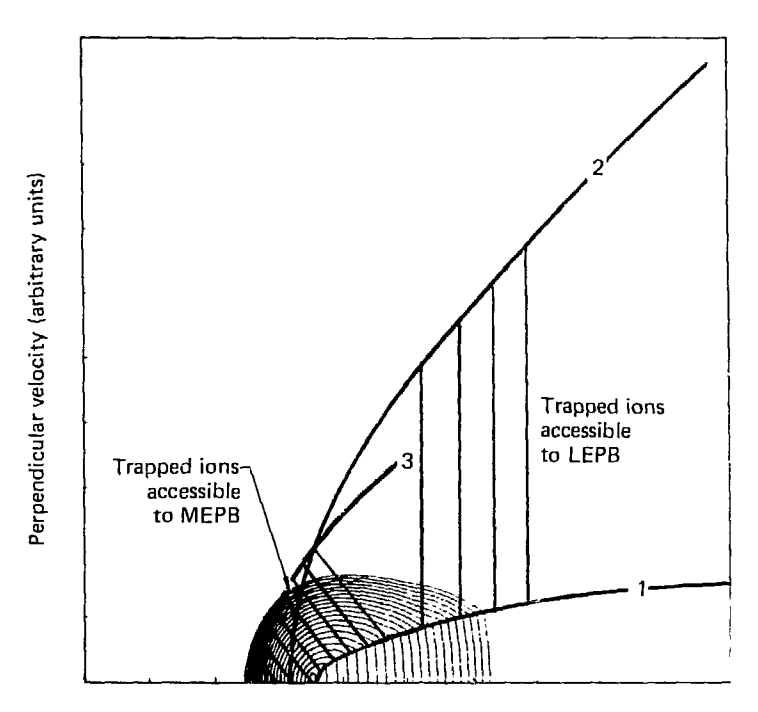
where x = 60 cm is the thickness of the plasma fan in the transition region, and the rate coefficient $\overline{\sigma_T v}$ for beam attenuation includes charge exchange and ionization by barrier ions and electrons. Since v_B is smaller than the plasma thermal speeds, $\overline{\sigma_T v} = 1$ to 2×10^{-7} cm$^3 \cdot$ s.[5-2] Therefore, for $n_b = 1.4 \times 10^{13}$ cm^{-3}, v_B should be between 2 and 17×10^7 cm/s, depending on the plasma temperature and the desired penetration. We have chosen to use 20-kV ion sources for the LEPB. To optimize the beam density and beam divergence, it is convenient to produce the LEPB from a mixture of molecular ions (D_2^+ and D_3^+).

It may be possible to use pellet injection rather than neutral beam injection to attain the desired penetration. However, this seems unlikely because of the high rate of pellet ablation at a 200-keV electron temperature.[5-3]

Fokker-Planck computations show that if $g_b = 2$, most of the trapped ions are accessible to charge-exchange pumping by the LEPB and GP because their trapped orbits extend to the region where $\phi^*(z) > \phi_e$. Figure 5-2 shows contours of trapped and passing ions in velocity space for the condition in which $n_{pass} = n_{trap}$. Three hyperbolas loss surfaces are indicated, corresponding to the mirror ratio R = 10 for passing ions, to the mirror ratio R = 2 for a LEPB injected into a 6-T magnetic field with $v_\parallel > 0$, and to the mirror ratio R = 3 for the MEPB to be described.

The fraction $f_{LEPB} + f_D$ of trapped ions accessible for pumping by the GP and LEPB can be computed by integrating the contours between the two hyperbolas corresponding to the passing ions and to the injected LEPB. This integration results in $f_{LEPB} + f_D = 0.77$.

To pump out the ions trapped more deeply in the potential well, it is necessary to inject neutral beams with sufficient energy E_B to satisfy Eq. (5-1) and thereby escape from the barrier after the neutrals are converted

Fig. 5-2. Contours of ion density in velocity space, computed by a time-dependent Fokker-Planck code. The time is chosen such that $n_{trap} = n_{pass}$, such that $g_b = 2$. The contours are plotted at equal logarithmic intervals, so that the ratio of densities for adjacent contours is 1.39. The three hyperbolas separate the trapped ions from the passing ions for three injection conditions: 1. $R = 10$ for central-cell ions; 2. $R = 2$ for LEPB ions injected into a 6-T magnetic field with $v_\parallel > 0$; and 3. $R = 3$ for MEPB ions injected into a 4-T magnetic field with $v_\parallel = (0.8 \; \phi_b \; q/m)^{1/2}$. The area in velocity space between hyperbolas 1 and 2 is accessible for charge-exchange pumping by the LEPB; the area between hyperbolas 1 and 3 is accessible to the MEPB.

to ions by charge exchange or by ionization. For each of the injected beams, a target area and a beam path must be selected so that ϕ, R, and θ satisfy Eq. (5-1). For economy in beam power, it is best to pump as many trapped ions as possible at an intermediate potential $\Delta\phi_{MEPB}$ with a MEPB and to pump only the ions trapped at the bottom of the potential well with a high-energy pump beam (HEPB) at the potential $\Delta\phi_{HEPB} = \phi_b = 112$ kV.

We shall select $\Delta\phi_{MEPB}$ by using the requirement that 90% of the trapped ions not accessible to the LEPB be pumped by the MEPB; i.e., .

$$f_{MEPB} = I_{MEPB}/I_{trap} = 0.9 (1 - 0.77) = 0.207 \quad ,$$

and

$$f_{HEPB} = I_{HEPB}/I_{trap} = 1 - (f_D + f_{LEPB} + f_{MEPB}) = 0.023 \quad . \tag{5-9}$$

We can obtain $\Delta\phi_{MEPB}$ from Fig. 5-2 by reading the value of $v_\parallel$ at which the 10% density contour intersects the horizontal axis:

$$(1 - \Delta\phi_{MEPB})/\phi_b = [v_\parallel (10\%)/v_\perp (100\%)]^2 = 0.6 \quad .$$

Therefore

$$\Delta\phi_{MEPB} = 0.4 \phi_b \quad . \tag{5-10}$$

Table 5-1 shows the values of E_B and θ required to satisfy Eq. (5-1) for the MEPB and the HEPB, using the specified values of $\Delta\phi$ and R. We must find injection paths satisfying these conditions.

TABLE 5-1. Beam parameters required to satisfy Eq. (5-1) for the medium-energy pump beam (MEPB) and the high-energy pump beam (HEPB).

	MEPB	HEPB
$\Delta\phi = \phi_e - \phi^*$, kV	45	112
$R = B_b/B$	3	10
Maximum θ, degrees	10	8
$E_B = \phi/(1 - R \sin^2\theta)$, keV	50	139

Neutral-Beam Current Requirement

For each of the four stages of the charge-exchange pump, the neutral-beam current requirement is derived from the pumping rate requirements I_{GP}, I_{LEPB}, I_{MEPB}, and I_{HEPB}. The pumping requirements must be multiplied by three factors, F_1, F_2, and F_3, to take into account the interactions not contributing directly to charge-exchange pumping:

• Some of the injected neutrals will be ionized and will not undergo charge exchange. To allow for this, we must multiply by the ratio of rate coefficients $\overline{\sigma_{cx}v}$ and $\overline{\sigma_i v}$ averaged for the speed of the injected neutrals relative to the speed of the plasma ions and electrons. Interactions with both trapped (n_{trap}) and passing (n_{pass}) ions must be included. However, charge exchange with passing ions is not a loss because another neutral is produced which contributes to the charge-exchange pumping. The factor accounting for these effects is

F_1 = injected neutral beam/pumping rate (neglecting the losses due to beam penetration and re-ionization.)

$$\approx \frac{(n_{trap} + n_{pass})\,(\overline{\sigma_{cx}v} + \overline{\sigma_i v}) - n_{pass}\,\overline{\sigma_{cx}v}}{n_{trap}\,\overline{\sigma_{cx}v}}$$

$$= 1 + \frac{g_b\,\overline{\sigma_i v}}{(g_b - 1)\,\overline{\sigma_{cx}v}} \quad ,$$

where

$$g_b = (n_{trap} + n_{pass})/n_{pass} \quad . \tag{5-11}$$

● Equation (5-11) implicitly assumes that the entire injected beam undergoes either ionization or charge exchange. If this is not true, the injected current must be increased by a factor F_2 to compensate for the fraction penetrating without interactions.

$$F_2 = \left\{ 1 - \exp\left[-\int dl \ (n_{trap} + n_{pass}) \ (\overline{\sigma_i v} + \overline{\sigma_{cx} v})/v_B \right] \right\}^{-1} \quad . \qquad (5\text{-}12)$$

● If a finite fraction of the charge-exchange products is re-ionized before escape from the barrier plasma, the neutral-beam requirement is increased by a factor F_3 equal to the reciprocal of the escape probability:

$$F_3 = \exp\left[(n_{trap} + n_{pass}) \ L\overline{\sigma_i v}/v \right] \quad , \qquad (5\text{-}13)$$

where the length of the escape path L depends upon the distance from the plasma surface $X \approx 10$ cm and upon the two angles θ and Φ:

$$L = X/(\sin \theta \ \sin \Phi) \quad . \qquad (5\text{-}14)$$

The pitch angle θ of the trapped ion before charge exchange is roughly equal to the loss-cone angle $\sin^{-1} R^{-1/2}$. The azimuthal angle Φ is a random variable. We must compute the average value of F_3 as Φ varies randomly from 0 to 180 degrees. The result is that for the low density of this reactor example $(1.4 \times 10^{13} \text{ cm}^{-3})$, the exponent is small and F_3 is about 1.2. For the gas pump in the very low density region, $F_3 = 1$.

In this computation, we neglect the possibility of a second charge exchange during the escape from the plasma. The second neutral product will contribute to the pumping and is not a loss.

In this section, we are assuming that each neutral beam consists of only one energy component (this assumption is discussed elsewhere). Therefore, the neutral-beam current requirement for each pumping stage is

$$I^0 = I_{pumping} \times F_1 F_2 F_3 \quad , \qquad (5\text{-}15)$$

where the required pumping rate is

$$I_{pumping} = I_{GP}, \ I_{LEPB}, \ I_{MEPB}, \ \text{or} \ I_{HEPB} \ .$$

The computations for I^0 for each stage are shown in Tables 5-2 through 5-5. In these computations, we specify the use of T^0 for the MEPB and HEPB to fuel the central cell and to take advantage of the better charge-exchange cross section.

Choice of Beam Paths

The location of the GP and LEPB is determined by the potential profile, such that ϕ^* is a few kV above ϕ_e. This location is shown on the potential profile in Fig. 2-1 and in Fig. 1-4.

The beam paths for the MEPB and HEPB are chosen to fit several requirements:

● The beam path must be almost parallel to a magnetic flux line to satisfy Eq. (5-1).

● Each beam must be aimed at the target area where ϕ^* and B have the values shown by Table 5-1. The potentials for the MEPB and HEPB are labeled on Fig. 2-1. Note that there are two possible locations for the MEPB injection.

● The useful part of the beam path must be several metres long so that most of the neutral beam is ionized or charge exchanged in the target region. Realistic conditions must be assumed for the beam density, beam access, and beam divergence.

TABLE 5-2. Neutral-beam requirements for each pumping stage for the following specified parameters: $I_{trap} = 1{,}076$ A (both ends), $n_{pass} = 7 \times 10^{12}$ cm^{-3}, and $g_b = n_b/n_{pass} = 2$.

	Pump stage				
	GP	LEPB	MEPB	HEPB	Total
E_B (from Table 5-1) (keV/atom)	0	10	50	139	
Injected species	D_2	D^0	D^0, T^0	T^0	
Rate coefficients (10^{-7} cm^3/s):					
$\overline{\sigma_i v}$	0.3	0.32	0.51	0.54	
$\overline{\sigma_{cx} v}$	1.4	1.4	0.80	0.31	
f	0.4	0.37	0.207	0.023	1.0
$I_{pumping} = f\, I_{trap}$ (A)	430	398	223	25	1,076
F_1 [effect of ionization and passing ions, Eq. (5-11)]	1.43	1.46	2.27	4.48	
F_2 [attenuation factor, Eq. (5-12)]	1.0	1.0	1.05	1.16	
F_3 [escape factor, Eq. (5-13)]	1.0	1.2	1.2	1.2	
$I^0 = F_1 F_2 F_3\, I_{pumping}$ (A)	615	697	639	156	2,107
Neutral beam power $= I^0 E_B$ (MW)	0	7.0	31.9	21.7	60.6

It appears possible to satisfy these requirements by the beam paths in-
dicated by Fig. 5-3, which shows the magnetic flux lines, and by Fig. 1-4, the
scale drawing. Here we assume that in the final stage of a reactor design the
details of the magnetic field will be reiterated to improve the conditions for
magnetic pumping. Consequently, the correspondence between Fig. 5-3 and
Table 5-1 is only approximate in this early stage of the design.
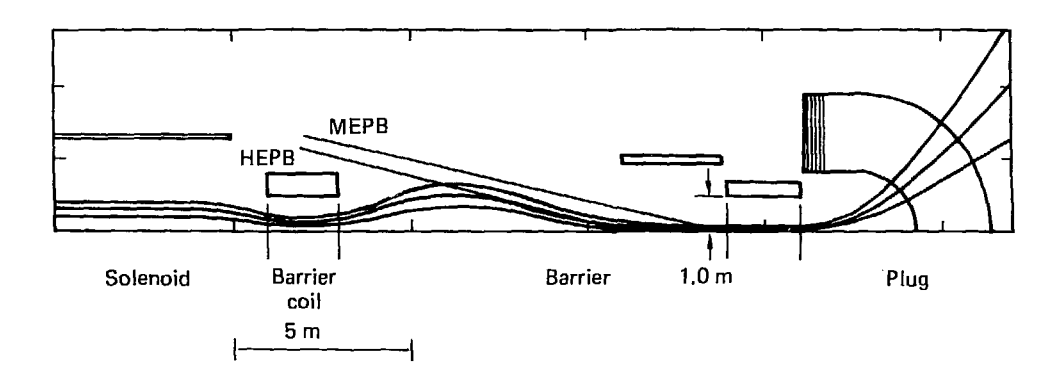
Fig. 5-3. Magnetic flux lines in the thermal barrier, with selected beam
paths for MEPB and HEPB fulfilling the requirements of Table 5-1.

Beam Purity Requirement

Neutral beams derived from positive ions normally consist of a mixture
of several energy components, derived from the mixture of H_1^+, H_2^+, and H_3^+
in the primary beam. This causes a problem for the MEPB and HEPB because the
half-energy and third-energy components will be trapped within the barrier if
their energy is less than the required E_B of Table 5-1. This problem does
not affect the LEPB, for which the energy is not important except for plasma
penetration.

137

To indicate the severity of the problem, we shall compute the factor F_4 defined as follows, without considering the correction factors F_1, F_2, and F_3:

$$F_4 = \frac{\text{primary beam current}}{\text{pumping speed of a mixed-energy neutral beam}}$$

$$= \frac{I^+}{I_1^0 \,\overline{\sigma_{cx} v}_1 \,/\overline{\sigma_T v}_1 + I_2^0 (\overline{\sigma_{cx} v}_2/\overline{\sigma_T v}_2 - 1) + I_3^0 (\overline{\sigma_{cx} v}_3/\overline{\sigma_T v}_3 - 1)} \quad . \quad (5\text{--}16)$$

The subscripts 1, 2, and 3 denote the components derived from T_1^+, T_2^+, and T_3^+. The subscripts cx and T denote the cross sections for charge exchange and for trapping the pump beam by all processes. The reaction rates σv are averaged for the relative speeds of a reactor plasma distribution.[5-2]

All three components contribute to the pumping mechanism by charge exchange. However, I_2^0 and I_3^0 also constitute a load that must be subtracted from the gross pumping speed.

The three neutral-beam components are related to the total pump beam I^+ as follows:

$$I_i^0 = \eta_i F_i \, I^+ \times \text{atoms/ion} \quad .$$

Here the composition of the primary beam is η_1, η_2, and η_3, and F_i is the neutral fraction[5-4] produced in an equilibrium neutralizing cell. Realistic values for the beam composition are 60-20-20%. A more optimistic example is 80-15-5%.

Figure 5-4 shows F_4 computed as a function of E_B for these two beam compositions and for a pure full-energy beam. The pumping speed is reduced by a large factor at energies in the range of the MEPB and becomes less than zero at energies in the range of the HEPB. Consequently, F_4 goes to infinity at high energy.
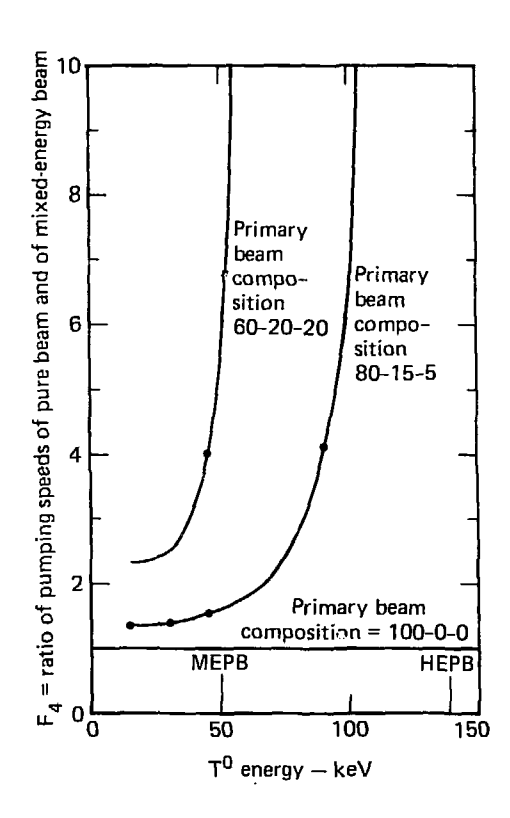
Fig. 5-4. Effect of half-energy and third-energy neutrals in charge-exchange pump beams. The effect becomes severe at higher energies, thus imposing a beam purity requirement.

The figure contains labels: "Primary beam composition 60-20-20", "Primary beam composition 80-15-5", "Primary beam composition = 100-0-0", "MEPB", "HEPB". Y-axis: "F_4 = ratio of pumping speeds of pure beam and of mixed-energy beam". X-axis: "T^0 energy — keV".

It is clear that we must design beams for charge-exchange pumping without contamination by components of energy less than E_B. In principle, there are four ways to do this:

1. Development of a pure T_1^+ plasma source is the most straightforward solution. However, we believe that a 90% pure source is the best attainable, and this is not good enough for the HEPB.

2. Neutral beams derived from T_3^+ will have no low-energy components. However, this implies an ion source voltage of 417 kV for the HEPB. Also, there would be a large power cost because of the inefficient components derived from the T_2^+ and T_1^+ in the primary beam.
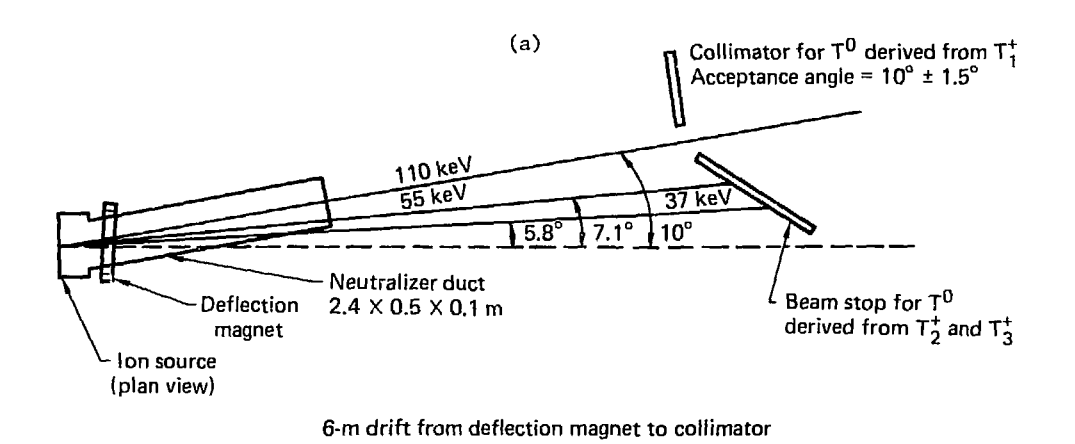
3. Neutral beams derived from T^- will have only one energy component. However, as shown in Chapter 4 the neutral-beam density is only 10 mA/cm^2 and the cost of T^- production is 40 kW per injected ampere.

4. Magnetic separation of T_1^+ from the molecular ions in the primary beam before neutralization is possible. This can be done in a compact system by an iron-core deflection magnet in the high-pressure (10^{-3} Torr) end of the neutralizer, implying a loss of 18% of the full-energy beam by premature charge exchange as the beam passes through the deflection magnet. This penalty seems preferable to the alternatives for the MEPB and HEPB.

The deflection magnet must be compact to minimize the beam loss by premature charge exchange. This is possible if the deflection angle is not large. As shown in Fig. 5-5, it is sufficient to deflect the T_1^+ by 10 degrees to separate the T_1^+ from the 7.1 degree deflection of the T_2^+ and from the 5.8 degree deflection of the T_3^+. The required deflection field is

$$\int B_\perp dl = (2 \, m \, E_B/q)^{1/2} = 0.016 \; T \cdot m \text{ for the HEPB}$$

$$of = 0.010 \; T \cdot m \text{ for the MEPB} \quad . \tag{5-17}$$

This deflection requires a magnetic field strength of only 0.08 T if the thickness of the magnetic field is 20 cm. Including the fringing fields, the overall thickness will be about 40 cm. Figure 5-5 shows the deflection magnet and neutralizer to scale in two views. The deflection magnets are viewed from the side in Fig. 1-4 and therefore are not visible.

The same design can be used for the HEPB and for the MEPB. the conductance of the neutralizer must be adjusted so the gas pressure is a maximum of 10^{-3} Torr for the HEPB and 0.4×10^{-3} Torr for the LEPB. These gas pressures will result in the same 18% penalty for both beams.

(a)

Collimator for T^0 derived from T_1^+
Acceptance angle = $10° \pm 1.5°$

110 keV
55 keV
37 keV

5.8° 7.1° 10°

Neutralizer duct
2.4 X 0.5 X 0.1 m

Deflection magnet

Ion source
(plan view)

Beam stop for T^0
derived from T_2^+ and T_3^+

6-m drift from deflection magnet to collimator

(b)

Ion-core deflection magnet
occupies 40 cm including fringing field
$\int B_\perp\ dz = 0.016$ T-m for $10°$
deflection of 139-keV T^+
Pole-pieces designed for beam optics

Ion source, equivalent to TFTR source
(side view)
110-kV, 50-A total beam/module
80% T_1^+; 20% T_2^+ and T_3^+

Neutralizer duct, about 2.4 X 0.5 X 0.1 m
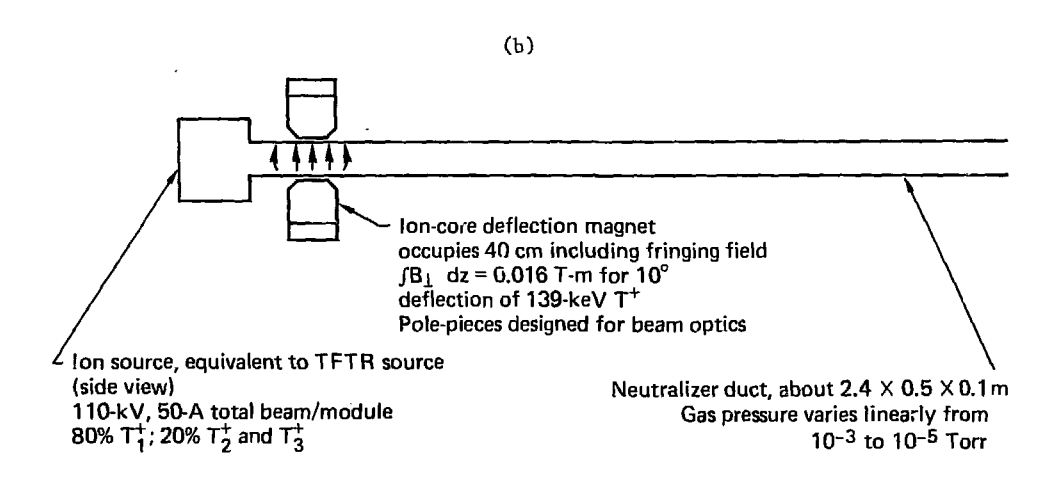Gas pressure varies linearly from
10^{-3} to 10^{-5} Torr

Fig. 5-5. Magnetic deflection of the primary beam before neutralization:
(a) plan view, showing products of T_1^+ separated from
products of T_2^+ and T_3^+ by a 10-degree magnetic deflection; and
(b) side view, showing a compact iron-core deflection magnet at
the high-pressure end of the neutralizer duct.

To attain a neutralization fraction 90% of the equilibrium fraction, the length of the neutralizer after the deflection magnet will be ~2 m for both the HEPB and the LEPB. This results in 54% neutralization of the HEPB and 82% neutralization of the MEPB.

Reactor Fueling

In the example of Table 5-2, all the neutral pump beams are converted to ions and injected into the central cell as reactor fuel except for the fraction that penetrates through the plasma without ionization or charge exchange. The slow ions produced by the gas pump will not enter the central cell because they are born without kinetic energy outside the dense plasma and will follow flux lines to a collector. The reactor fuel injected by each beam is I^0/F_2, shown by Table 5-3 to be a total of 1,440 A. It will be convenient to adjust conditions so that this injected current fulfills 100% of the reactor fueling requirements. In the next step of the reactor design, the parameters f_D, f_{LEPB}, f_{MEPB}, f_{HEPB}, the gas pump baffles, and perhaps the length of the central cell will be adjusted to equalize the fueling requirement and the injected pump beam current. This equalization will be deferred until the next design stage when we will have a fully consistent design.

The injected currents of D^+ and T^+ should be proportional to the rate of Coulomb scattering to equalize the densities of D^+ and T^+ in the central-cell plasma. The Coulomb scattering rate is inversely proportional to the ion mass, since both species have the same temperature and charge. We have specified that the HEPB and most of the MEPB be 100% T^0 to take advantage of the larger charge-exchange cross section. Table 5-3 shows how the injected currents can be adjusted to fulfill these requirements.

142

TABLE 5-3. Reactor fueling by charge-exchange pump beams.

	GP	LEPB	MEPB	HEPB	Total
Current injected into central cell, I^0/F_2 (A)	0	697	609	134	1,440
T^+ injected (A)	0	0	513	134	647
D^+ injected (A)	0	697	96	0	793

TABLE 5-4. Cold-electron load (both ends).

	GP	LEPB	MEPB	HEPB	Total
$(F_1F_2F_3)^{-1}$ calculated from Table 5-2	0.699	0.571	0.350	0.160	
$(1 - F_2^{-1})$ calculated from Table 5-2	0	0	0.048	0.138	
$I_{ionization}$ (Eq. 5-18) (A)	185	299	385	110	979
Electron current into plug (A)	0	299	385	110	794
Potential difference (kV)	112	112	67	0	
Cold-electron power load,[a] (MW)	0	33.5	25.8	0	59.3

[a]To be supplied by electron cyclotron resonant heating (ECRH).

Cold-Electron Load

The cold electrons produced by ionization of injected neutrals will be a load on the electron energy balance. If the cold electrons enter the plug plasma, they will create a load for electron cyclotron resonant heating (ECRH). If they enter the central cell, they will be heated indirectly by collisions with alpha particles.

The rate of electron production ($I_{ionization}$) by ionization of each of the neutral beams I^0 can be computed by the factors F_1, F_2, F_3. The injected neutral beam can be divided into three fractions: charge-exchange pumping, ionization, or penetration through the plasma:

$$I^0 = I_{pumping} + I_{ionization} + I_{penetration} \quad ,$$

where

$$I_{pumping} = I^0/F_1 F_2 F_3 \quad ,$$

and

$$I_{penetration} = I^0 (1 - F_2^{-1}) \quad . \tag{5-18}$$

Consequently,

$$I_{ionization} = I^0 [1 - (F_1 F_2 F_3)^{-1} - (1 - F_2^{-1})] \quad .$$

The results of this computation are shown in Table 5-4, with the additional assumption that electrons produced by the gas pump can be baffled from the plug plasma.

Electrons produced by the HEPB at the bottom of the potential well have potential energy of $\phi_b + \phi_c$ relative to the plug plasma and require no further heating. Electrons produced by the MEPB have potential energy of only $0.4 \phi_b + \phi_c$, while electrons produced by the LEPB have potential energy of ϕ_c. The ECRH load is determined by the need to heat the cold electrons to a total energy of $\phi_b + \phi_c$. This computation is also shown in Table 5-4.

Charged Beam Power

In Table 5-5, we compute the charged beam power and the total input power required for the charge-exchange beams. This computation is based on the neutral-beam power $E_B I^0$ for each pump beam as computed in Table 5-2. The correction factors F_5, F_6, and F_7 are required to account for the beam fractions lost because of the neutralization, the nonuseable molecular ions in the primary beam, and the premature charge exchange in the deflection magnet. These losses have been discussed in other sections of this chapter.

The result is that for this example the total input power required for the pump beams is 118.9 MWe, of which 56.1 MW is collected by beam dumps in the injectors and is available for thermal or electrical energy recovery. If the efficiency of thermal energy recovery is 30%, the net input power is 101.2 MWe. A further saving of about 10 MW is possible by using beam direct recovery where this is practical rather than thermal energy recovery. Beam direct recovery at 70% efficiency has been shown to be practical in experiments at LLL/LBL, ORNL, and at Fontenay-aux-Roses under conditions similar to those of the MEPB and HEPB.

TABLE 5-5. Charged beam power requirement.

	GP	LEPB	MEPB	HEPB	Total
Neutralization fraction, F_5	1.0	0.88	0.82	0.54	
Fraction in usable specie, F_6	1.0	1.0	0.9	0.9	
Fraction lost in deflection, F_7	0	0	0.18	0.18	
$I^+ = I^0/F_5 F_6 (1-F_7)$	--	or 792 A D^+ 396 A D_2^+	1,056	391	1,843
Charged beam power, $I^+ E_B$ (MWe)	0	7.9	52.8	54.5	115.2
Arc and filament power, 2 keV/ion extracted (MWe)	0	0.8	2.1	0.8	3.7
Total pump beam input power (MWe)	0	8.7	54.9	55.3	118.9
Number of neutral-beam modules required, both ends, based on $I^+ = 60$ A/module	0	6	18	8	32
Ion beam power available for energy recovery in the injector, (MWt)	0	0.84	20.8	34.5	56.1
Net pump beam input power after thermal energy recovery at 30% efficiency (MWe)	0	8.4	48.6	44.2	101.2
Beam power available for direct conversion, full-energy charged beam only, $I^0/F_5 - I^0$ (MWe)	0	0	7.0	18.5	26.5
Net pump beam input power after beam direct conversion at 70% and thermal conversion at 30% efficiency (MWe)	0	8.4	45.9	37.5	91.8

REFERENCES

5-1.   J. Kesner, Passive Generation of Ambipolar Potential Barriers in a
       Tandem Mirror, University of Wisconsin, Rept. UWFDM-303; to be published
       in Comments on Plasma Physics and Controlled Fusion.

5-2.   A. C. Riviere, "Penetration of Fast Hydrogen Atoms into a Fusion Reactor
       Plasma", Nucl. Fusion 11, 363 (1971).

5-3.   S. L. Milora and C. A. Foster, "A Revised Neutral Gas Shielding Model
       for Pellet-Plasma Interactions", IEEE Tran. Plasma Sci., PS-6, 578
       (1978).

5-4.   C. F. Barnett, J. A. Ray, E. Ricci, and M. I. Wilker, Atomic Data for
       Controlled Fusion Research, Oak Ridge National Laboratory, Rept.
       ORNL-5206, Vol. I, p. A.6.2 (1977).

CHAPTER 6.   ELECTRON CYCLOTRON RESONANT HEATING

G. W. Hamilton, B. Arfin

INTRODUCTION

Some means of heating the electrons up to 200 keV in the plug is re-
quired to increase the ambipolar potential confining the central cell ions.
The available plasma heating techniques are neutral-beam injection, electron
beam heating, and several types of radio frequency (rf) heating.[6-1] Our
design studies show that the thermal barrier greatly reduces the heating re-
quirements because the barrier makes it possible to heat the plug plasma with-
out also heating the large central cell.

Neutral-beam requirements are significantly reduced by rf heating, which
reduces the electron drag. In this design the 400-keV neutral beams are re-
quired only to provide the fast ions required for plug confinement. Plug
electrons are heated primarily by rf. We feel that not enough information is
available on the absorption of electron beams in the end-plug plasma for a
reactor design.

Four types of rf heating are available for consideration:

- Alfven wave heating   1-10 MHz

- Ion cyclotron resonant heating (ICRH)   50-100 MHz

- Lower hybrid resonant heating (LHRH)   1-5 GHz

- Electron cyclotron resonant heating (ECRH)   30-150 GHz

In general, the cost per watt increases as a weak function of fre-
quency.[6-2] However, we prefer ECRH for this application for several reasons:

- ECRH transfers the rf power to the electrons; such a transfer is our
  objective.

- More experimental data are available for ECRH[6-3] than for the
  other types of rf heating.

- ECRH power can be transmitted by simple waveguides, requiring no special antenna systems if polarization is not important.
- High-power oscillators (gyrotrons) in the ECRH frequency range have recently become available; this development makes it possible to extrapolate the performance of existing rf systems to the levels required by TMR without the need for totally new inventions.

CHOICE OF FREQUENCY AND RESONANT MAGNETIC FIELD

Efficient transfer of rf power to a plasma normally requires coupling with one of the fundamental plasma resonances. In ECRH the resonant frequency is the fundamental or a harmonic of the electron cyclotron frequency; i.e.,

$$f = f_{ce} \text{ or } 2f_{ce} \tag{6-1}$$

where

$$f_{ce} = eB/2\pi \, m_e = 28B \, [f_{ce} \text{ in GHz, B in Teslas}].$$

However, the resonant condition must occur where the plasma is accessible to the injected rf power. This requires that the microwave frequency be higher than the electron plasma frequency to avoid reflections from the plasma cutoff; i.e.,

$$f > f_{pe}$$

where

$$f_{pe} = (1/2\pi) \, (n_e e^2/m_e \varepsilon_0)^{1/2} = 8,976 \, n_e^{1/2} \, [f_{pe} \text{ in Hz}, \, n_e \text{ in cm}^{-3}]. \tag{6-2}$$

Fortunately, Conditions (6-1) and (6-2) are mutually compatible in the TMR plugs, where the maximum density is $n_e = 3 \times 10^{13} \, \text{cm}^{-3}$. Therefore, $f_{pe} \leq 49$ GHz and the Conditions (6-1) and (6-2) may be satisfied if B is

larger than 1.7 T. These requirements may be satisfied either in the plug
itself or in the transition region between the plug and the thermal barrier.
The electrons in the transition region are electrostatically trapped by the
positive plug potential and belong to the same population as the plug elec-
trons. The transition region is convenient for installation of wave guides
because space is available between the magnet conductors.

Some other practical considerations affecting the choice of frequency
are the magnetic field required for other reasons and the state-of-the-art of
high-frequency gyrotrons. In order to heat the transition region near the
plug and to avoid heating the central cell electrons, we will design for
$B > 2$ T and $f_{ce} > 56$ MHz. To avoid a requirement for gyrotron frequencies
higher than 100 MHz we will use $B < 3.6$ T for ECRH. These conditions can be
satisfied in the transition region in the following range:

Range of conditions for ECRH in the transition region:

$$2 < B < 3.6 \text{ T} \qquad\qquad n_e = 2.2 \times 10^{13} \text{ cm}^{-3}$$

$$56 < f_{ce} < 100 \text{ GHz} \qquad\qquad f_{pe} = 42 \text{ GHz}$$

MICROWAVE POLARIZATION AND ABSORPTION

Conditions must be selected such that the microwaves injected into the
plasma will be strongly absorbed either in a single transit through the re-
sonant zone or by repeated transits within a cavity with reflecting boun-
daries. In TMR it is not possible to enclose the transition plasma completely
within a cavity. However, we can show that the microwaves will be almost 100%
absorbed by the plasma electrons in a single pass.

If we use circular waveguides for microwave injection, approximately 50%
of the injected power will be in the ordinary mode for which the plane-
polarized rf electric field is parallel to the B field; and 50% of the power

will be in the extraordinary mode for which the rf electric field is perpendicular to the B field. The extraordinary mode is absorbed much more strongly than the ordinary mode because the electrons are less free to move with the rf electric field. However, because of the high density and temperature of the TMR electrons, even the ordinary mode will be totally absorbed in a single transit. This condition can be seen from Porkolab's absorption theory.[6-3] The absorption coefficient Γ_0 is defined as $T = \exp(-\Gamma_0)$ where T is the transmitted fraction. Porkolab's results for the ordinary mode are:

$$\Gamma_0 = 2\pi \, L_B(\omega/c) \, (T_e/m_e c^2) \, Q_0$$

$$= 2.56 \times 10^{-6} \, L_B(cm) \, f(GHz) \, T_e(eV) \, Q_0 \quad ,$$

where

$$Q_0 = \frac{1}{4} \frac{\alpha^2 (1 - \alpha^2)^{1/2}}{1 + N_z^2 \, (1 - \alpha^2)} \quad ,$$

$$\alpha^2 = f_{pe}^2 / f^2 < 1 \quad ,$$

$$N_z = ck_z/\omega_0 << 1 \text{ for } \underset{\sim}{k} \perp \underset{\sim}{B} \quad ,$$

and

$$L_B = \left| B(dB/dx) \right|^{-1} \quad . \tag{6-3}$$

The component of the index of refraction along the magnetic field, N_z, is small if $\underset{\sim}{k}$ is perpendicular to $\underset{\sim}{B}$. N_z does not strongly affect Q_0 even if N_z is not small. Also, L_B, the scale length of the magnetic field gradient at the resonant layer, is 100 to 500 cm in the TMR transition region.

In respect to absorption of microwaves, the worst condition will be at the time of startup when the plasma is sustained only by the injected neutral

beams. The absorption parameters during startup and during TMR operation are shown in Table 6-1.

TABLE 6-1. ECRH absorption parameters in the transition plasma.

	Startup	Operation
n_e, cm^{-3}	0.5×10^{13}	2.2×10^{13}
T_e, keV	10	200
f_{pe}, GHz	20	42
f = 56 to 100 GHz, depending only upon B.		
$\alpha = f_{pe}/f$	0.2 to 0.36	0.42 to 0.75
Q_0	0.01 to 0.05	0.05 to 0.095
Minimum value of Γ_0 if L_B = 200 cm	5.12	25.6
$T = \exp(-\Gamma_0)$, maximum	6×10^{-3}	10^{-11}

This computation indicates that absorption in a single transit will be no problem in TMR even under startup conditions. A mixture of wave modes and polarizations can be injected with efficient absorption. This conclusion is supported by reports on recent experiments in ECRH.[6-4]

ECRH POWER REQUIREMENTS

There are two categories of ECRH power requirements:

1. The largest portion of ECRH power is needed to heat the cold electrons produced by ionization of the charge-exchange beams used to pump the trapped ions out of the thermal barriers. In Table 5-4 of Chapter 5 this is computed as 30 MW for each thermal barrier.

2. The second requirement for ECRH heating is the maintenance of the
200-keV electron temperature in the plugs and transition region. This re-
quirement is computed as 9 MW for each end of TMR, based upon the power trans-
fer from the hot plug electrons to the cooler center cell electrons and upon
the power loss by synchrotron radiation.

The total requirement for ECRH power is therefore 39 MW at each end
of TMR. This requirement represents an increase over existing technology that
is surely attainable during the next two decades.

WAVEGUIDE LIMITATIONS

Figure 1-4 is a layout indicating an assembly of waveguides delivering
ECRH power to the transition region of TMR. Each waveguide has a diameter
equal to 20 to 80 wavelengths of the radiation at frequencies in the range
from 56 to 100 GHz. In the present state-of-the-art the capacity of each
waveguide is limited by the power absorbed by the windows, which consist of
two layers of dielectric cooled by a liquid fluorocarbon flowing between the
layers.

It is necessary to make a design decision of whether to design within
the limitations of rf windows or to design the waveguides to operate under
vacuum without windows but with differential pumping to maintain the high
vacuum (10^{-8} Torr) required for gyrotron operation. It appears that both
approaches are feasible, but it is difficult to predict at this time which
approach is better. In Table 6-2 we present the waveguide parameters suitable
for operation of the ECRH system both with and without windows. Both examples
appear to be feasible with moderate improvements of existing technology.

TABLE 6-2. Two examples of ECRH parameters for TMR.

	With rf windows	Without windows
Total ECRH power to each end, MW	39	39
Power density in waveguides, kW/cm^2	2	10
Gyrotron power output, each, MW	1	2
Number of gyrotrons required	39	20
Waveguide diameter, cm	25	16
Overall efficiency, %	60	60
Gyrotron input power, MW total	60	60
, MW each	1.7	3.3
Gyrotron electron beam, kV	83	83
, A	20	40

Several factors must be considered in the decision whether to use wave-
guide windows. A window at the tube is an asset for two reasons: (1) to en-
able the manufacturer to test the tube before shipment; and (2) to protect the
tube from damage when the reactor vacuum is vented.

Windows would be needed at both ends of the waveguide if the waveguide
were pressurized to avoid rf breakdowns. Such breakdowns are expected if the
waveguide under low vacuum must penetrate the fringing field of TMR in a
condition such that $f = f_{ce}$. However, this problem can be avoided by other
means—by evacuating the waveguide to high vacuum or by avoiding the con-
dition $f = f_{ce}$ within the waveguide. Injection of rf into the non-minimum-B
transition region is convenient in this respect because there is only one
radial position in a non-minimum-B field where $f = f_{ce}$, while there are two
such positions in a minimum-B field.

It may be difficult to shield an rf window near a reactor from neutrons and other types of bombardment. The window location must be protected by neutron shielding and by a miter-bend so the window is not directly exposed to radiation and particles emitted by the reactor plasma.

If the rf window is eliminated the complications involved are a differen- tial pumping system to maintain a vacuum at 10^{-8} Torr and a gate valve that may be closed to isolate the gyrotron from the waveguide. If the differential pumping system is cryogenic, it must be somehow protected from heating by stray rf. These complications do not seem impossible to solve.

In the Appendix to this chapter a computation is shown to demonstrate that the average microwave power density specified by this design is at least one order of magnitude less than the ultimate power density limitation imposed by rf breakdown.

GYROTRON RADIO FREQUENCY SOURCES

The recent development of gyrotron oscillators with continuous outputs up to 200 kW at 28 GHz has improved the feasibility of ECRH at the power levels required for fusion reactors. The gyrotron oscillator converts power from an electron beam to rf oscillations by passing the beam through a resonant cavity in a magnetic field tuned such that the electron cyclotron frequency resonates with one of the cavity frequencies.[6-5] The cavity dimensions may be much larger than the wavelength if high mode numbers are used for the cavity resonance. The relatively large cavity dimensions permit high output powers before the limitations associated with high power densities become critical.

A pulsed gyrotron has been reported to deliver 1.1 MW at 100 GHz for 100 μs.[6-6] This performance would fulfill the TMR requirements if the pulse length and efficiency were improved. Efficiencies of 30 to 45% have been measured in other installations; these can probably be improved to the 60% overall efficiency assumed in Table 6-2.

We expect the capital cost of a large ECRH system to be about \$1.00/W delivered to the plasma. This is a rate competitive with the capital costs of neutral-beam systems. This estimate is based on comparisons of the ECRH components with neutral-beam components and the components of other large power systems. Costs of existing gyrotrons are not relevant to gyrotron costs for a reactor because of the development expenses that will not apply to a reactor.

APPENDIX. CALCULATION OF MAXIMUM POWER THAT CAN BE CARRIED IN A WAVEGUIDE

The maximum power density that can be transmitted along a circular wave-guide will be found as a function of the maximum allowable peak fields. The general formula will be derived for the TE_{on} modes and then the power in the TE_{01} and TE_{02} modes will be found for a peak field of 29 kV/cm.

The fields for the TE_{on} modes can be written as:

$$H_z = H_0 \, J_0(kr) \, e^{j(\omega t - \beta z)} \quad , \tag{6A-1}$$

$$H_r = \frac{jBH_0}{k} \, J_1(kr) \, e^{j(\omega t - \beta z)} \quad , \tag{6A-2}$$

$$E = \frac{j\omega\mu H_0}{k} \, J_1(kr) \, e^{j(\omega t - \beta z)} \quad , \tag{6A-3}$$

where:

$$k = \frac{2\pi}{\lambda_c} = p/b \quad ,$$

$$\beta^2 = \omega^2 \mu\epsilon - k^2 \quad ,$$

$$p = 3.82, \ 7.016 \text{ for } TE_{01}, \ TE_{02} \quad ,$$

λ is the free space wavelength ,

b is the guide radius in cm .

The power transmitted can be found by use of Poynting's vector:

$$P_z = \frac{1}{2} \text{ Real} \int_{\theta=0}^{\vartheta=2\pi} \int_{r=0}^{r=b} E_0 \, H_r^* \, r \, d\theta \, dr \quad . \tag{6A-4}$$

This can be shown to be

$$\frac{P_z}{\pi b^2} = 1.326 \times 10^{-3} \frac{\lambda}{\lambda_g} \frac{J_0^2(kb)}{J_1^2(kr)_{max}} E_0^2 \text{ W/cm}^2 \qquad (6A-5)$$

where

λ_g is the guide wavelength,

E_0 is the maximum field in V/cm .

The maximum value of the rf electric field limited by breakdown in air has been measured as E_0 = 2.9 × 10^4 V/cm.[6A-1] In vacuum or in pressurized gas E_0 would be more than this. The ratio λ/λ_g is almost unity for an over-size waveguide. The Bessel functions $J_0(kb)$ and $J_1(kr)$ depend upon the mode. The calculations for the modes TE_{01} and TE_{02} are shown in Table 6-1.

TABLE 6A-1. Calculation of average power density in a circular waveguide limited by rf breakdown at E_0 = 2.9 × 10^4 V/cm.

Calculation	Mode TE_{01}	Mode TE_{02}
kb	3.83	7.016
$J_0(kb)$	0.4028	0.3001
$J_1(kr)_{max}$	0.582	0.582
$P_z/\pi b^2$, kW/cm^2	534	297

REFERENCES

6-1.   M. Porkolab, "Review of RF Heating" from <u>Theory of Magnetically Confined</u>
       <u>Plasmas</u>, Proceedings of the Course, International School of Plasma
       Physics, Varenna, Italy (1977), (Pergamon Press, New York, 1979).

6-2.   B. W. Reed, O. N. Bowen, H. M. Hill, J. Q. Lawson, W. G. Newman, and
       A. J. Sivo, <u>Preliminary Report on the Development of RF Auxiliary</u>
       <u>Heating Systems for TERP-1</u>, Princeton Plasma Physics Laboratory,
       Princeton University, Princeton, N.J., PPPL-1410 (1977).

6-3.   M. Porkolab, "Electron Cyclotron Resonance Heating of Tandem Mirrors,"
       Lawrence Livermore Laboratory, Livermore, CA, UCRL-52634 (1978).

6-4.   C. L. Hedrick, R. A. Dandl, J. A. Cobble, R. A. Dory, H. O. Eason,
       E. G. Harris, G. R. Haste, H. Ikegami, E. F. Jaeger, N. H. Lazar,
       D. H. McNeill, D. G. McAlees, D. B. Nelson, L. W. Owen, D. A. Spong, and
       N. A. Uckan, "Transport and Scaling in the Elmo Bumpy Torus (EBT),"
       <u>Physics and Controlled Nuclear Fusion Research 1976, Sixth Conference</u>
       <u>Proceedings, Berchtesgaden, Nuclear Fusion Supplement 1977</u>, Vol. II,
       p. 145 (1977).

6-5.   R. S. Symons and H. R. Jory, "Small-Signal Theory of Gyrotrons and
       Gyroklystons," <u>Proc. Seventh Symposium on the Engineering Problems of</u>
       <u>Fusion Research, Knoxville, TN (1977)</u>, (IEEE, New York, 1977).

6-6.   V. V. Alikaev, V. A. Flyagin, V. I. Khizhnyak, A. G. Luchinin,
       G. S. Nusinovich, V. G. Usov, and S. N. Vlasov, "Gyrotrons for the
       Electron-Cyclotron Plasma Heating in Large Tokamaks," <u>Proc. of Joint</u>
       <u>Varenna-Grenoble International Symposium on Heating in Toroidal Plasmas,</u>
       <u>Grenoble, France (1978)</u>, (French Atomic Energy Commission, Grenoble,
       France, 1978).

6A-1. H. E. M. Barlow, "The Relative Power-Carrying Capacity of High-Frequency
       Waveguides," Proc. IEE (London, Pt. III, Vol. 99, p. 21, 1952).

CHAPTER 7. PLASMA DIRECT CONVERTER

W. L. Barr

INTRODUCTION

The single-stage plasma direct converter (PDC) on only one end of the reactor receives 180 MW of ion power and produces 115 MW of electricity for a net efficiency of 64%. The largest single loss of efficiency is due to the high average energy of the alphas (2.5 MeV) at the PDC. Without them the efficiency would be 77%. The PDC has a single collector stage and two water-cooled grids, and its maximum diameter is ~13 m. The reason it can be so compact is that only an insignificant amount of electron power has to be handled by the PDC. By selectively leaking most fast ions out one end and most hot electrons out the other, the power loading on the PDC grids is greatly reduced. A simple thermal dump at the electron end receives the 160 MW of electrons plus 45 MW of alphas that cannot be selectively leaked to the PDC.

One novel feature of the TMR concept is that the end-loss ions can be preferentially lost out one end and the electrons preferentially lost out the other end. This condition is accomplished by lowering the potential in one plug slightly so that, as the ions that are confined in the central cell scatter in phase space, they escape over the lower potential barrier before they can gain enough energy to pass over the higher one. The electrons are unaffected by the change in one plug potential since they are confined by the combination of the positive potential, ϕ_e, and the magnetic mirror. By holding the entrance grid to the ion collector at a low negative potential and by decreasing the magnetic mirror on the electron end, the central cell electrons can be allowed to leak out one end before they scatter into the loss cone for the ion end.

The great advantage in separating the end-loss electrons from the ions is gained at the ion end. At the PDC, which recovers most of the ion power

electrically, an electron repeller grid (see Fig. 7-1) prevents electrons from reaching the ion collector, which is held at high positive potential. Any electrons flowing out of or produced in the ion end are reflected by the repeller grid and are eventually collected on the entrance grid, which immediately precedes the repeller grid. The entrance grid therefore has to handle the heat generated not only by the small fraction of the ions that are intercepted but also by all of the electrons that go out that end. By causing most of the end-loss electrons to go out the other end, the heat load on the entrance grid is drastically reduced—in this case from over 160 MW to essentially only the intercepted fraction of the 155 MW of ions.
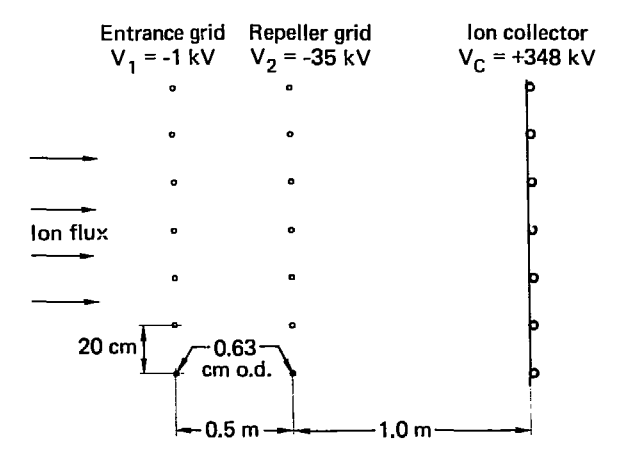

Fig. 7-1. Grids and collector in plasma direct converter.

The low heat load allows a relatively compact PDC for the ion power. The small size of the PDC allows the use of convectively cooled grids, which in turn allow a higher power density than radiative cooling allows. The longest grid element is about 5 m long, and the diameter could be as large as 1 cm. Grids of this size can be water-cooled and can easily handle more than

a 300-W/cm^2 heat load on one side. The flux tube containing the escaping ions must have a cross-sectional area of 65 m^2 to reduce the average power density to about 280 W/cm^2. Because of the circularizing coil the flux tube has a circular cross section, and the field line- radiate out to form an expanding cone. Therefore, the grids and collector of the PDC should each be formed into the curved surface of a spherical segment in order to intercept the ions at nearly normal incidence.

PARTICLE ENERGIES AT PLASMA DIRECT CONVERTER

The current of lost fuel ions going to the PDC is just equal to the total number of fuel ions confined in the central cell at any one time divided by the mean confinement time:

$$I_c = \frac{q \, n_c^2 \, V_c}{(n\tau)_c} \approx 333 \text{ A} \quad .$$

On the average each ion escapes with a mean energy of T_{ic} = 40 keV (i.e., thermal energy in two degrees of freedom), and is then accelerated by the potential difference $\phi_c + \phi_e$ = 355 kV before reaching the entrance grid at the PDC. The average energy is therefore 395 keV, and the minimum is 355 keV. Ions that escape after being confined in a plug also have at least 355 keV of energy at the PDC, but their mean energy is 755 keV. The current of plug ions to the PDC is only

$$I_p = \frac{q \, n_p^2 \, V_p}{(n\tau)_p} \times 2 = 4.8 \text{ A} \quad .$$

The alpha particles that result from the fusion reactions arrive in the end tanks in three different energy groups. Because the effective magnetic mirror ratio seen by the particles in the central cell is only 3.65, 15% (50 MW) of the alphas are born in the loss cone and escape immediately with their full 3.52 MeV of energy. Half of the resulting 28.6 A (electrical) goes out each end and, after acceleration by the difference in potential (ϕ_e = 200 kV), the alphas arrive with 1960 keV per unit of charge. The trapped 85% of the alphas transfer 129 MW to the plasma electrons and 136 MW to the ions. While cooling by transferring energy to the plasma, 22% (42 A) of the alphas scatter into the loss cone and escape with 20 MW of the remaining 25 MW of power. They, too, are accelerated by ϕ_e and arrive half at each end, with a mean energy of 783 keV. The other 63% of the alphas thermalize with the central plasma and eventually diffuse radially, depositing 5 MW on the wall. They are reionized as they leave the wall, and stream out along the outer magnetic field lines as cold ions. The result is that the alphas deliver 44.8 MW out each end, since they are too energetic to be affected by the difference in potential at the two plugs.

Except for the alphas, the total ion energy distribution at the PDC is narrow, with a high minimum of 355 keV per unit of charge. This is an ideal distribution for a single-stage PDC.

SPACINGS IN PLASMA DIRECT CONVERTER

The grid parameters are determined by the spacing d between the collector surface and the surface of the negative grid (see Fig. 7-1). Element-to-element spacing in a grid must be small compared to d to give reasonably smooth surfaces of equipotential near the grid so that the ions are not

deflected by more than about 10°. The spacing d is determined by the current density of the ions. The current density j_i is about:

$$j_i \approx \frac{340 \text{ A}}{65 \text{ m}^2} = 5.2 \text{ A/m}^2 \quad ,$$

if we ignore the alphas since their contribution to space charge is small. At a given current density, the space charge of the ions seriously distorts the applied electric field near the collector if the spacing d is too large. For spacings larger than a maximum value, a virtual anode forms in front of the collector. The location of this virtual anode is the maximum effective spacing, d_{max}, and is given approximately by Child's law for the space charge limit in a plane diode. When solved for d_{max}^2, Child's law states that:

$$d_{max}^2 = \frac{4\varepsilon_0}{9} \sqrt{\frac{2q}{M}} \frac{V^{3/2}}{j_i} \quad ,$$

where $\varepsilon_0 = 8.85 \times 10^{-12}$ F/m, q is the charge, M is the mass of an ion, and V is the voltage difference across the space d_{max}. In this expression it is assumed that the ions all have zero energy at the anode. In the PDC the collector voltage is about 350 kV and only some of the ions are decelerated to near zero energy. The average ion arrives with 40 keV of kinetic energy remaining. For this reason, Child's law gives a slightly smaller value for d_{max} than the true value. Actually, in a PDC there is no serious consequence of exceeding d_{max}. If the spacing is greater than d_{max}, a virtual anode forms at d_{max} as the space charge of the ions increases the potential there until it is essentially equal to anode (i.e., collector) potential. If the potential at the virtual anode were to rise above the collector voltage, some ions would be reflected before reaching the collector. But, the emission of secondary electrons from the collector prevents the space charge potential from rising more than a few volts above that of the collector. The result is

that in a PDC the effective spacing adjusts automatically so that it satisfies Childs's law.

The voltage difference across the spacing d is approximately the difference between the 350-kV collector voltage and the -35-kV grid voltage, or 385 kV. Child's law then gives d_{max} = 1.58 m for an equal mixture of 350-keV tritons and deuterons making up the current density j_i = 5.2 A/m^2. We choose d = 1.0 m and set the spacing between the negative grid and the grounded grid equal to 0.5 m.

The longest grid elements are approximately 5 m long. By using high-strength, high-temperature alloys, such as Ta-10 W or Mo-0.5 Ti (which can stand an internal water pressure of 400 bars), the 280-W/cm^2 heat load could be handled on grid elements less than 2 mm in outer diameter. Elements of that small size would intercept only about 1% of the ions. But, the manifolds to supply the high pressure water would intercept much more. Also, there is a danger from the possible failure of such a high pressure system.

For the present study we consider larger diameter elements that can handle the 280 W/cm^2 on one side with much lower water pressure and temperature. The elements considered are tubes of 316 stainless steel with a 0.63-cm outside diameter and 1-mm-thick walls. An input water pressure of 20 bars and an outlet pressure of 5 bars allow a temperature rise in the water of 120°C in a 5-m-long tube. The maximum tube wall outer temperature is 275°C.

The spacing "a" between tubes in a grid should be small compared with d = 1000 mm, but much larger than the 6.3-mm-diam of the tubes. We choose a = 200 mm, making the grid 3.2% opaque to the ions. The water manifolds and the support structure add to this opacity.

CAPACITIVELY STORED ENERGY

In designing the support structure, the total capacitively stored elec-
trical energy must be considered. The stored energy that can be released in a
spark must be kept below about 10 J to prevent damage to the electrodes. To
limit the stored energy available, the PDC must be electrically divided into
sections. The total stored energy E_{st} in the PDC is:

$$E_{st} = \frac{1}{2} CV^2 \quad ,$$

where

$$C = \frac{\epsilon_0 A}{d}$$

$$\epsilon_0 = 8.85 \times 10^{-12} \text{ F/m} \quad .$$

$A = 65 \text{ m}^2$ is the surface area of the PDC, $d = 1.0$ m is the grid-to-collector
spacing, and $V = 385$ kV is the potential difference between grid and col-
lector. The above gives $E_{st} = 43$ J, indicating that the PDC must be divided
into at least five sections. We choose the configuration shown in Fig. 7-2,
which divides it into seven sections and allows for the possibility of higher
power density and higher ion energy near the center.

GRID VOLTAGE

Each section of the PDC is similar to a plane, triode vacuum tube. We
must operate it beyond the cutoff condition to prevent electrons at the en-
trance grid (cathode) from reaching the collector (plate). Spangenburg[7-1]
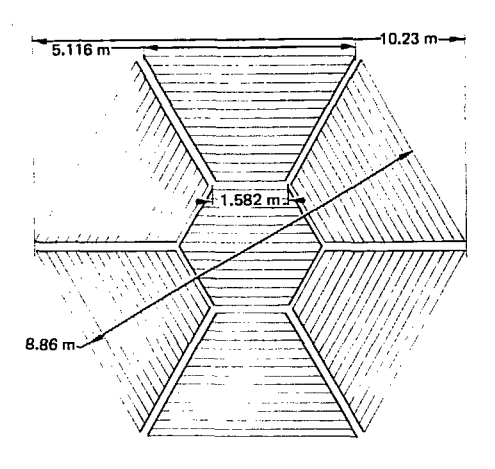
Fig. 7-2. Seven sections of entrance grid.

has analyzed the grid voltage required for cutoff in triodes, and his graph

shows that the grid voltage, V_g, must satisfy:

$$V_g \leq -V_p/13$$

for our geometry ratios. Here, V_p = 350 kV is the collector voltage.

Spangenburg's analysis does not include the space charge of the ions.

The effect of space charge can be approximately allowed for by observing that

in a space-charge limited diode (considering only the negative grid and the

collector now), the electric field at the cathode is just 4/3 times the vacuum

field. We can include this effect by reading Spangenburg's graph at 3/4 of

the actual d value. This gives $V_g \leq -V_p/10$ = -35 kV. We set V_g = -35 kV,

since the PDC is well below its space charge limit.

STRUCTURAL DESIGN

The hexagonal shape of the PDC shown in Fig. 7-2 offers a practical ap-

proximation to the ideal spherical surface. The six sections outside the cen-

tral hexagon are tilted toward the incident beam to receive it at nearly

172

normal incidence. The 6.5-m^2 area of the central section is smaller than

the 11.1 m^2 of each outer section because of the higher power density at the

center and because of the unused outer corners. In the center section the

longest grid tube is 3.16 m as compared to 5.12 m for the longest outer tube.

This difference allows the center section to receive up to twice the power

density that the outer tubes are designed for.

There are 17 tubes in each outer grid section and they vary in length

from 1.58 m to 5.12 m. The center section has 14 tubes with lengths from 1.58

to 3.16 m. It is assumed here that all tubes have the same inner and the same

outer diameters. A more detailed design should adjust the diameters so that

the temperature rise of the water is the same in all tubes. Similarly, the

cantilever supports for the outer sections which also serve as water manifolds

(see Fig. 7-3) could be optimized by varying the inner and outer diameters

along the length. In this way the sag could be limited with a minimum of ex-

ternal area exposed to the ion flux. Here we simply note that the cantilever

supports for the outer sections could be made from 316 stainless steel tubes

with uniform 25-mm o.d. and 1.3-mm wall thickness. The greatest sag would be

0.23 m at the tip of the supports for those outer grid panels that lie in

nearly vertical planes. This greatest sag would occur in the plane of the

grid. The center section is supported from the rear (see Fig. 7-4), and we

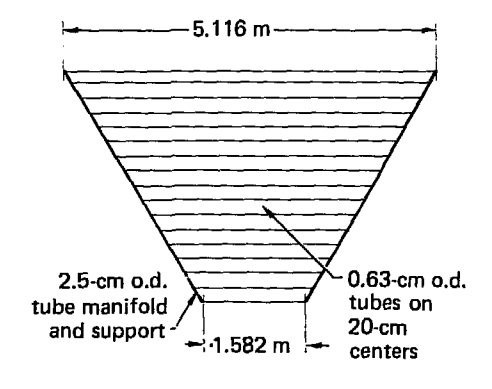assume that the same size tubes can be used there.

Fig. 7-3. Outer section of
entrance grid.

0.63-cm o.d. tubes on 20-cm centers

In

Out

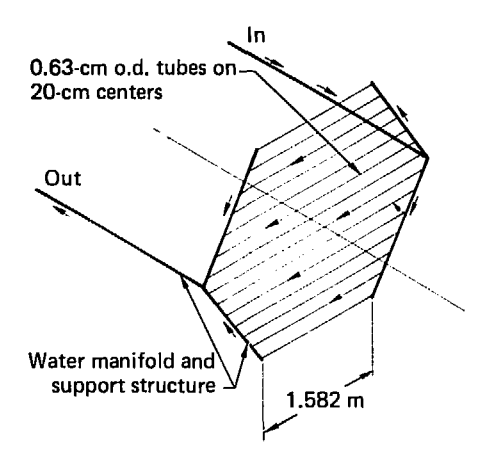Water manifold and support structure

1.582 m

Fig. 7-4. Supports for center section of grid.

There are six outer panels for each grid, and each panel requires two support tubes 3.76 m in length. But only 3.32 m of that length is exposed to the flux of ions. The center panel of each grid requires support tubes on four of the six sides. Each side is 1.58 m long. Therefore, the total length of exposed support tubes in each complete grid is 46.2 m giving an intercepting area of 1.15 m^2. There is a 6.3-mm grid element every 200 mm across the grid, giving an intercepting area of 2.05 m^2 for the elements. The total intercepting area is 3.2 m^2, or 4.9% of the 65 m^2 total. Both grids have identical structures.

The center section of each grid is supported from behind by two 25-mm stainless steel tubes, which also carry the cooling water. High voltage insulators are required where the four tubes pass through the collector surface. The insulators must hold off 350 and 385 kV at the supports for the entrance and the negative grid, respectively. Shielding against sputtering must also be provided at each insulator. Because of the 20-cm spaces between grid elements, no insulation is needed where the supports for the entrance grid pass near the negative grid. Only a negligible fraction of the collector surface area need be lost to the feedthrough insulators. If each insulator

structure has an outer diameter of 15 cm (~50 kV/cm), the total area lost for ion collection is only 0.07 m^2. Figure 1-6 shows a sketch of the structure.

VACUUM REQUIREMENT

The vacuum in the region between the plug and the PDC must be good enough so that only an allowable fraction of the escaping ions undergo charge exchange. Any ion that does capture an electron from a gas molecule will arrive at the PDC as a fast neutral. It will impact the collector with its full ~355 keV of energy and will generate heat but no direct electric power. The cold ion that is produced is trapped by the combination of the magnetic field and the high positive potentials of the plug on one side and the PDC on the other. It will finally diffuse to a magnetic flux tube that intercepts a grid element and will be collected there. Since its energy is low, very little heat is generated, but electrical power is consumed at the negative grid.

It is more serious if the ion suffers charge exchange inside the PDC near the collector where the potential is positive. Then the resulting ion is accelerated and can deposit a significant amount of heat on the grid that collects it.

The cross section for charge exchange of fast D^+ with D_2 molecules is 4×10^{-18} cm^{-2} at 395 keV and has a broad maximum value of 8.6×10^{-16} cm^{-2} between about 4 and 20 keV. Those ions that reach the PDC with only slightly more than the minimum 355 keV are decelerated into that 4- to 20-keV range where the cross section is large. Ions with the average 395 keV or more see a much smaller average cross section. We can, therefore, estimate the vacuum requirement by calculating the pressure at which about 2% of those worst-case (355-keV) ions undergo charge exchange. The fraction, $F_{0,L}$, of those ions

that capture an electron in a charge-exchange collision in going the distance L from the plug to the collector surface is:

$$F_{0,L} = 1 - \exp\left\{ - \int_0^L n_0 \, \sigma_{10} \, dx \right\} \quad ,$$

or approximately

$$F_{0,L} \approx \int_0^L n_0 \, \sigma_{10} \, dx \quad .$$

Here, n_0 is the neutral gas density, σ_{10} is the cross section for electron capture, and both n_0 and σ_{10} may vary with the distance x along the ion path. For those worst-case ions, the last 20 cm before collection dominates the integral so that:

$$F_{0,L} \approx n_0 \, \sigma_{10}(\text{max})(20 \text{ cm}) \quad .$$

For $F_{0,L} \leq 0.02$, we must have $n_0 \leq 1 \times 10^{12} \text{ cm}^{-3}$ giving a pressure $p \leq 3 \times 10^{-5}$ Torr. This is a rough estimate of the vacuum requirement. For a more accurate determination of the allowed neutral density, a proper average of $F_{0,L}$ must be calculated using the ion energy distribution.

The allowed pressure, p, and the gas throughput, Q, then determine the pumping speed, S, that is required. The 340-A input of atomic ions becomes Q = 30 Torr-litres/s of molecular gas. Then:

$$S = \frac{Q}{p} = \frac{30 \text{ Torr-litres/s}}{3 \times 10^{-5} \text{ Torr}} = 1.0 \times 10^6 \text{ litres/s}$$

is the required pumping speed. Cryopumping can be used not only for the hydrogen isotopes, but also for the small amount of He. The He will be pumped by cryotrapping because of the 30-times-greater input of D_2 and T_2 which will act as the sorptive medium. A cryopump with two sets of chevrons has a specific pumping speed of 4.4 litres/s-cm^2 for a mixture of D_2 and T_2 gas at

300 K. Therefore, only 23 m^2 of cryopanels is needed. As compared to the 65-m^2 frontal area of the PDC, the 23 m^2 of cryopanels seems rather modest. The cryopanels can easily be located on the side walls in the PDC tank where they are protected from neutron bombardment. Figure 7-5 indicates their location.
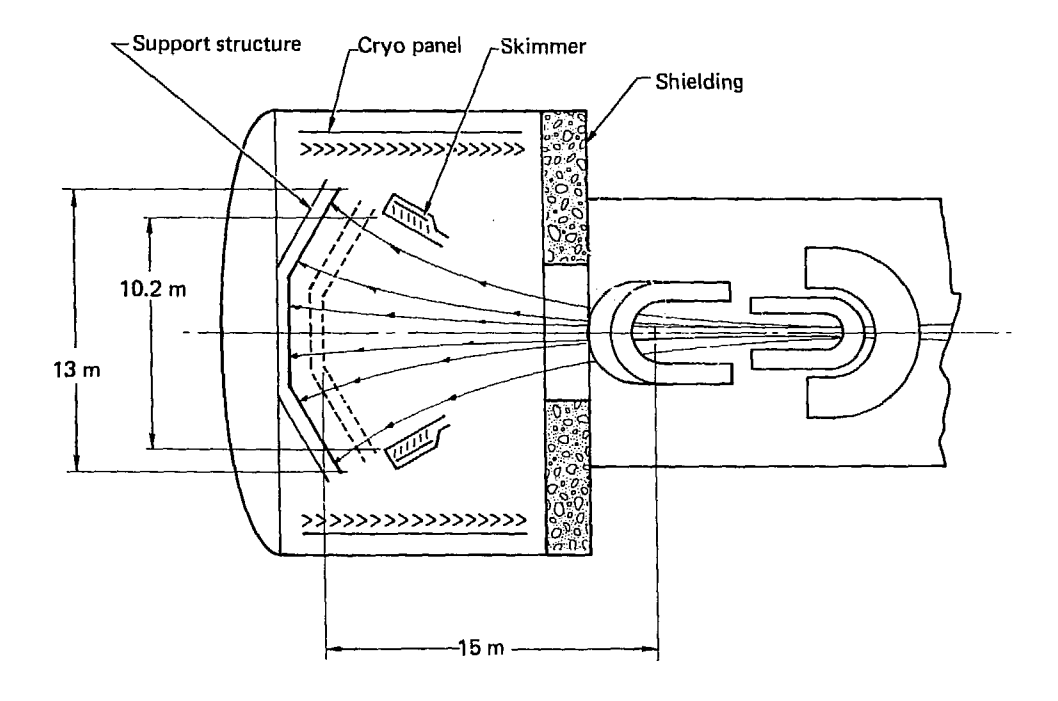

Fig. 7-5. Location of cryopanels and skimmers.

Skimmers near the PDC remove the cold plasma that streams out along magnetic field lines that lead from the outer boundary of the central cell plasma. These skimmers (see Fig. 7-5) direct their gas onto enclosed cyropanels.

The efficiency of the PDC can best be determined by considering the losses. The losses are:

- Electrons. We assume here that all hot electrons are lost out one end and do not affect the PDC at the other end. The cold electrons that neutralize the space charge of the ions give rise to only an insignificant loss.

- Grid interception. The grids together with their supports each intercept 4.9% of the ion flux giving a 9.8% total loss.

- Repeller grid power consumption. The negative grid is held at $V_g = -35$ kV by a power supply that must supply not only the 4.9% of 360 A of ions that it intercepts, but also about three secondary electrons for each ion intercepted. The above amounts to a power loss of about 17 A of ions and 50 A of electrons at 35 kV, or 2.4 MW, which amounts to 1.5% of the incident 159 MW of total ion power.

- Energy spread. The ideal collector potential is 355 kV, the maximum value before reflecting even those ions with the lowest energy. The average ion, including alphas and plug ions, has 482 keV of energy per unit of charge at the PDC and impacts the ideal collector with 127 keV, giving a loss of 26% in directly recovered power.

- Deflection at the grids. Those ions that pass close to a grid element, especially in the negative grid, suffer some deflection. The deflection is small because of the high energy of the ions, and is estimated to be less than $8°$ maximum. After an $8°$ deflection, a minimum-energy (355 keV) ion has only 348 keV of energy in the forward direction. For this reason the collector voltage must be reduced from 355 to 348 kV to prevent the reflection of some ions. This gives a 2% loss of recovered power.

• Residual magnetic field. The strength of the magnetic field at the PDC is less than that in the central cell in inverse proportion to the areas. This gives 0.075 T at the PDC. Since the ions were confined electrostatically and not magnetically, this residual magnetic field does not limit the parallel energy at the PDC, and causes no loss of recovered power.

• Charge exchange. By maintaining the pressure in the PDC vacuum tank below 3×10^{-5} Torr, the loss of fast ions by charge exchange can be made negligible. The power consumed by the collection of the resulting cold ions on the repeller grid is then also negligible.

• Coolant pumping power. Because of the rather large size of the tubes that make up the grids and those that can be used to cool the collector, we assume the pumping power is negligible.

After allowing for all of these various losses, a total of 338 A of ions are collected at 348 kV, giving 115 MW of net electric power output from the PDC after supplying 2.4 MW to the repeller grid, yielding an efficiency of 64%. The largest single loss is that due to the high average energy (~2.5 MeV) of the alphas at the PDC. The efficiency is 77% if the alphas are not included in the calculation.

REFERENCES

7-1. K. R. Spangenburg, <u>Vacuum Tubes</u> (McGraw-Hill Book Co., New York, 1948),

p. 125 ff.

CHAPTER 8. CENTRAL CELL

W. S. Neef, Jr.

The heart of any fusion power plant is the energy conversion blanket which absorbs thermonuclear neutrons (converting the neutron kinetic energy to temperature rise in a circulating coolant), and breeds tritium as future fuel. The TMR blanket and shield assembly has the simple geometry of a straight cylindrical annulus.

Our first attempt at a TMR blanket design[8-1] used wedge-shaped pressure-tight submodules arranged in a ring. They contained quasi-static lithium in canisters that were cooled by helium at a pressure of 60 atm and a maximum coolant temperature of $550^{\circ}C$. The shape of these modules and our desire to avoid cold-welding by contact led us to a rigid pressure container of nonideal shape and a large structural fraction (about 17%). Sufficient tritium breeding was achieved but the design proved expensive. Contributing to the high cost of the central cell was a low solenoid current density (1200 A/cm^2), which we are now confident can be tripled with present niobium-titanium superconductor. The MFTF yin-yang coil is designed for 2980 A/cm^2 with a 7.5-T field at the conductor. Our conductor field strength will be about half that value.

Improvements in tandem mirror physics leading to higher reactor Q have been under development. Preliminary results indicate that best reactor eco- nomics will probably be at a first-wall neutron power loading between 2 and 4 MW $\cdot$ m^{-2}. We have proceeded to develop a new blanket and shield concept for the central cell quite independent of the end-plug changes, knowing that we could deal with the transition zone near each plug without basically changing a new central-cell design approach.

In order to reduce reactor cost and to improve maintainability we have established the following set of design goals for this iteration of the TMR design. They are:

- Simple design; easily built parts

- Rugged, reliable, pretested components

- Simple building for shielding, containment, and support

- Operation by a standard: If it doesn't require replacement, don't move it

- Remote servicing by simple motions with simple tools

- Inexpensive construction, operation, and maintenance

We have achieved these goals by redesign of the central cell.

CYLINDRICAL PODS

It is well known that a cylinder is a much more material-efficient pressure vessel than our previous wedge. Long cylinders were studied (some as long as the entire central cell) but the problem of replacement ended that investigation. Cylinders pointing toward the plasma centerline have been proposed,[8-2] but in that case each was removed from inside the vacuum vessel (i.e., toward the plasma). We wished to minimize plumbing disconnects both for first-wall replacement and for flaw correction. Further, we wished to propose a reactor offering two modes of blanket change: (1) remove large segments for first-wall change; and (2) remove only the offending blanket submodule in the event of some malfunction, to effect the quickest possible repair.

Our new design employs annular rows of short tubes. Four and five rows were considered, the latter to be used if the tritium breeding material is liquid lithium. Four rows are sufficient if lithium oxide is the breeder. To

achieve the highest breeding material content the tubes (called "pods" in this design) change in diameter approximately in proportion to distance from the reactor centerline. Figure 8-1 shows an arrangement of four rows of pods. The pods are mounted permanently to two different gas distributor housings. (Figs. 8-2 and 8-3). The two shapes are necessary to permit withdrawal of the pod-modules radially inward from their mounting location on the shield. If one of the smaller pods must be repaired it will be necessary to remove the two neighboring large pods to gain access to the small one. This method of removal can be used for correction of a pod malfunction by moving a service-car down the bore of the reactor and extracting and replacing the offending unit. This remote servicing machine will be described in more detail in Central Cell Servicing.
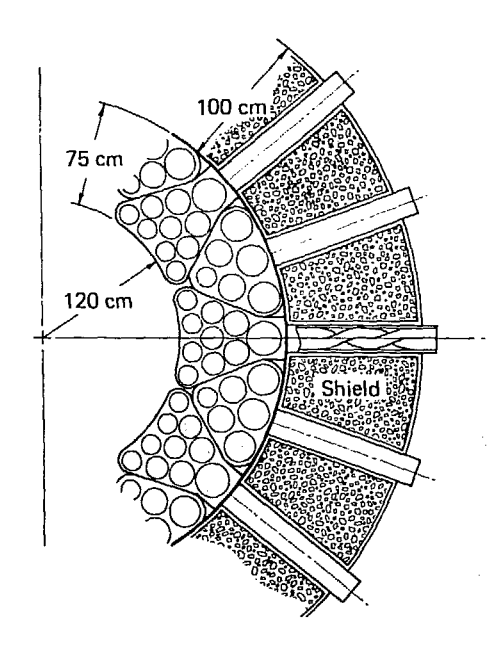

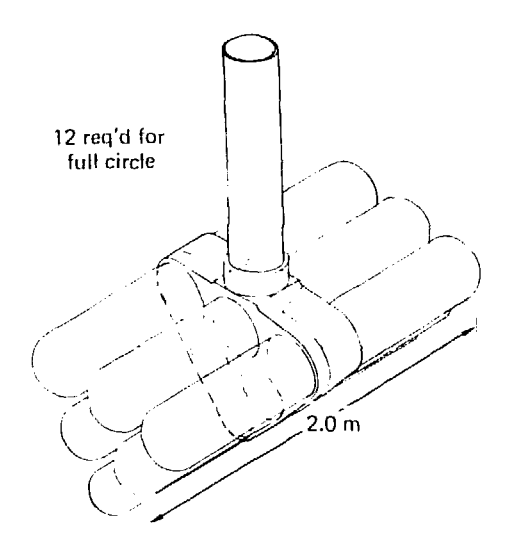Fig. 8-1. Cross section of blanket and shield.

12 req'd for
full circle

Fig. 8-2. Blanket pod cluster—Type S.
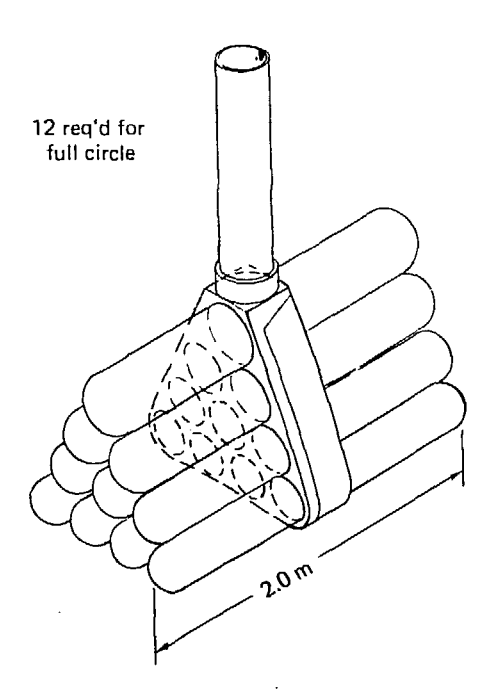
2.0 m

12 req'd for
full circle

Fig. 8-3. Blanket pod cluster—Type T.

2.0 m

186

Each gas-distributor module has a stem that extends through to the back of the shield where it is welded at the time of assembly. Figure 8-4 shows this stem containing gas inlet and exit tubes (twisted to reduce neutron streaming). A bolted cover flange carrying helium coolant tubes provides the gas seal. That flange must be removed to allow access to the aforementioned stem weld. The flange's coolant tubes mate with the twisted gas tubes in the module stem. The seal between those tubes need not be perfect. The flange seal and the tube joints between the cover flange and the supply and return manifolds must be of high-vacuum quality and must be tested using mass spectrometer methods.

Each pod (there are ten in one assembly and six in the other) passes through the gas distributor support. Two metres were chosen as the pod length, which sets the length of a major central cell module at 2 m also. The mass of such a module is approximately 500 tonnes.

The construction features of the pod and its relationship to the gas distributors is shown in Figure 8-5. The canister containing the breeding material, Li_2O in finely divided granules, is sheet stainless steel with a thin coating nearly impervious to tritium. Berylium oxide is one coating possibility. Tritium is removed from the canister by a small purging flow of helium at the same pressure as the main coolant stream. The fraction of maximum theoretical density that is attainable for Li_2O is not known; it most probably lies between 60 and 90%. Our calculations of tritium breeding ratio indicate a range of values from 1.07 at 50% theoretical density to 1.27 at 90%. The more finely divided particles will allow prompt tritium purge and hence lower blanket inventory. Work by JAERI[8-3,8-4] in Japan leads us to conclude that tritium can be extracted easily so long as the particles of Li_2O are small, preferably 10 to 100 μm across.

Coolant in

Coolant out

Coil

Lead-cement shield
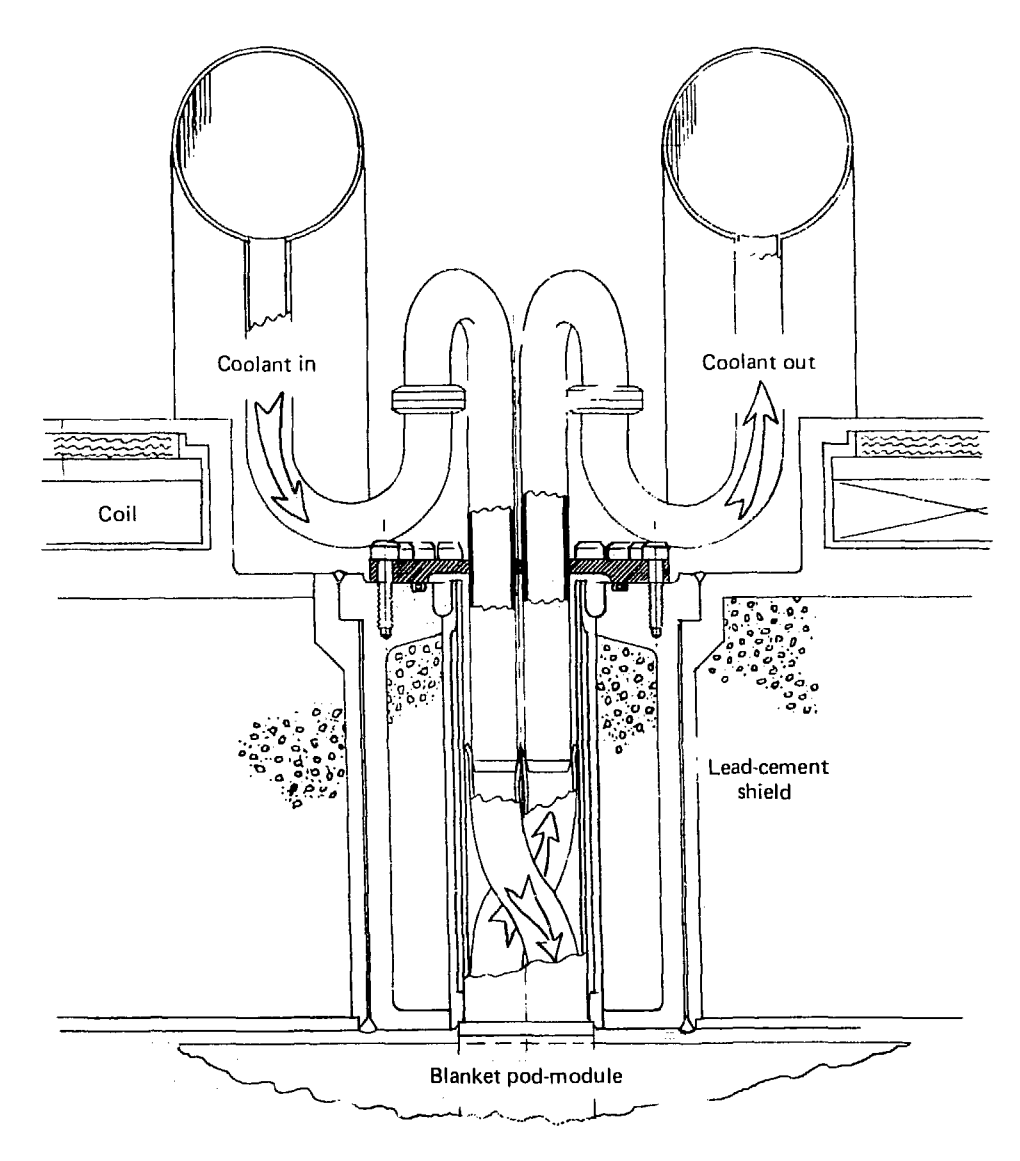
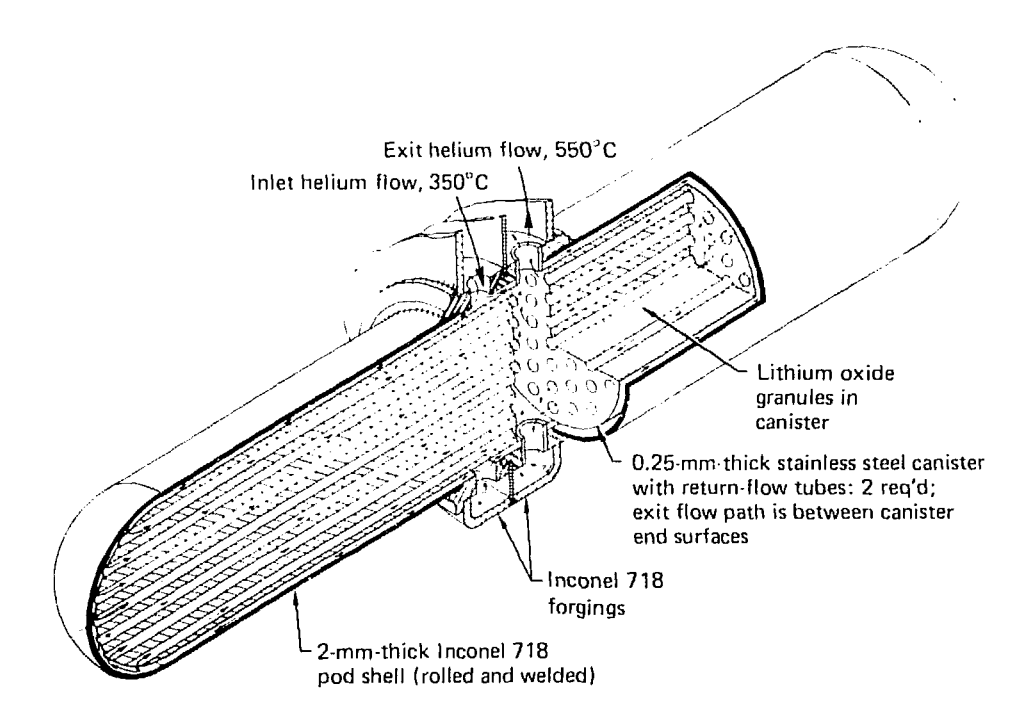**Blanket pod-module**

Fig. 8-4. Module coolant connection.

Fig. 8-5. Blanket pod.

The coolant flow path brings helium first to the pod shell where it flows toward the hemishell end. The outside of the Li_2O canister is cooled simultaneously by that flow stream. Upon reaching the end of the shell the helium returns, entering tube passages running lengthwise through the canister thereby cooling the internal mass of Li_2O. The presence of the tritium-purging helium flow at 60 atm pressure is essential to obtain blanket cooling. The helium serves as the heat transfer medium from the Li_2O particles to the tube walls of the canister. The number and location of these 0.5-cm-diam tubes has only been estimated.

To return the coolant to the gas distributor it is necessary that a collection gap about 4 cm long be provided just adjacent to the midplane of the canister. Helium flows radially outward from this collector plenum through short tubes that also serve to anchor the canister within the pod. To further stabilize the canister position in the flow stream, several fins or corrugations of the canister outer shell will serve to pilot it inside the pod.

It will be noted that the outer shell of the canister of Li_2O is continuous through the gas distributor. There are two reasons: the breeding of tritium requires some lithium in that zone in order to achieve an adequate breeding ratio, and also, structural members are required to limit the bending stress in the gas distributor face-plate. The two halves of the pod shell are joined by threading, which permits a clamping grip on the inlet/exit helium flow divider. Figure 8-6 shows an exploded view of the gas distributor. Once the two pod shells are threaded, the pod collars can be brazed to the gas-distributor housing. This blazing locks the whole gas-distributor assembly since all ten (or in the small module, six) pods will simultaneously be brazed. The heavy pod collars perform the second vital load bearing function. The 60-atm helium pressure cannot be resisted by the walls of the gas distributor housing acting alone because of the large flat-plate area. Additional tension members are required as provided by the threaded pod collars. The central portion of the pod assembly is stressed only axially by the gas pressure. The outboard portions of the shell, 2 mm thick, experience the circumferential stress of any cylindrical pressure vessel plus the tension produced by the pressure on the hemispherical end cap. Inconel 718 has been chosen as the material for this entire structure.
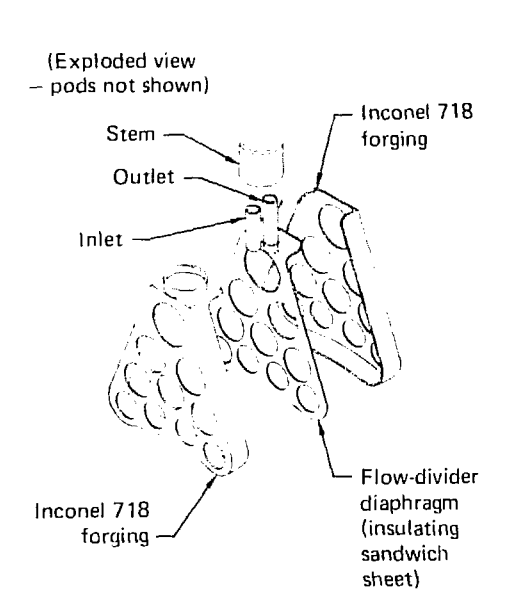
(Exploded view
— pods not shown)

Stem
Outlet
Inlet

Inconel 718
forging

Inconel 718
forging

Flow-divider
diaphragm
(insulating
sandwich
sheet)

Fig. 8-6. Pod-module coolant
flow distributor.

BLANKET AND SHIELD NEUTRONICS*

A Monte Carlo type code, TARTNP, is used extensively at LLL for neu-
tronics calculations. Using that code, we ran both one-dimensional and
three-dimensional problems describing our Li_2O blanket concept. The geome-
try for the three-dimensional calculations is fairly complex. Only a few ap-
proximations were needed to permit reasonably short problem-running time.

Figure 8-7 shows a cross section of the blanket segment analyzed by the
TARTNP three-dimensional runs. Adjacent segments are mirror images of the one
illustrated and are so treated by "reflecting" regions described in the code
input. Note that there are four annular rows of pod shells.

---

*Work performed by D. Hanchar, 1979 summer employee from Massachusetts
Institute of Technology, under the direction of J. D. Lee.

191

Pod shell — Li$_2$O breeding zone

Shield region

Vacuum zone

12 cm   11 cm

11.25 cm

1.60 m radius

9.5 cm   9.5 cm   1.620 m radius

1.40 m radius

8 cm   8 cm   1.425 m radius

1.235 m radius   7 cm   1.260 m radius

7 cm   7 cm   Outlines of coolant distributors
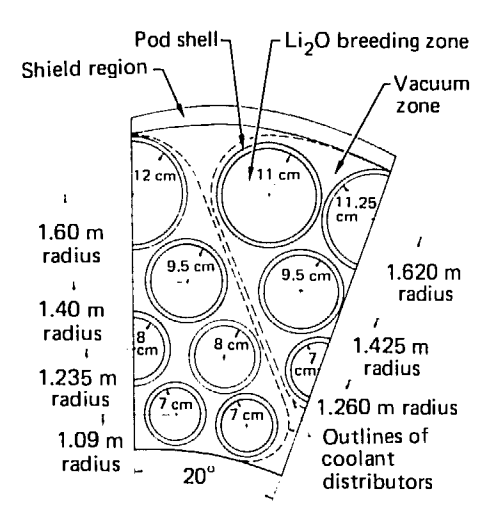
1.09 m radius   20°

Fig. 8-7. End view of neutronics models.

The hemispherical ends on the pod shells were replaced by blunt (flat) cylinder ends. We bracketed the actual geometry with two cases: one, the cylinders extended from −100 to +100 cm giving more than the actual volume of breeding Li$_2$O; and two, the cylinders were truncated at the plane where the radius of the largest hemishell begins. Figure 8-8 compares these two cases. Since Case 2 understates the actual volume of Li$_2$O we are confident that the actual breeding ratio and blanket energy multiplication lie between the results of the two cases.

|← 1.0 m →| |← 1.0 m →|

Steel shell   Shield   Lead concrete

Lead concrete   Breeding pod

Vacuum zone
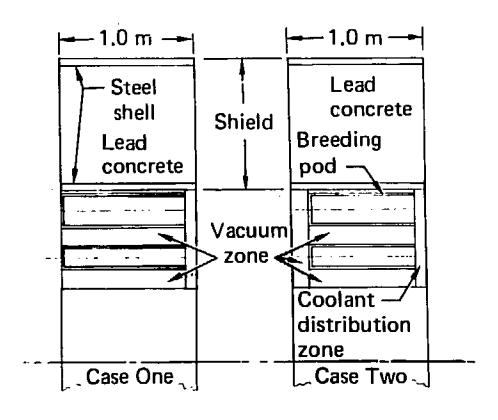
Coolant distribution zone

Case One   Case Two

Fig. 8-8. Side view of neutronics models.

The reason only two pods appear in each part of Figure 8-8 is that the pod-tubes are staggered. A radial plane cut through the blanket bisects the pods of alternate rows and misses pods in the remaining rows.

Both cases were run using various neutron batch sizes. Ten batches were run in all cases. The number of neutrons in each batch was taken as 400, 600 and 800. Results are shown in Table 8-1 for the three assumed batch sizes. Tritium breeding ratios are shown for all three batch sizes. We present the energy multiplier for only the larger batch size.

TABLE 8-1. Blanket neutronics.

| | Tritium breeding ratio Batch size | | | Blanket energy multiplier Batch size |
	400	600	800	800
3D[a] Case 1	1.339	1.241	1.234	1.086
3D Case 2	1.119	1.128	1.136	1.018

[a]Three-dimensional

BLANKET AND SHIELD ASSEMBLY

In considering methods of reactor maintenance, the size and shape of the largest serviceable module is a difficult decision. We set a limit of 500 tonnes on module mass because nuclear components of that mass are routinely installed by conventional cranes. This limit imposed another limit of ~2 m on module length if a full cross-section "slice" of the reactor is to be removed. The solenoid coil shape and the desire to avoid conductor joints impose the geometry limit that any module must contain a full coil—hence, must be a "slice" of the entire central cell assembly.

A result of the above decisions is that the parting planes between neighboring modules must pass between the spherical ends of adjacent pods.

Also in that plane some clearance for removal must be provided. We provide a metal pressurized cushion in that region like a huge steel washer with the same inside diameter and outside diameter as the shield. It is only a few centimetres thick. Depressurizing it allows it to shrink and be slipped from between modules—just clearing the round noses of the pods. During operation, this seal-cushion provides a high impedance vacuum seal between modules. We believe cold-welding can be prevented. First, the contact pressure between the cushion face and the shield is only a few atmospheres. Second, a thin coating of molybdenum or other refractory alloy can be plasma-torch-sprayed onto one of the surfaces to inhibit accidental bonding. No bolted or welded circumferential joints must be broken to remove one of the large modules. Figure 1-7 illustrates the arrangement of the module components. The seal cushion is discussed in more detail in a later section.

Each module has the gas-distributor stems of the pod-submodules on the module's center plane. There are two solenoidal coils on each module, symmetrically disposed from the center plane. The module sits in curved V-blocks surrounding the lower 180° of the module. Those blocks take the unbalanced coil thrust (axial) which is zero or very small at the solenoid center and much larger near the two ends. The top half of the coils must also be supported, and several wedge blocks will be provided, oriented for vertical removal by the crane.

Gas manifolds for the helium coolant are somewhat unique and are shown in Fig. 8-9. To conserve space at the bottom of the machine oné master manifold serves two adjacent modules. Upon reaching the horizontal centerline this manifold bifurcates and becomes two parallel manifolds on opposite sides of the module division plane. These two smaller manifolds lift off the large lower manifolds with the module when it is being removed by the crane. This requires that the pod stem feed pipes for the lower half of the module have

remote-disconnect joints so they may be separated from the lower fixed mani-
fold. Obviously there must also be four manifold couplings to permit division
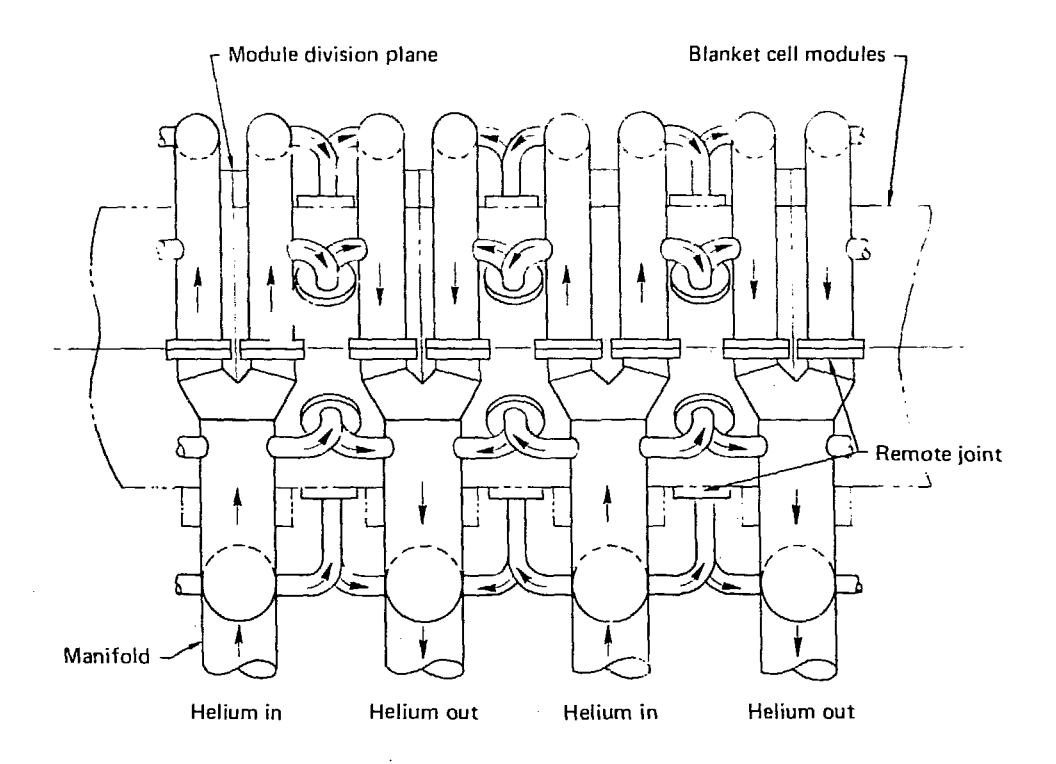of the two smaller manifolds near the horizontal centerline.

Fig. 8-9. Coolant gas manifold system.

There will be twenty helium pipe joints to open by remote tools when a
module is removed: four 20 cm in diameter (on manifolds) and sixteen 6 cm in
diameter (two on each pod stem connection).

Shield

We reduce fabrication costs of the central cell by using a very inexpen-
sive shield and integrating the magnet fabrication with the shield so that
duplication of form and structure can be avoided. The shield is fabricated as
a hollow shell—an inner cylindrical shell, two face-plate "washers," and an
outer shell. The outer shell of the shield cylinder is used as the coil form
for the solenoid magnets. Appropriate layers of insulation would be in-
cluded between the shield outer wall and the superconductor. The dimensions
of the shield for one central cell module are 2.2 m inner radius, 1.0 m,
radial thickness, and 2 m, length. After coil winding and installation, the
hollow shell would then be poured full of lead-concrete. This "concrete" uses
lead shot as the aggregate. A range of sizes will yield a higher packing
factor. A high density matrix material (ρ = 10 g/cm) is used to fill the
voids and complete the lead shield without pouring molten lead. This matrix
materal is proprietary with Chemtree Corp., Central Valley, New York, and is
called "Lead-cement."

Seal Washer

The pressurized-cushion seal* between central cell modules was mentioned
earlier in the section, Blanket and Shield Assembly. It must provide a very
low conductance gas seal between the 10^{-2}-Torr vacuum, which can be readily
achieved in the "trench" surrounding the central cell, and the plasma chamber

---

*Patent applied for by General Atomic Company, San Diego, as a result of
1978-1979 contract work with Lawrence Livermore Laboratory and Pacific
Gas and Electric Company for the Electric Power Research Institute.

pressure which must be in the 10^{-6} to 10^{-7} Torr range. This low conduct-
ance is achieved by flat plate contact over a radial dimension of 1 m (the
shield thickness) with an assumed average gap of 0.03 mm. The conductance of
such a gap is about 0.04 litres/s. With 28 modules (hence 58 sealing sur-
faces) the total gas inflow is 0.02 Torr-litres/s, a very small gas load. A
method of halving that gas flow is to build the cushion as a permanent part of
the shield on one end of each module. This method has the added advantage of
not requiring a separate disassembly operation to remove the seal cushion. A
disadvantage is the reduced module installation clearance.

The cushion seal, whether separable or integrated with the shield, uses
omega-joint expansion elements, which behave similarly to a bellows but are
much more rugged. The price of ruggedness is comparative stiffness. Only
1 cm of clearance for assembly can be obtained by evacuating the cushion to
allow the ambient pressure in the trench to collapse it. Though normally
evacuated, the trench is backfilled to atmospheric pressure with dry air or
inert gas prior to the beginning of a module change-over.

Another concern for the cushion seal is neutron leakage through the gap
between adjacent shield segments. This gap need not be unimpeded radially.
The two faces of the cushion can be contoured on their inner surfaces (in con-
tact with the pressure energizing fluid) to create a labyrinth (see
Figure 8-10). Some neutron leakage is unavoidable because the effective
shield thickness will be reduced in the cushion zone; however, the leaking
neutrons are not aimed at a solenoid coil. The upper half of the machine,
where such leakage has biological significance, can have fitted shield pieces
separately lifted away by the crane before module removal. The lower half of
the leakage goes into the concrete foundation, service gallery hardware, and
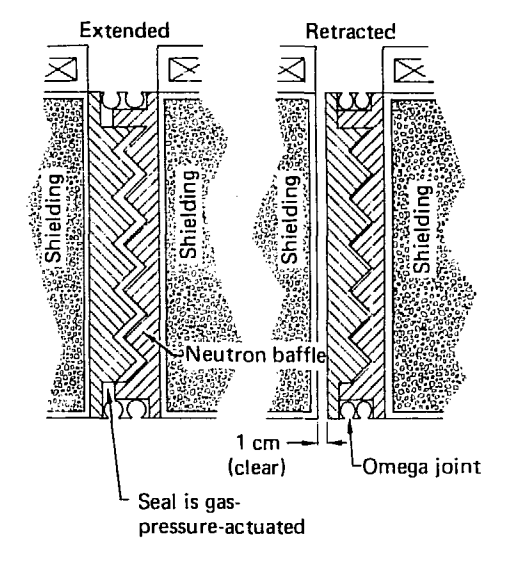the earth.

Fig. 8-10. Module-to-module seal cushion.

CENTRAL CELL SERVICING

Two methods of blanket replacement are available to operators of this TMR: (1) use of the gantry crane to remove a 2-m-long central-cell module containing 18 pod-submodules, or (2) using a service car operating in coopera- tion with disconnect tools, removal of only the pod-submodule which has ex- perienced a failure. The first method should be used for periodic first-wall replacement. The second method applies to unscheduled blanket repairs.

Large Module Replacement

The design feature of this reactor, which permits rapid change of cen- tral cell modules, is the vacuum trench surrounding it. This trench contains locators and supports for each module and a number of hinged covers, one or two of which have to be lifted to yield access to any given module. The vacu- um seals of the trench are all static. The cover seals must be opened and

198

resealed several times in the life of the reactor. The seals can be elasto-
meric since they are in a low radiation environment and are easily replaced.
Along the short edge of the cover the vacuum seal is between the cover and the
building structure. Along the long edge the seal is between adjacent covers.
The corner of the cover presents a difficult topological problem. We suggest
an inflatable hose design of square cross section to provide seal effective-
ness at the corners. Figure 8-11 shows the transition region at the corner.

The procedure for removal of a large module is outlined below:

1. Shut off plasma by stopping all neutral beam injection, de-energize
   magnets.

2. Backfill vacuum trench with dry air or inert gas.

3. Deflate all door seals.

4. Using the traveling crane, remove the desired trench cover(s) and
   store them.

5. Deflate all pressurized seal cushions between modules and evacuate
   the cushion cavity of those seals affecting the desired module.

6. Lift out magnet thrust blocks and store.

7. Disconnect cryogenic services to solenoid coils on desired module.

8. Disconnect instrumentation on module.

9. Disconnect helium purge lines for tritium recovery.

10. Disconnect manifold feeders between fixed lower helium manifold and
    eight lower pod-module subassemblies (sixteen remotely operated
    couplings).

11. Disconnect four remotely operated couplings that attach the upper
    helium manifolds to the fixed lower manifolds.

12. Attach the crane hoist to the module and lift the module assembly
    out of the trench; translate the module to a waiting transporter in
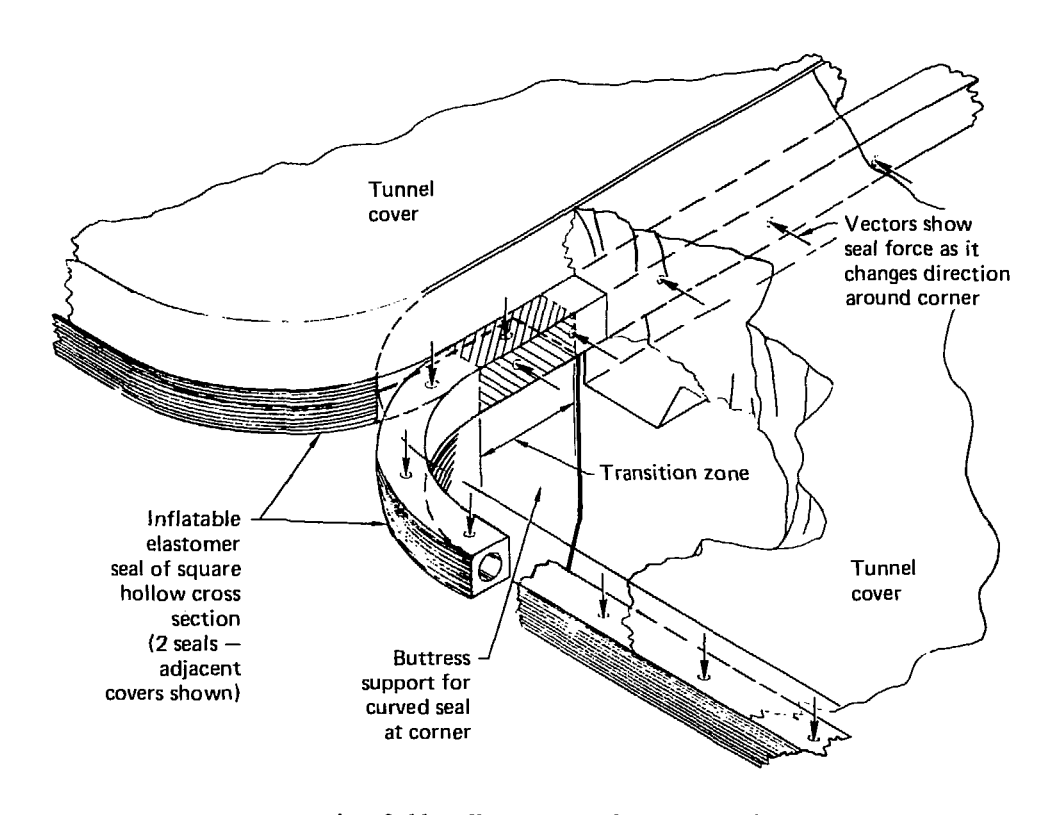   the service space beside the trench.

Fig. 8-11. Vacuum trench cover seal.

13. Mount the module on the transporter.

14. Transport to the hot cell for module disassembly.

15. Using a new-module transporter, bring a new pretested module from the assembly hall to a position next to the open trench cover.

16. Install the replacement module reversing the procedure outlined *above.*

As many modules as desired can be lifted out serially to accomplish replacement of a portion of the first-wall. Items 6 through 11 (above) can be performed simultaneously on all modules to be replaced thereby shortening multiple module change-over time.

If a flaw is detected in one pod-submodule its replacement can be accomplished more quickly by another service scenario. At the two ends of the central cell are solenoidal coils generating a 12-T magnetic field between the central cell and the thermal barrier region. These barrier coils, by their physical presence, prevent large objects from entering the "bore" of the central cell. No other reactor component interferes with translation of these coils perpendicular to the reactor axis to temporarily eliminate this obstruction. The sections of the reactor in which these coils reside can be part of two tunnels running perpendicular to the reactor axis and containing a vacuum-airlock separating the reactor from a hot cell. The tunnels are shown in Fig. 8-12 (it will be noted that the "dead end" of each tunnel which extends several meters past the reactor serves as a parking place for the barrier coil).

Central cell

Barrier coil in parked position

Plug Yan-Yang magnet

Vacuum-airlock for service car entrance and exit

Plasma direct converter

Transition magnet

Airlock door recesses
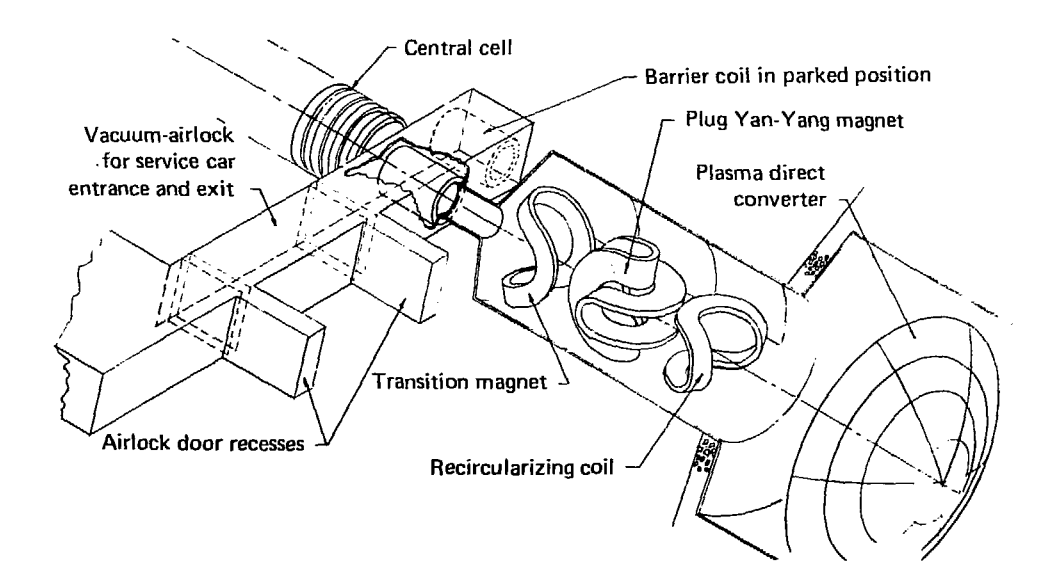
Recircularizing coil

Fig. 8-12. Service-car access tunnel.

The service car(s) park in the vacuum-airlock under normal operating conditions. When blanket service is required the barrier coil is disconnected from its current and cryogenic connections and moved aside to its parking area. The "movers" are large pneumatic cylinders and the transport tracks are below the coil and well clear of the plasma zone. Some bracing structure that serves to hold the coil in place against axial magnetic forces will have to be disengaged to permit the coil's movement.

A concept of the service car is shown in Fig. 8-13. It is equipped with carbon-cloth-covered pneumatic tires mounted on bogie trucks. The wheels roll directly on the pods and the coolant distributor housings. The bogie trucks smooth the "ride" for the module being transported. No special tracks are necessary. (Tracks would have to be cooled if permanently built-in, or would be time-consuming to install if temporary.) The blanket submodule can be replaced as follows:

1. Shut off plasma by stopping all neutral beam injection.
2. Relocate the barrier-cell mirror coil as described previously.
3. Bring the service car to the centerline of the reactor through the vacuum-airlock in the tunnel; the car moves sideways on a transporter to get into position at the open end of the central cell.
4. Move car to desired position in the central cell using laser quad-cell control to steer and to position the car.
5. Extend positioning dowels to accurately align the car.
6. Extend the rotating inner shell of the car and rotate it to the desired angle.
7. Engage pod-module grippers to the module desired.

Quad-cell
alignment
laser target

Blanket pod-module
as transported

Location and lock
dowels

Graphite cloth-covered
pneumatic tires on
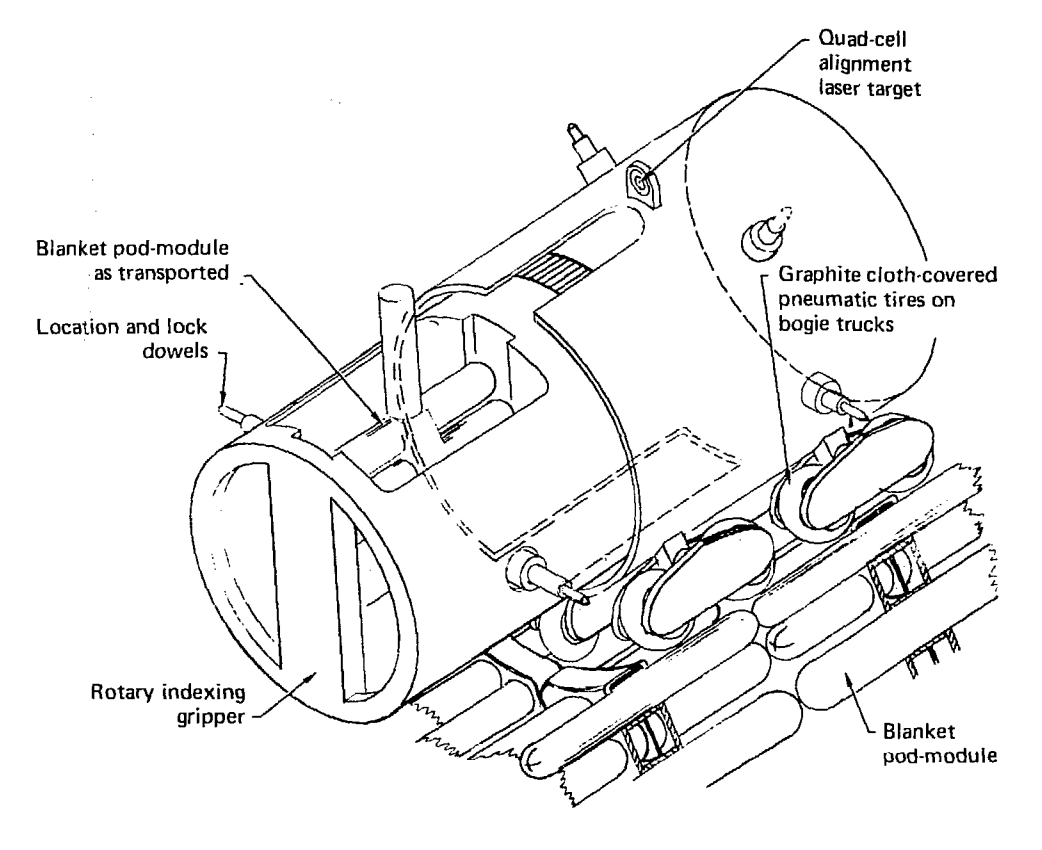bogie trucks

Rotary indexing
gripper

Blanket
pod-module

Fig. 8-13. Blanket service car.

8. By using remote tools located in the space provided outside the
   shield and between the two coils, remove two helium pipe connections
   and unbolt the gas system cover plate; park the plate nearby in the
   service gallery.

9. Grind off the pod stem weld that attaches the stem to the back of
   the shield.

10. Withdraw the pod-module into the service car extension.

11. Retract the service-car extension cylinder back into the car (with the pod-module inside).

12. Move the car back to the entrance point and onto the transporter.

13. Transport the car with the faulty pod-module to a hot cell that is part of the tunnel system.

14. Load a new pod into the service car.

15. Repeat the previous steps for installation of the replacement pod.

SUMMARY OF CENTRAL CELL DESIGN AND COST ESTIMATE

Our new central cell has the following design features:

- Efficient cylindrical pod pressure vessels for the blanket
- Li_2O neutron moderator: thin blanket
- Helium coolant
- One-tonne replaceable blanket pod-modules
- Access to pod connections from <u>outside</u> the shield
- Poured lead-cement shield
- Combined coil winding form and shield case
- A choice of maintenance methods:
  a. Service car in bore of central cell for unscheduled blanket maintenance on pod-modules
  b. Large-module change-out for scheduled first-wall replacement (a 2-m-thick "slice" of the central cell)

Our first TMR design (1977) had fabrication costs for the central cell of 3.0 million dollars/m of length. As shown in Table 8-2 this new design will total about 1.72 million dollars/m.

TABLE 8-2. Cost estimate of TMR central cell.

Item	Description	Cost (million $)
T-breeder	Li_2O He cooled	0.41
Blanket structure	Inconel 718 tube and forge $35/kG	0.15
Shield	--	0.66
Solenoid coil superconductor and coil structure	$22/kG $15/kG structure	0.50
Vacuum cylinder	Part of shield	--
Main support structure	Part of building	--
	Total cost per meter	1.72

8-1. W. S. Neef, Jr., <u>Mechanical Design Aspects of a Tandem Mirror Fusion</u>
      <u>Reactor</u>, Lawrence Livermore Laboratory, Livermore, CA, UCRL-79434 (1977).

8-2. D. J. Bender, R. S. Devoto, J. H. Fink, T. R. Galloway,
      W. E. Kastenberg, J. D. Lee, W. S. Neef, Jr., K. R. Schultz,
      D. W. Culber, S. B. Rao, and S. R. Rao, <u>Reference Design for the</u>
      <u>Standard Mirror Hybrid Reactor</u>, Lawrence Livermore Laboratory,
      Livermore, CA, UCRL-52478 (1978).

8-3. K. Tanaka, H. Kudo, and H. Amano, "Tritium Recovery of the Fusion Re-
      actor Lithium Oxide Blanket," <u>Proc. Int. Conf. on Radiation Effects and</u>
      <u>Tritium Technology for Fusion Reactors, Gattlinburg, TN, October 1-3,</u>
      <u>1975</u>, CONF-750989 3 253.

8-4. S. Nasu, H. Kudo, K. Shiozawa, T. Takahashi, T. Kurasawa, M. Tachiki,
      and K. Tanaka, "Tritium Release From Neutron Irradiated Li_2O Pellets,"
      J. Nuc. Mater., <u>68</u> 261 (1977).